INFORMATION TO USERS

This reproduction was made from a copy of a manuscript sent to us for publication and microfilming. While the most advanced technology has been used to photograph and reproduce this manuscript, the quality of the reproduction is heavily dependent upon the quality of the material submitted. Pages in any manuscript may have indistinct print. In all cases the best available copy has been filmed.

The following explanation of techniques is provided to help clarify notations which may appear on this reproduction.

1. Manuscripts may not always be complete. When it is not possible to obtain missing pages, a note appears to indicate this.

2. When copyrighted materials are removed from the manuscript, a note appears to indicate this.

3. Oversize materials (maps, drawings, and charts) are photographed by sectioning the original, beginning at the upper left hand corner and continuing from left to right in equal sections with small overlaps. Each oversize page is also filmed as one exposure and is available, for an additional charge, as a standard 35mm slide or in black and white paper format.*

4. Most photographs reproduce acceptably on positive microfilm or microfiche but lack clarity on xerographic copies made from the microfilm. For an additional charge, all photographs are available in black and white standard 35mm slide format.*

***For more information about black and white slides or enlarged paper reproductions, please contact the Dissertations Customer Services Department.**

UMI University Microfilms International

Smith, Steven Andrews

GRAVITY WAVE DYNAMICS NEAR THE MESOSPAUSE OVER POKER FLAT, ALASKA

University of Alaska, Fairbanks PH.D. 1985

PLEASE NOTE:

In all cases this material has been filmed in the best possible way from the available copy. Problems encountered with this document have been identified here with a check mark __✓__.

1. Glossy photographs or pages _____
2. Colored illustrations, paper or print _____
3. Photographs with dark background _____
4. Illustrations are poor copy _____
5. Pages with black marks, not original copy _____
6. Print shows through as there is text on both sides of page _____
7. Indistinct, broken or small print on several pages ✓
8. Print exceeds margin requirements _____
9. Tightly bound copy with print lost in spine _____
10. Computer printout pages with indistinct print _____
11. Page(s) _____ lacking when material received, and not available from school or author.
12. Page(s) _____ seem to be missing in numbering only as text follows.
13. Two pages numbered _____. Text follows.
14. Curling and wrinkled pages _____
15. Dissertation contains pages with print at a slant, filmed as received _____
16. Other _____

_____

_____

University
Microfilms
International

GRAVITY WAVE DYNAMICS NEAR THE MESOSPAUSE OVER POKER FLAT, ALASKA

A

THESIS

Presented to the Faculty of the University of Alaska

in Partial Fulfillment of the Requirements

for the Degree of

DOCTOR OF PHILOSOPHY

by

Steven Andrews Smith, B.A., M.S.

Fairbanks, Alaska

September 1985

GRAVITY WAVE DYNAMICS NEAR THE MESOPAUSE OVER POKER FLAT, ALASKA

RECOMMENDED:

Chairman, Advisory Committee

Head, Space Physics and Atmospheric Sciences Program

APPROVED:

Dean, College of Natural Sciences

Director of Graduate Programs

6/28/85
Date

Abstract

The characteristics of mesospheric gravity waves are studied using rocket and radar soundings. The soundings are examined in two different approaches: identification of individual, nearly monochromatic waves, and through the statistical view offered by spectral analysis of wind velocity fluctuations.

Simultaneous rocket and radar data has provided a complete overview of the saturation of a large-scale inertio-gravity wave near the summer mesopause. The 3m scale-size turbulence, to which the Poker Flat MST radar responds, was most intense in that phase of the wave that was most nearly unstable. However, the wave amplitude was not sufficient to produce instabilities by itself. Other waves, identified in radar data from the winter mesosphere, also lacked sufficient amplitude to become unstable yet were clearly saturated as shown by their lack of growth with height.

A comparison of vertical wavenumber spectra, of high spatial resolution (300 m) radar measurements, with a gravity wave model proposed by Van Zandt demonstrates that gravity waves dominate the mesospheric wind spectrum. These spectra also show that the wave amplitudes are

approximately 1/2 of the saturation threshold. These observations point towards wave superposition as the cause of the reduced saturation threshold.

The mesospheric spectra agree in shape and amplitude with similar spectra obtained in the stratosphere and troposphere. It is concluded that small-scale gravity waves are saturated throughout the lower and middle atmosphere. Observations of the growth of wave amplitudes with height as seen in frequency spectral studies are compatible with the conclusion that the small-scale waves are saturated since the vertical wavelength of the largest saturating wave increases with height. Waves with scales greater than the largest saturated wave are at less than saturation amplitudes and do grow with height.

Table of Contents

List of Figures

List of Tables

Acknowledgements

First and foremost, thanks go to the chairman of my committee, Dr. David Fritts, for pointing me in the right direction and frequently redirecting my footsteps. I must also thank him for taking the time to teach me the intricacies of gravity wave propagation through compressible and incompressible, quiet and disturbed, and uniform and non-uniform atmospheres.

For the data used in this study, I thank Drs. Ben Balsley of NOAA's Aeronomy Lab and C. Russell Philbrick of the Air Force Geophysical Lab. The bulk of the data, in fact, more than I could use, came from Dr. Balsley and the Poker Flat MST radar. Both Drs. Balsley and Phibrick are to be commended for the collaboration that led to the STATE campaign and the data used in Chapter 4.

The work on the gravity wave spectra was aided greatly by several discussions I had with Dr. Thomas Van Zandt of NOAA's Aeronomy Lab. I also had several written and oral discussions with Drs. Ken Gage, Jerome Weinstock and Ed Dewan that improved the section on spectral studies.

The readability of this thesis is the result of constructive criticism from several sources. Dr. Fritts uncovered several errors and ambiguities, Professor Daniel Swift and Dr. Thomas Royer very carefully read this thesis and contributed much time and effort to making the text

more understandable and finally, my wife, Barb, read much of this thesis and though she admits to understanding not a word of it, helped smooth out the wording and the flow of the logic.

This work was supported by Air Force Office of Scientific Research (AFSC) grant AFOSR 82-0125.

Symobls Used

c	horizontal wave phase speed
c_p	specific heat at constant pressure
c_s	speed of sound
f	inertial frequency
$\vec{g}$	gravitational acceleration
H	density scale height
k	wavenumber in x direction
l	wavenumber in y direction
m	vertical wavenumber
N^2	Brunt-Vaisala frequency = $(g/T)(T_z+g/c_p)$
p	pressure
R	gas constant for dry air
R_i	Richardson number = $N^2/(u_z^2+v_z^2)$
T	temperature
$\vec{V}$	wind velocity vector with components (u, v, w)
u	wind component in x direction
U_t	mean flow acceleration
v	wind component in y direction
w	vertical wind component
$\hat{x},\hat{y},\hat{z}$	unit vectors defining the coordinate system
β	intrinsic wave frequency = $k(c-U)$
Ω	earth's rotation frequency
ϕ	latitude in Chp. 2 and phase of wave in Chp. 4

λ_x, λ_y	horizontal wavelengths in x and y directions
λ_z	vertical wavelength
ρ	density
θ	potential temperature
ν	viscosity
ω	apparent wave frequency

- capital letters indicate mean quantities while primes denote the perturbation component of a variable, e.g., $u = U + u'$.
- overbars indicate average quantities.
- subscripts denote the derivative of the subscripted variable with respect to the subscript, except in the case of λ, where subscripts indicate the wavelength in the x, y or z directions.

Chapter 1

Introduction

Internal gravity waves hold a prominent position in mesospheric dynamics. Evidence has been accumulating that gravity waves transport momentum and energy from the tropoposphere and lower stratosphere to the mesosphere where they saturate, or break, resulting in the transfer of momentum to the mesospheric mean flow. To familiarize the reader with the atmosphere through which the waves propagate and the effect of these waves on mesospheric structure and dynamics, a review of the general structure and circulation of the atmosphere will be presented. Much of the material on models of the stratosphere and mesosphere can be found in Geller (1983) and a review of the theory and observations of saturating gravity waves is given by Fritts (1984).

The observed temperature structure and zonal (east - west) components of the circulation of the stratosphere and mesosphere are shown in Figure 1. These maps were constructed from meteorological rocket soundings conducted from a global network of launch sites since 1959. The stratosphere and mesosphere can be identified in Figure 1.1A. The stratosphere covers the altitude region from a relative temperature minimum, at heights of 10 km near the poles and 16 km at the equator, known as the tropopause up

A

B

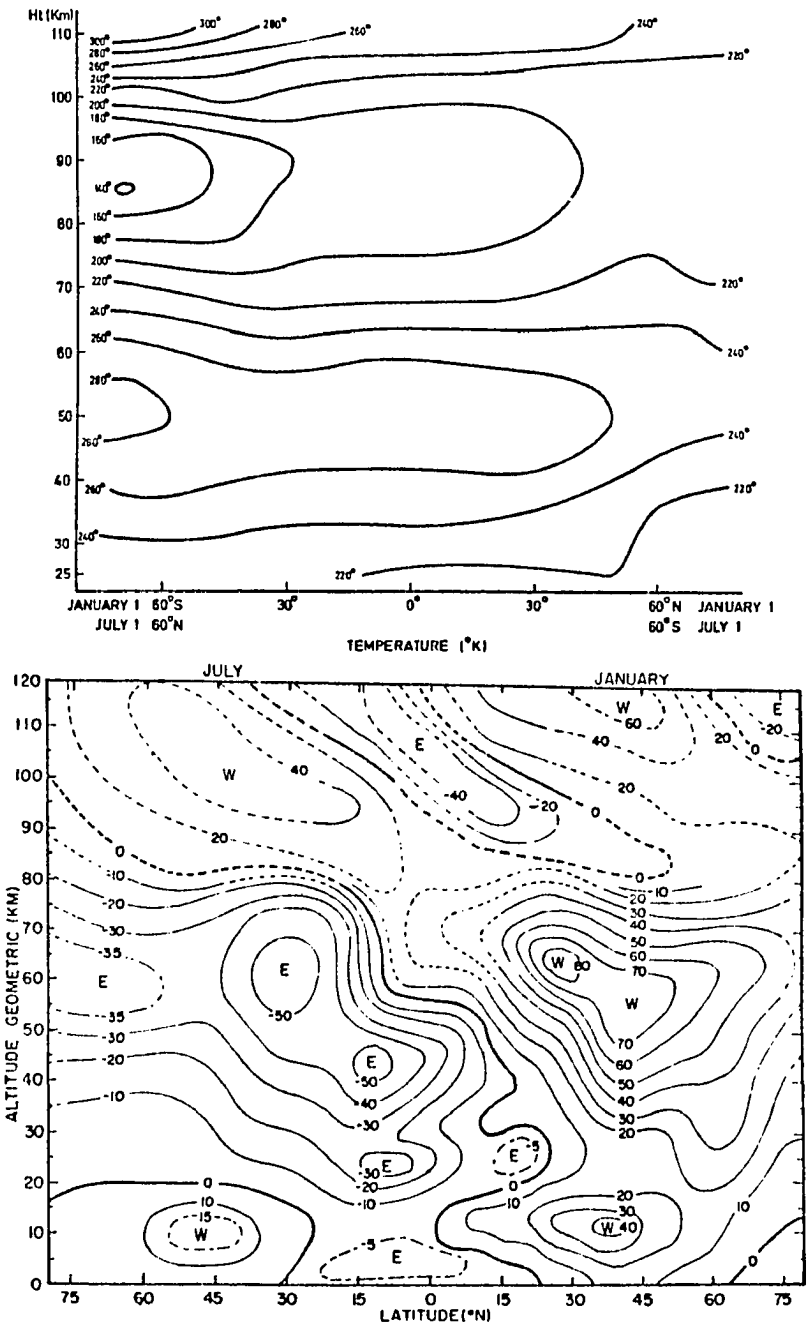

Figure 1.1 Latitude-height contours of average temperatures (A) and zonal wind velocities (B) from the CIRA 1972 model atmosphere.

to the relative temperature maximum, known as the stratopause, near 50 km. Generally, the boundaries known as the tropopause, stratopause and mesopause are located at heights where the mean vertical temperature gradient reverses or changes sign. Throughout the stratosphere, the temperature increases with height.

From 50 km to about 85 km the temperature decreases with height. This region is known as the mesosphere. The minimum temperature near 85 km marks the mesopause. The summer hemisphere mesopause is identified by a sharp minimum in temperature of about $140^{o}K$. The winter mesopause, unlike the summer mesopause, is marked by a fairly broad region having a nearly constant temperature. Above the mesopause the temperature steadily increases in the region generally known as the thermosphere. The term middle atmosphere encompasses the stratosphere, mesosphere and lower thermosphere covering the heights from 20 to 100 km. The region above 100 km up to about 600 km is also known as the ionosphere, since significant portions of the atmospheric constituents are ionized in this region. The work reported in this thesis deals mainly with the mesosphere.

Pressure and density values in the mesosphere are a factor of 10^{-5} smaller than values near the surface. Both pressure and density decrease exponentially with height

with an e-folding height of 7 km. The molecular composition of the atmosphere is constant up to about 100 km. Above this height the density is low enough and the mean free path is large enough to allow molecular diffusion to vertically separate the various atmospheric constituents.

The basic temperature structure shown in Figure 1.1A is determined primarily by the differential absorption of solar radiation. The stratosphere has a mean meridional (north - south) temperature gradient with the summer stratosphere being warmer than the winter stratosphere. The meridional temperature gradient is produced by ozone, which has its maximum concentration near a height of 30 km, absorbing solar ultra-violet radiation, and locally heating the stratosphere. The winter-summer difference is due to the summer stratosphere receiving a greater amount of solar radiation over the course of a day while the winter stratosphere spends a greater percentage of a day in the earth's shadow. The meridional temperature gradient in the mesosphere is reversed relative to the temperature gradient in the stratosphere. A series of atmospheric circulation models has shown that the mesospheric temperature structure is determined by dynamics rather than radiative heating and cooling.

The first successful model of the mesospheric temperature and wind structure was produced by Leovy (1964). His model assumed a hydrostatic atmosphere with zonal and meridional winds in geostrophic balance between pressure and Coriolis forces. The driving force for the circulation was an imbalance between heating of the atmosphere by solar radiation and cooling of the atmosphere by radiative emission of CO_2. Leovy obtained a model atmosphere that was warmer at the summer pole throughout the stratosphere and mesosphere than observed temperature profiles. The geostrophic winds which resulted from such a distribution of temperature and pressure were quite different from the observed zonal winds (Figure 1.1B) with summer hemisphere easterlies and winter westerlies monotonically increasing with height and not forming the observed closed jets. (A closed jet has wind speed decreasing both above and below the wind maximum.)

Leovy obtained better agreement with observations by adding a Rayleigh drag term to the equations of motion. A Rayleigh drag is a 'pseudo' force proportional to and directed opposite to the wind velocity. With the addition of the Rayleigh drag the mesospheric jets closed and the mesospheric temperature gradient reversed such that the winter mesopause was warmer than the summer mesopause. The magnitudes of the winds were larger than observed and the

temperatures were not in precise agreement, but the model clearly showed that dynamics was a significant factor in determining the average mesospheric temperature and wind structure.

A large circulation cell maintains the observed atmospheric structure. The air that is heated in the summer stratosphere rises and cools adiabatically, causing the cold summer mesopause. There is then a mesospheric meridional transport of the air from high pressure in the summer to low pressure in the winter hemisphere. The air descends over the winter hemisphere and warms adiabatically, producing the relatively warmer winter mesopause. The cell is completed by weak meridional flow in the lower stratosphere.

Various refinements have been added to this conceptual model, including better parameterizations of radiative cooling and the addition of a drag coefficient that increases exponentially with height but the basic results remain: zonal wind drag is needed to produce the observed wind and temperature structure. However, the models have not identified the physical force responsible for the 'artificial' Rayleigh drag used to simulate a zonal drag.

Recently, it has been recognized that the saturation of vertically propagating gravity waves is the mechanism responsible for the zonal drag (Houghton, 1978; Lindzen,

1981). Before examining the connection between zonal drag and saturating gravity waves, it is appropriate to present a brief history of the study of gravity wave propagation to and through the mesosphere.

Hines (1960) argued conclusively that irregular wind fluctuations seen in meteor trail winds and in travelling ionospheric disturbances (TIDs) were manifestations of gravity waves propagating vertically through the upper atmosphere. Hines gave an outline of linear gravity wave theory and noted that one of the properties of gravity waves is that the wave amplitudes grow with height in proportion to the decrease in density in order to keep the kinetic energy flux constant. Since wave kinetic energy is proportional to ρV^2, where ρ is density and V is the wave amplitude, and since density decreases exponentially with height, then V must increase exponentially as $\rho^{-1/2}$.

Hodges (1967, 1969) extended Hines' theory to show that waves could grow until they acheived unstable amplitudes. He also postulated that the waves would not grow with height above the altitude at which they became unstable but would be limited in amplitude by dissipation resulting from convective instability. This limiting process is called saturation. Hodges supported his contention that gravity waves could become unstable and generate turbulence by examining previously published mesospheric wind profiles

and gravity wave observations. He found several waves that met the criteria for producing instabilities. Lindzen (1968) examined the growth with height of vertically propagating diurnal tidal waves (note that tides are simply global-scale gravity waves with periods that are integer fractions of a day, i.e. 24, 12, 8 hours) and found that tidal waves would become unstable in the mesosphere.

In the ensuing years, support for the gravity wave interpretation came from observations of sodium vapor drift clouds, rocket grenade temperature profiles, TIDs as revealed by electron density measurements and periodic fluctuations in other ionospheric parameters. Additionally, there was continual development of gravity wave theory. In an important study, Booker and Bretherton (1967) showed that waves which do not grow with height would result in the acceleration of the background wind. Thus, gravity waves transport momentum from their source to the regions where they are dissipated. The acceleration of the mean wind brought about by wave dissipation is always toward the horizontal phase speed of the dissipating wave. Much of the theoretical work, gravity wave observations, and interpretations up to 1974 were summarized in the collection of papers by Hines (1974).

The recognition that the mean wind accelerations due to saturating gravity waves can provide the drag needed to

explain the observed mesospheric wind and thermal structures was advanced by Houghton (1978) and developed in a quantitative manner by Lindzen (1981). Lindzen argued that waves of tropospheric origin which reach the mesosphere would have the correct direction and phase speeds to bring about the reversal of the zonal wind shears. He also assumed typical gravity wave parameters and reported that the resulting acceleration could more than provide the required drag.

Soon after the identification of gravity waves as the physical mechanism producing the zonal wind drag, several models were developed to include gravity waves and the effects of wave saturation. These models (Holton, 1982, 1983; Dunkerton, 1982) showed that reasonable wind profiles could be produced by saturating gravity waves. Qualitative agreement was obtained with observed winds by incorporating waves having only three discrete horizontal phase speeds in Holton's case and an approximately Gaussian distribution of phase speeds about an assumed tropospheric mean wind speed in Dunkerton's model. However, there is sufficient uncertainty in knowledge of gravity wave parameters that agreement with practically any wind profile could be obtained by judicious choice of wave amplitudes and phase speeds. Clearly, the models lack a complete and accurate specification of the spectrum of gravity waves contributing

to the mesospheric wind drag. This information can only be determined by observation.

Previous gravity wave observations have usually been of waves in the ionosphere. One of the reasons for this observational bias is the growth of the dominant wave scales with height which makes them large enough in the ionosphere to be readily identifiable (Hines, 1960). Another reason is that observational techniques were optimized for ionospheric sounding.

It is now well known that observed fluctuations in ionospheric wind velocities and electron densities are caused by gravity waves. Some of these waves have been traced to sources near the tropospheric jet stream. Others have been attributed to auroral perturbations, electrojet fluctuations, or to shock waves produced by sudden cooling in the shadow of a solar eclipse. All of these sources are discussed in Hines (1974). However, it is likely that most of the waves observed below the ionosphere, in the mesosphere, are propagating upwards from the lower atmosphere rather than travelling downwards from auroral or ionospheric heights since downward travelling waves propagate into regions of exponentially increasing density causing their amplitudes to decrease exponentially.

More recent gravity wave studies have been performed through analyses of winds measured by MST (Mesosphere-

Stratosphere-Troposphere), meteor and partial reflection drifts radars, all of which obtain echoes from the mesosphere. Several instances of identifiable, monochromatic waves have been reported (Woodman and Guillen, 1974; Rastogi and Bowhill, 1976; Manson and Meek, 1980; Manson et al., 1981; Frezal et al., 1981; Royrvik et al., 1982; Hirota et al., 1983; Vincent and Reid, 1983; Smith and Fritts, 1983). These observations provide discrete data points in broad regions of the gravity wave frequency, wavelength and phase speed spectra. A detailed description of the gravity wave spectrum has not emerged from these isolated, single wave observations partially because of the limited number of observations and also because the waves most readily isolated from the background wind fluctuations have unusually large amplitudes and thus are not 'average' waves. A gravity wave climatology or a statistical description of gravity waves and their effects is needed to accurately specify wave drag, the general circulation, and energy and momentum transfer throughout the atmosphere.

An average gravity wave picture can be obtained by spectral analysis of velocity fluctuations as functions of frequency and wavenumber. Frequency spectra of horizontal velocity fluctuations in the mesosphere have been computed by Vincent and Ball (1981), Frezal et al. (1981) and

Balsley and Carter (1982). All of the observed spectra have similiar forms, with the amplitude of horizontal velocity spectral density having a power law relationship to frequency with a power of -1.5 to -2.0.

Vincent (1984) found that spectra taken at Poker Flat, Alaska by Balsley and Carter (1982) agreed in shape and absolute magnitude with spectra obtained at two low-latitude sites in Australia by Vincent and Ball (1981). This led Vincent to state that there was good evidence for a 'universal' spectrum of gravity waves. Universality was implied by the observation that the gravity wave spectrum appeared to be the same no matter where (in latitude) it was sampled. Frezal et al. (1981) also reported evidence for a universal spectrum since spectra measured in Norway, France and Puerto Rico were nearly identical. Vincent (1984) also demonstrated the utility of spectral analysis by determining the vertical wavenumber spectra for waves having long apparent periods (> 5 hrs). He found that at least 65% of the total energy of the long period waves was in upward propagating waves.

In conjunction with the increased number of spectral observations, Van Zandt (1982) proposed a universal gravity wave spectral modelbased on various studies of wave motions in the troposphere, stratosphere and mesosphere. Van Zandt's spectrum closely mimics the universal spectrum of

oceanic gravity waves introduced by Garrett and Munk (1972, 1975), which has been shown to be an excellent first order model of gravity wave motions in the ocean (Munk, 1981). If an atmospheric universal spectrum could be verified, it would certainly provide a secure basis for modelling of the gravity wave - middle atmosphere interaction.

In this thesis, the role of gravity waves in mesospheric dynamics will be examined. The theoretical background needed to identify gravity waves and their effects will be presented in Chapter 2. The current theories on atmospheric wave saturation will also be reviewed in Chapter 2. The techniques of rocket and MST radar soundings of the mesosphere will be outlined and compared in Chapter 3. It will be shown that the two techniques yield equivalent measurements of the wind field. In Chapter 4, temperature measurements from a rocket sounding made during the STructure and Atmospheric Turbulence Environment (STATE) campaign will be combined with velocity time series data obtained by the Poker Flat MST radar to examine the saturation of a large-scale, low-frequency gravity wave at the summer mesopause. Radar signal strength is found to be greatest in that phase of the wave that would be predicted to be most nearly dynamically unstable. Individual, nearly monochromatic waves that have been identified from winter velocity data obtained with the Poker Flat radar will be described in

Chapter 5 and the possible effects of the waves on the mean flow will be reported. It will be shown in Chapter 6 that gravity wave motions dominate the atmospheric velocity fluctuation power spectrum, near the mesopause, through comparison of observed vertical wavenumber spectra with Van Zandt's gravity wave model spectrum. The observed mesospheric spectra are very similar in shape and amplitude to stratospheric spectra. This observation leads to the conclusion that small (less than 5 km) vertical scale gravity waves are limited to saturation amplitudes throughout the atmosphere. Conclusions on gravity wave dynamics observed near the mesopause will be presented in Chapter 7.

Chapter 2

Gravity Wave Theory

Identifying gravity wave perturbations in data containing many other types of atmospheric motions requires theoretical guidelines. These theoretical guidelines come from the equations governing atmospheric fluid motions. Approximations can be made when solving these equations to obtain solutions that can be used to differentiate among the multitude of atmospheric motions. For example, it is possible to separate planetary waves, with scales on the order of the earth's circumference, from smaller scale gravity waves or to separate gravity waves from even smaller scale turbulent motions. Relations between atmospheric parameters, derived from gravity wave solutions of the fluid equations, will be used to identify gravity waves in the data to be presented in subsequent chapters and also to deduce the effects of such waves on the atmosphere.

Beginning with the basic equations of fluid motion, this chapter will review atmospheric gravity wave theory. The assumptions needed to solve the equations with gravity wave solutions will be stated and discussed. After the solutions are presented, the relationships between horizontal and vertical velocities, temperature and density perturbations and the frequency of the waves will be

developed. These relationships will be used in later chapters to identify gravity waves. Finally, effects of gravity waves on atmospheric mean flows will be demonstrated, and the recent theories describing the saturation or breaking of gravity waves that lead to acceleration of the mean flow will be reviewed.

2.1 Gravity wave solutions of the equations of motion

In an ideal, rotating atmosphere the fluid motion is governed by three conservation principles; conservation of momentum, mass and energy. The equations expressing these principles are

$$\frac{D\vec{V}}{Dt} + 2\vec{\Omega} \times \vec{V} = -\vec{\nabla}p + \rho\vec{g} + \nu\nabla^2\vec{V} \qquad (2.1)$$

$$\frac{D\rho}{Dt} = \rho\vec{\nabla}.\vec{V} \qquad (2.2)$$

$$\frac{D\theta}{Dt} = 0 \qquad (2.3)$$

where $\vec{V}$ is the velocity vector with components u, v and w in the $\hat{x}$, $\hat{y}$, and $\hat{z}$ directions, which usually are directed east, north and upward. ρ is density, p is pressure, $\vec{g}$ is the acceleration of gravity, ν is the kinematic viscosity and θ is potential temperature.

The momentum (also known as the Navier-Stokes) equation has the inertial or total derivative as the leftmost term, followed by a term expressing the Coriolis acceleration due to rotation of the reference frame. On the right side of the equation are terms corresponding to the driving forces;

the pressure gradient, gravitational acceleration and a viscous damping term. The viscous term will be dropped from further consideration as gravity waves generally have scale sizes much larger than the average mean free path and frequencies much smaller than collision frequencies so that the viscous drag term is much smaller than the other terms in the equation.

The Coriolis term, $2\vec{\Omega} \times \vec{V}$, has components $-2v\Omega\sin\phi$, $2u\Omega\sin\phi$ and $-2u\Omega\cos\phi$ with ϕ being the latitude of the origin of the reference frame. The $-2u\Omega\cos\phi$ term can be dropped from the vertical component equation of motion since it is much smaller than the gravity term. The horizontal Coriolis terms can be rewritten as $-fv$ and fu where $f = 2\Omega\sin\phi$ and f is known as the inertial frequency or Coriolis parameter.

The so-called energy conservation equation is more accurately called the entropy conservation equation. The connection between entropy and potential temperature is given by the definition of potential temperature. Potential temperature is defined as the temperature that a parcel of air would have if it were brought adiabatically to a reference pressure level, p_o, usually taken to be 100 kPa (= 1000mb) which is approximately sea level pressure. Combining the second law of thermodynamics with the

equation of state for an ideal gas, $p = \rho RT$, yields the definition of potential temperature as

$$\theta = T \left(\frac{p}{p_o}\right)^{R/c_p} \qquad (2.4)$$

where R is the gas constant for dry air and c_p is the specific heat at constant pressure. We have assumed the atmosphere to be an ideal, dry and non-viscous fluid, which is a good approximation for the motions we are examining in the mesopshere. By taking the total derivative of eqn. 2.4, we obtain

$$\frac{1}{c_s^2} \frac{Dp}{Dt} = \frac{D\rho}{Dt} \qquad (2.5)$$

where c_s is the speed of sound and is equal to γRT with γ being the ratio of specific heat at constant pressure to the specific heat at constant volume. For simplicity we will assume c_s to be infinite or, equivalently, that the atmosphere is incompressible. Retaining a finite c_s produces solutions that differ from the solutions to be discussed here only in that they include terms corresponding to compressional acoustic waves (Hines, 1960). Acoustic waves, which have frequencies greater than gravity waves, are inefficeient transporters of momentum and will not be discussed further. With $c_s \rightarrow \infty$, the energy equation becomes

$$\frac{D\rho}{Dt} = 0 \qquad (2.6)$$

With this condition the mass continuity equation is simplified to

$$\vec{\nabla}.\vec{V} = 0 \qquad (2.7)$$

The next step in the solution of the equations is to use the linear perturbation method. All variables are assumed to be composed of a mean, steady-state component, that does not vary with time or horizontal distance but can vary with height, and a small fluctuating component. For example, velocity in the x direction is expanded as $u(x,y,z,t) = U(z) + u'(x,y,z,t)$, where the capital letter indicates the mean or average quantity and a prime identifies the fluctuating component.

After substitution of the mean and perturbation variables, the equations can be separated into mean and perturbation equations. Solution of the zeroth order equations, involving only mean quantities, produces the geostrophic relation and the hydrostatic equation. The geostrophic relation states that, to zeroth order, the mean wind is the product of a balance between horizontal pressure gradient forces and the Coriolis force. The hydrostatic equation,

$$\bar{p}_z = -\bar{\rho}g \qquad (2.8)$$

expresses the fact that the atmosphere is stably stratified on average with mean pressure at any height being equal to

the weight of the atmosphere above that height. Note that subscripts, except on λ, will indicate the partial derivative with respect to the subscripted variable and overbars will be used, along with capitals, to indicate mean quantities.

Another average quantity that will appear is $\bar{\rho}_z$, which can be evaluated using the hydrostatic equation and the equation of state. Substituting from the equation of state into the hydrostatic equation gives

$$\frac{\bar{\rho}_z}{\bar{\rho}} = - \left(\frac{g}{R\bar{T}} + \frac{\bar{T}_z}{\bar{T}} \right) \qquad (2.9)$$

This equation has the solution $\rho = \rho_0 \, e^{-z/H}$ with H, the density scale height defined as

$$H \equiv R \, \bar{T} \, / \, (g + R \, \bar{T}_z) \qquad (2.10)$$

H is approximately 7 km from the ground to about 100 km.

The x, y, and z components of eqns. 2.1, 2.2 and 2.3 are

$$\bar{\rho} \, (u'_t + Uu'_x + Vu'_y) - \rho f v' = - p'_x \qquad (2.11)$$

$$\bar{\rho} \, (v'_t + Uv'_x + Vv'_y) + \rho f u' = - p'_y \qquad (2.12)$$

$$\bar{\rho} \, (w'_t + Uw'_x + Vv'_y) = - p'_z - \rho \, g \qquad (2.13)$$

where horizontal and time derivatives of mean quantities have been eliminated and it has been assumed that $\bar{W} = 0$.

The equations have been linearized by dropping any terms involving the product of two or more perturbation quantities. This derivation also neglects any shear of the mean wind. Such a shear can alter gravity wave propagation, causing reflection or absorption of the waves. Shear is neglected here because the observations to be presented later cover a small height region of the atmosphere. Thus, it is not possible to readily identify the effects of shear on waves. For this situation, U is assumed to vary much more slowly with height than the perturbation velocities, which is a good assumption for the types of waves to be examined.

The equations are now solved by assuming wave-like variations in the x-y plane. Again, using velocity in the x direction for the purposes of illustration

$$u'(x,y,z,t) = u'(z)e^{i(kx + ly - \omega t)}$$

The horizontal derivatives are now $u_x = iku'$ and $u_y = ilu'$. Performing x and y derivatives produces five equations in the five varibles u', v', w', p' and ρ', which can be combined to yield an equation in a single varible. Traditionally, the single variable is w' and the equation is

$$w'_{zz} + \frac{\bar{\rho}}{\bar{\rho}}_z w'_z + \left(\frac{N^2 - \beta^2}{\beta^2 - f^2}\right)(k^2 + l^2) w' = 0 \qquad (2.14)$$

N is the Brunt-Vaisala or buoyancy frequency and is defined

for an incompressible atmosphere as $N^2 = - \rho_z \ (g / \rho)$. More generally,

$$N^2 = \frac{g}{\theta} \theta_z = \frac{g}{T} (T_z + g/c_p) \qquad (2.15)$$

N enters equation 2.14 when the $\rho'g$ term in the vertical momentum equation is replaced, with an expression obtained from the incompressible energy equation (2.6). Physically, N is the frequency at which a parcel of air would oscillate if it were displaced vertically against the background stable stratification of the atmosphere. β is defined to be $\beta \equiv \omega - kU - lV$ and is the intrinsic or Doppler shifted frequency that the wave has in a reference frame moving with the background wind (U, V). ω is the apparent frequency measured in a fixed (earth-bound) reference frame.

The vertical derivatives cannot be easily simplified by assuming wave-like variations in the vertical because mean quantities, such as N, vary with height. If the mean quantities vary slowly compared to the vertical wavelengths of the solutions then the WKB approximation applies. This results in solutions of the form $w' \sim m^{-1/2} \ e^{i\int m \, dz}$, where m is the vertical wavenumber. Employing this solution for

w', the equations can be solved for m to yield

$$m^2_{real} = (k^2 + l^2)\left(\frac{N^2 - \beta^2}{\beta^2 - f^2}\right) - \frac{1}{4H^2}$$

$$m_{imag} = -\frac{1}{2H} \qquad (2.16)$$

where the real and imaginary parts of m are given separately. The imaginary part of m leads to exponential amplitude growth with height since there will be a term of the form $e^{z/2H}$ in the wave solutions. Henceforth, this term will be implied and will not be written explicitly. Generally, $m^2 >> 1 / 4H^2$ or $4\pi H > \lambda_z$ where $4\pi H \simeq 100$ km and therefore, the real part of m can be simplified by dropping the $1 / 4H^2$ term.

For a wave to propagate vertically m must be real. This implies that $f < \beta < N$ or that the intrinsic period be less than 13.2 hrs (the inertial period at Poker Flat) and greater than about 5 minutes (a typical Brunt-Vaisala period).

There are several simplifications that can be made to the above formula that will clarify the physical picture of propagating waves. The first simplification is to rotate the horizontal axes of the reference frame such that the wave is propagating along the x axis or force the horizontal wavenumber, $\vec{K}_h$ ($= \vec{k} + \vec{l}$), to be parallel to $\hat{x}$. Then the wavelength of the wave in the $\hat{y}$ direction is made infinite so $\vec{l} = 0$ and $\beta = (\omega - kU) = k(c - U)$ where c is

the horizontal phase speed of the wave and is equal to ω/k. In general, waves to be examined later have frequencies greater than f. In this case the formula for m can be further simplified;

$$m^2 \simeq \frac{k^2(N^2 - \beta^2)}{\beta^2} = \frac{N^2}{(c-U)^2} - k^2 \qquad (2.17)$$

The next simplification can be made by assuming the waves to be hydrostatic. Hydrostatic waves have vertical wavelengths much shorter than horizontal wavelengths or $m >> k$. This means that the perturbation velocities are directed more horizontally than vertically. Equivalently, the hydrostatic condition implies that the wave frequencies are much smaller than N. For hydrostatic waves,

$$m^2 = \frac{N^2}{(c-U)^2} \quad \Rightarrow \quad m = \pm \frac{N}{(c-U)} \qquad (2.18)$$

From the above expressions for m it is clear that m can be either positive or negative. To determine the sign of m consider the phase and group velocities of a wave. First rearrange the formula for m to get an expression for frequency

$$\omega = k\ (U \pm N/m) \qquad (2.19)$$

Then phase and group velocities are

	phase velocity	group velocity
horizontal	$\omega/k = U \pm N/m$	$\omega_k = U \pm N/m$
vertical	$\omega/m = (k/m)(U \pm N/m)$	$\omega_m = \mp kN/m^2$

(2.20)

The horizontal phase and group velocities are equal and have the same direction.

For upward energy propagation the lower sign is chosen or $m = N/(U-c)$ and vertical phase velocity equals $(k/m)(U-N/m)$. Since c is along the positive x axis, c is positive and m will be negative for $U < c$ and positive for $U > c$. Similiarly, if $U < c$ the vertical phase velocity is $(U - N/m)\ k/m = kc / m$ and is negative or downward, since m is negative and phase velocity is positive or upward for $U > c$. For downward energy propagation the opposite signs hold.

The vertical phase and group velocities are in opposite directions. A wave propagating upward (downward) in the direction of its group velocity has downward (upward) propagating phase fronts. Thus given U along the horizontal direction of wave propagation, the directions of vertical phase and group velocity can be determined.

The frequency limits of N and f limit the propagation of waves. As β approaches f, m becomes infinite or, equivalently, the vertical wavelength approaches zero. In

this case, the direction of phase propagation, given by $\vec{K} = \vec{k} + \vec{m}$, is strictly vertical. However, the direction of energy propagation is perpendicular to the direction of phase porpagation for such low frequency waves. Hence, the wave packet propagates horizontally only, with the mean flow speed, and is prevented from further vertical propagation by the 'critical level' defined as that level at which $\beta = f$. Thus Doppler shifting of the intrinsic wave frequency as the wave encounters differing values of U can lead to wave absorption.

Towards the other limit, as β approaches N, m approaches 0 and the vertical wavelength approaches infinity. Since $\beta \sim N$, the wave frequency is approximately the Brunt-Vaisala frequency. These Brunt-Vaisala frequency waves propagate horizontally only. Thus slow changes in N with height or Doppler shifting of β towards N produces horizontally propagating waves that are reflected back towards the direction from which they came in the vertical plane. Therefore altitudes at which $\beta = f$ or $\beta = N$ act as barriers to further vertical propagation of a wave.

Relationships between the gravity wave parameters u', w', ρ', T', θ' and p' have been termed "polarization" relations (Hines, 1960). The relation between u' and w' is

most easily obtained from the incompressible continuity equation (2.7)

$$\vec{\nabla}.\vec{V} = u'_x + w'_z = iku' + imw' = 0 \Rightarrow \frac{u'}{w'} = -\frac{m}{k} \quad (2.21)$$

Note that u' and w' are in phase in the direction of wave propagation for upward propagating waves (i.e., $m < 0$). This fact will be used later to determine propagation directions.

The relation between u' and v' comes directly from the v' momentum equation and is

$$v' = -i\frac{u'f}{\beta} \quad (2.22)$$

From this expression it is clear that u' and v' are in phase quadrature but the magnitude of v depends on the intrinsic wave frequency with the magnitude being greater the closer the intrinsic frequency is to the inertial frequency. Thus, for intrinsic frequencies much larger than the inertial frequency, $v' \sim 0$ and the wave is a plane wave while for frequencies near f, v' is non-zero and air parcels will travel in elliptical orbits under the influence of such a wave. These waves are known as rotary or inertio-gravity waves.

ρ' can be expressed in terms of the wave amplitude

using the incompressibility condition (eqn 2.6). From perturbation theory

$$\rho' = \frac{i\ w'}{k(U-c)}\ \bar{\rho}_z \qquad (2.23)$$

Similiarly, θ' and T' are obtained from the energy conservation equation

$$\theta' = \frac{i\ w'}{k(U-c)}\ \bar{\theta}_z \qquad T' = \frac{i\ w'}{k(U-c)}\ \bar{T}_z \qquad (2.24)$$

These equations can be simplified for hydrostatic waves by using equations 2.18 and 2.21 to

$$\rho' = \frac{iN\bar{\rho}}{g}\ u' \qquad \theta' = -\frac{iN\bar{\theta}}{g}\ u' \qquad T' = -\frac{iN\bar{T}}{g}\ u' \qquad (2.25)$$

Pertubation pressure is given by the horizontal momentum equations as

$$p' = \bar{\rho}\ (U-c)\ u' \qquad (2.26)$$

and relations between m, k, ω, u' and w' are as given before by the dispersion relation and the mass continuity equation.

2.2 Wave effects

Internal gravity waves have the potential for altering the mean wind speed and the average potential temperature, producing turbulence and transporting heat and atmospheric constituents vertically. However, it is only in regions where the waves are undergoing dissipation that such effects appear since conservative waves leave the atmosphere unchanged as they pass through.

The magnitudes of such effects can be obtained through use of the linearized equations of motion and mass continuity that have been averaged over a horizontal wavelength or over a wave period. Combining the linearized and averaged equations gives

$$\bar{\rho}U_t = -(\overline{\rho'u'})_t - (\bar{\rho}\,\overline{u'w'} + \overline{\rho'u'w'})_z - (\bar{\rho}\,\overline{u'^2} + \overline{\rho'u'^2})_x - \overline{\rho'w'}\,U_z - (\bar{\rho}U + \overline{\rho'u'})_x - \bar{p}_x \tag{2.27}$$

for a compressible, non-rotating, two-dimensional fluid (Hinze, 1975, p. 22). Since ρ' and u' or w' are in phase quadrature, carrying out the averaging operation removes all terms containing ρ'. The $(\bar{\rho}\,\overline{u'w'})_z$ term represents a wave drag on the mean flow and is known as a Reynolds stress since Reynolds first derived terms of that form. If a wave is strictly conservative, its perturbation velocity grows exponentially with height as $e^{z/2H}$. Then $\overline{u'w'}$ is proportional to $e^{z/H}$ and $\bar{\rho}\,\overline{u'w'}$ is constant so that the wave drag is zero. This is the essence of the Eliassen - Palm (1960) Theorem which states that $(\bar{\rho}\,\overline{u'w'})_z = 0$ in the absence of wave forcing or dissipation. If, on the other hand, the wave growth with height is limited by dissipation, then there will be a finite wave drag on the mean flow. This term is the theoretical basis for the wave drag needed to close the mesospheric jets as mentioned in

the introduction. From the above discussion, it is clear that upward-propagating waves must be dissipated in order to produce a wave drag in the mesosphere.

In the absence of dissipation the waves grow exponentially with height. It is thus possible for the wave amplitude to grow large enough for the wave to become unstable and break or saturate. An idealized view of this process is that the waves reach an amplitude above which energy is lost to turbulence, to the mean flow or to other waves. This amplitude is the saturation amplitude. The waves do not break and completely disappear in the manner of surface waves approaching a shoreline but "breaking waves" provides a convenient physical interpretation.

Since the work of Hodges (1967) it has been known that gravity waves grow to sufficient amplitudes to become convectively unstable. A convective instability is characterized by a wave induced temperature gradient that is more negative than the adiabatic lapse rate. Such a gradient renders that region of the atmosphere convectively unstable. The unstable region becomes turbulent, wave energy is converted to turbulent energy, the temperature gradient is turbulently mixed and the turbulence continues to be produced until the lapse rate becomes adiabatic. The limiting amplitude for such a wave, i.e., the amplitude for which the perturbation temperature lapse rate is adiabatic,

can be determined from the simplified, linear perturbation temperature relation, eqn. 2.25,

$$T'_z = imT' = \frac{N}{g}\,\bar{T}mu' \qquad (2.28)$$

The condition for convective instability is that the local temperature gradient becomes superadiabatic or

$$N^2 \leq 0 \;\Leftrightarrow\; \frac{g}{\bar{T}}\,(T'_z + \bar{T}_z + g/c_p) \leq 0$$

$$\Rightarrow\; T'_z \leq -(\bar{T}_z + g/c_p) = \bar{T}\,N^2/g \qquad (2.29)$$

$$\Rightarrow\; u'\frac{m\,N\,\bar{T}}{g} \geq \frac{\bar{T}\,N^2}{g} \;\Rightarrow\; u' \geq \begin{matrix} N/m = U-c & \text{for } U>c \\ -N/m = c-U & \text{for } c>U \end{matrix}$$

The wave becomes convectively unstable when the horizontal perturbation velocity is greater than the horizontal phase speed of the wave relative to the local mean flow. Orlanski and Bryan (1969) derived a criterion for instability in terms of an "exchange" velocity, which was defined as the time derivative of the perturbation temperature divided by the horizontal derivative of the perturbation temperature. Orlanski and Bryan proved, through analysis of the thermodynamic energy equation, that convective overturning would occur whenever the velocity perturbation exceeded the exchange velocity. The exchange velocity can be shown to be equal to U-c for monochromatic waves.

Another instability that acts to limit the exponential growth of waves is the shear or dynamic instability. A

shear instability arises when the vertical shear, V_z, becomes greater than the local stability of the atmosphere given by N. Specifically, when the Richardson number, defined as

$$R_i \equiv N^2 / V_z^2 \qquad (2.29)$$

is less than 1/4, a shear instability or Kelvin-Helmholtz instability may be initiated, resulting in the production of turbulence. Fritts and Rastogi (1985) calculated the wave amplitude necessary to reduce Ri to less than 1/4 by expanding N in terms of a mean plus wave perturbation and by computing the shear, in the denominator of Ri, using both the longitudinal and tranverse components of the wave-induced velocity shear. For waves with frequencies much larger than the inertial frequency, dynamic instabilities are possible only when $u' \sim U-c$, implying that convective instabilities are the dominant instability produced by high-frequency waves. However, the amplitude threshold for dynamic instability decreases as the wave frequency approaches f due to the increase in amplitude and shear of the transverse velocity component. In low-frequency, inertio-gravity waves, the maximum shear of the tranverse velocity component occurs at the same phase of the wave in which the temperature perturbation has reduced N to a minimum (the same point in the wave field where convective

instabilities develop in high-frequency waves). Thus, low frequency waves more readily dissipate through dynamical rather than convective instablities. The amplitude limit derived by Fritts and Rastogi (1985) is given by

$$u' = (2 + 2(\alpha(\alpha^2-1)^{1/2} - \alpha^2)\ (U-c) \qquad (2.31)$$
$$\text{with } \alpha \equiv \beta/f$$

For example, with $\beta/f = 1.25$, the amplitude required for the possibility of dynamic instability is $u' < .75(U-c)$.

The amplitude $u' = U-c$ is a simple, intuitive limit for monochromatic waves. It will be used here to obtain an estimate for the Reynolds stress similiar to that derived by Lindzen(1981). Lindzen derived an expression for wave acceleration by a monochromatic wave above some level at which the wave achieved saturation amplitude. He specified the saturated wave amplitude and inferred the magnitude of the eddy diffusion needed to limit wave growth. The convective instability limit given above yields equivalent expressions for the wave drag term and has a stronger physical basis than a prescribed eddy diffusion.

To obtain a non-zero wave drag term, the wave must be dissipated. Saturation commences at the lowest height at which u' equals $U-c$, call that height z_{break} as in Lindzen (1981). Then above z_{break}, the wave amplitude will be constant and equal to $U-c$ as the convective instability acts to remove wave energy whenever $u' > U-c$. The momentum

flux, $\bar{\rho}\ \overline{u'w'}$, can be made a function of the single parameter u' using the relation u'/w' = -m/k (eqn 2.21),

$$\bar{\rho}\ \overline{u'w'} = -\bar{\rho}\ \frac{k\ u'^2}{m\ 2} \tag{2.32}$$

where the factor of 1/2 comes from averaging over a wavelength. The wave drag above z_{break} is

$$-\frac{1}{\bar{\rho}}(\bar{\rho}\ \overline{u'w'})_z = \frac{\overline{u'w'}}{H} = -\frac{k\ u'^2}{2\ m\ H} = -\frac{k(U-c)^2}{2H(N/(U-c))} = -\frac{k(U-c)^3}{2NH} \tag{2.33}$$

for U-c constant above z_{break}. It is clear from this expression that the drag accelerates the mean flow towards the wave phase speed. If U > c the drag slows the mean flow and if c > U, the mean flow is accelerated towards c. As U→c, the wave approaches a critical level where the wave is absorbed and above which mean flow acceleration by that wave ceases. Thus, wave drag produces mean flow acceleration only between zbreak and the wave's critical level.

Lindzen(1981) used the fact that wave induced mean flow acceleration was proportional to U-c to evaluate the Rayleigh friction parameterization that had been previously used to decelerate the mean flow in circulation models. The relation between wave drag and Rayleigh friction has been been discussed by Holton (1983). Since wave drag is

proportional to U^3 it is clear that a Rayleigh drag which is proportional to the first power of U is inadequate. The most recent and most successful Rayleigh drag parameterizations (Geller, 1983) have used a drag coefficient that increases with height which happens to mimic the increase of U with height. Thus the latest drag parameterizations have drag roughly proportional to higher powers of U but cannot completely reverse U. However, wave drag can produce a reversal of U if waves with phase speeds directed opposite to U are saturating. Lindzen's paper has provided a physical basis for a mesopheric drag and such a wave parameterization has been used in the models of Dunkerton (1982, 1983) and Holton (1983) with reasonable success in matching observations of zonally averaged temperature and wind structure.

An alternative approach to wave saturation has been developed by Weinstock (1976, 1982, 1984). Weinstock's theory examines some of the non-linearities that lead to wave dissipation by retaining the $\vec{v}'\vec{\nabla}.\vec{v}'$ term in the perturbation expansion of the total derivative. Weinstock(1976) solves the equations of motion and finds the only difference between his non-linear and the usual linear solution is an imaginary component of frequency, $-id_w$, which he labelled the non-linear damping decrement. With the wave form $e^{i(kx + mz - (\omega - id_w)t)}$, it is easy to

understand the appellation since the wave amplitude decreases by 1/e in a time $1/d_w$. By multiplying d_w by the vertical phase speed, the vertical damping decrement is given as md_w/β and now gives the height increment over which the wave decreases by 1/e (Weinstock, 1984).

d_w is determined from the retained non-linear term, $\vec{v}'\vec{\nabla}.\vec{v}'$, and since $\vec{\nabla}.\vec{v}' = i\vec{k}.\vec{v}'$, d_w is proportional to $\vec{k}.\vec{v}$. The latest expression for d_w is given in Weinstock (1984) as

$$d_w(\vec{v}') \simeq \langle \frac{1}{4}(\vec{K}_1.\vec{v}_1)^2 + \frac{1}{4}(\vec{K}_1.\vec{v}_2)^2 + b(\vec{K}_1.\vec{v}_t)^2 \rangle + K_1^2/\mu \quad (2.34)$$

with $\vec{K}_1$ being the total wavenumber ($\vec{K}_1 = \vec{k} + \vec{m}$) of the wave under consideration. The first term on the right is due to self interaction of the wave. This term is zero in linear theory since $\vec{K}$ is perpendicular to $\vec{v}'$. Weinstock (1982) suggests this term is non-zero for large amplitude (hence, non- linear) waves, though a self-consistent solution actually showing that term to be non-zero has not been presented. The second term is the interaction of the rest of the waves in the gravity wave spectrum with the primary wave and the third term is the interaction of turbulent fluctuations with the wave. b is a dimensionless coefficient, less than one, that accounts for the fact that turbulent time scales are much less than gravity wave periods. The angle brackets denote averaging over the

period of the wave. Weinstock states that the $K_1.v_t$ term includes turbulence generated by the convective instability and therefore, d_w includes the convective instability. Thus, Weinstock(1984) claims this is a 'unified' theory incorporating nonlinear interactions ($\vec{K}_1 \bullet \vec{v}_1$ and $\vec{K}_1 \bullet \vec{v}_2$) and turbulent interactions ($\vec{K}_1 \bullet \vec{v}_t$) with a gravity wave. Perhaps this theory is too unified in that all non-linear interactions, instabilities and turbulence are combined into a single comprehensive variable that can shed no light on the individual physical processes that dissipate atmospheric gravity waves.

This theory appears to be limited to a single wave of wavenumber, K_1. This single wave can be a dominant wave, an average wave or the fastest growing wave in the gravity wave spectrum. The theory is further limited by the dissipation mechanism. It is assumed that the dissipating waves can only put energy into turbulence. Thus wave-wave interactions that could produce wave of different wavelengths or any process that could transfer wave energy to other waves is neglected. Hence, Weinstock's theory is not fully non-linear but applies only to the interactions of a single, dominant wave with other waves leading to saturation or with turbulence to effect a net transfer of energy to turbulent scales.

In applications of this theory (Weinstock, 1984), d_w is determined from observations of the average e-folding height of gravity waves relative to the exponential growth of conservative waves. Knowing d_w, it is possible to calculate the dissipation effects on a spectrum of waves as the waves propagate upward. Since d_w is positive (i.e., there is no generation of waves, only dissipation) the waves will eventually be completely damped. In a model calculation, Weinstock (1984) starts with a stratospheric spectrum dominated by small-scale waves (λ_z < 2 km). In the mesosphere, longer wavelength waves that have been growing exponentially dominate the spectrum while the smaller scale waves have been damped out. However, observations to be presented in section 6.5 show that small scale waves are present at nearly equal amplitudes in the stratosphere and mesosphere. This observation suggests that wave generation is maintaining the small-scale end of the spectrum as compared to Weinstock's theory which removes all small-scale waves.

One interesting aspect of this theory is that once d_w becomes non-zero some wave saturation occurs at all higher heights, not just above z_{break}. Weinstock (1982) determined mean flow acceleration in terms of d_w and was

able to incorporate the width of the gravity wave spectrum in the formulation. He found that the acceleration term varied as $(U-c(K_1))^3$ for a broad spectrum. However, unlike monochromatic saturation theory it is not possible to predict the breaking height or maximum amplitude for a single wave based on that wave's parameters and knowledge of the background stability. Instead, saturation depends on the slope of the wave spectrum, the phase speed of the dominant wave and knowledge of d_w. With saturation occurring throughout the stratosphere and mesosphere, it is irrelevant to determine a z_{break}. The theory does predict that largest values of momentum deposition and mean flow acceleration occur in the upper mesosphere, in agreement with observations and circulation models.

While this theory is a step beyond monchromatic wave theory towards non-linear treatment of atmospheric gravity wave spectra, its reliance on d_w and hence past behavior or the propagating wave spectrum and not on individual wave amplitudes or on the mean atmospheric environment gives it limited value for the present study.

Chapter 3

Wind velocity measurement techniques

Before presenting wind measurements and using those measurements to infer the presence of atmospheric gravity waves, we will examine the techniques used to make such measurements and study the strengths and weaknesses of the methods. The two techniques used in this thesis were rocket and MST radar. A comparison of horizontal wind velocities, simultaneously measured by the two techniques, will be presented in this chapter.

3.1 Rocket techniques

Rockets provide an 'in-situ' measurement of horizontal winds by depositing spheres, balloons, weighted parachutes, or smoke trails in the atmosphere at the desired altitude. Observers on the ground track the motion of the deposited objects. Wind velocities are inferred from the changing positions of the objects. State-of-the-art rocket measurements are made with spheres containing accelerometers. Accelerations of the sphere are recorded and integrated to yield velocity and density changes. Here we will discuss the standard falling chute and the acclerometer techniques.

3.1.1 Meteorological rocketsondes

The meteorological rocketsonde, or metrocket, has been used to obtain stratospheric and mesospheric wind and

temperature measurements since the late 1950's. The sonde itself was developed to be as light as possible so that a small and relatively inexpensive rocket could be used to boost the sonde to maximum altitude. With the present Super-Loki rocket, the sondes are released in the 80 to 90 km altitude range.

After the rocket motor has burnt out, the sonde is drag separated from the motor. A small gas cylinder partially inflates an open Mylar balloon, or retardation device, from which the sonde is suspended. The rocketsonde contains a thermistor and circuitry to sense ambient temperature and a telemetry transmitter. The metalized retardation device provides a target for the ground-based tracking radar to lock onto. Radar is used to track the falling sonde from the release altitude (80 - 90 km) until the sonde reaches an altitude near 20 km. The total tracking time is approximately 45 minutes.

While the balloon is falling, a minicomputer records the radial coordinates of the sonde and the telemetered thermistor readings every .1 secs. Processing of this data follows the procedure given in the Federal Meteorological Handbook #10 (FMH 10, 1975) except for the second smoothing as described below. Rocketsonde positions in radial coordinates (range, elevation angle and azimuth) are first smoothed with a 101 point, symmetric, low-pass filter (FMH

10, p.I-62) and then converted to Cartesian coordinates to obtain the horizontal positions and heights of the temperature estimates. Differences between successive recorded positions are used to compute the wind velocity. The conversion from position changes to wind velocity is complicated by the fact that atmospheric density changes by several orders of magnitude over the path of the falling sonde. As the density changes so does the ability of the wind to change the position of the sensor. In other words, the drag coefficient of the falling balloon changes with altitude.

An expression for the varying drag coefficient was derived by Eddy et al. (1965) by solving the equations of motion including a drag term proportional to the square of the difference between the sensor velocity and the wind velocity. By assuming vertical wind velocity (usually < 1m/s) to be small relative to the vertical sonde velocity (about 200 m/s) they obtained a drag coefficient proportional to the difference between the vertical acceleration of the sonde and the acceleration due to gravity, g. If the sensor is accelerating at g, the atmosphere has little effect on its motion, while if the sensor is accelerating more slowly than g the sensor is relatively more sensitive to the wind. These considerations have led to the designation of the altitude

of maximum fall velocity as the maximum altitude of reliable wind data, i.e., as the fall velocity decreases due to increasing atmospheric density, the drag coefficient is increasing and the retardation device is more sensitive to the wind.

With the drag coefficient determined from vertical sensor velocity and acceleration, the measured horizontal winds can be corrected for the varying sensor response to the wind. The corrections are proportional to the inverse of the differences between the sensor acceleration and g. As the sensor acceleration approaches g the correction becomes larger and would be infinite for an acceleration equal to g. Overly large correction terms were occasionally observed in the metrocket data to be reported. Possible causes of unusually large accelerations are tangling of the parachute lines partially collapsing the parachute, oscillation of the chute and attendant alteration of the area presented by the chute in the direction of the falling sensor, and forces not accounted for in the drag coefficient formulation (Eddy et al., 1965).

The low-pass filter was used again, this time to smooth the computed velocities. This step was found to eliminate unusually large correction terms. Next, corrected velocities were computed using the smoothed vertical

accelerations and velocities as discussed above. These corrected velocities were averaged over kilometer layers between integral values of height (for example, all data between heights of 62 and 63 km were averaged together). Finally, adjacent one kilometer wind velocity averages were averaged to produce wind estimates at each integral height value. These averaged velocities are used in the velocity comparisons presented later in this chapter, and similiar data has been used in climatological middle atmosphere charts such as the one shown in Figure 1.1.

3.1.2 Tri-axial accelerometers

State-of-the-art, in-situ measurements of horizontal wind velocities, turbulence intensity and atmospheric density are made with piezo-electric accelerometer packages. The sensor consists of three piezo-electric accelerometers arranged to measure accelerations along three orthogonal axes. This instrument is rigidly mounted inside a .25 m diameter metallic sphere which also contains a transmitter to telemeter the accelerometer data to the ground during flight. The sphere is carried to the upper atmosphere atop a rocket booster.

Here we will specifically discuss the flight of such a payload during the STATE (STructure and Atmospheric Turbulence Environment) campaign of June 1983 launched from Poker Flat, though other accelerometer flights are

similiar. The sphere separated from the booster at a height of 75 km and continued upward to a maximum altitude of 130 km. This section of the flight is termed the upleg. Useful data were also obtained from the downleg portion of the flight from 130 to 55 km. Altitudes were determined from ground-based radar tracking data. During its flight, the sphere was spinning with a frequency of 4 Hz about one of the accelerometer axes. This spin was imposed to keep the package stable and hold the orientation of the accelerometer axes fixed.

The raw data from the accelerometer sphere consisted of measured accelerations along the three axes of the instrument. The conversion from accelerometer axes to Cartesian coordinates is complicated by the fact that accelerations due to density changes are along the sphere trajectory and the orientation of the trajectory relative to the accelerometer axes changes during flight. The angle between the spin axis and the trajectory is determined to be that angle which maximizes the agreement between the upleg and downleg density accelerations. This can only be done for horizontally homogeneous density fluctuations. Once the angle between the spin axis and the trajectory is known, accelerations due to density changes can be estimated and removed from along all three axes leaving accelerations caused by horizontal winds. Density

measurements are obtained from the estimated component of acceleration parallel to the trajectory and empirical knowledge of the drag coefficient of the sphere. Temperature are obtained through use of the hydrostatic equation, the equation of state and integration of the density measurements (Philbrick et al., 1978).

The height resolution of the instrument was degraded by the failure of the package to achieve a spin rate of 6 Hz. The slower spin frequency resulted in independent estimates of acceleration being further apart. This problem and the desire to ensure horizontal homogeneity led to a smoothing of the data that severly damped fluctuations with scale sizes smaller than 2 km. Thus, only large-scale waves can be identified in the rocket data.

Another less serious difficulty arose because there was both up and downleg data only from heights of 75 to 130 km. The lack of upleg data from 55 to 75 km meant that the density accelerations could not be accurately obtained in this interval. The accelerations could be calculated from knowledge of the trajectory and accelerometer axes but the analysis is much more complicated and was not carried out for this data set. The measured densities were continued from 75 to 55 km by extrapolation using an exponentially increasing density function, but this yields a mean density estimate only. Since accelerations due to changes in

density were not removed, it is possible that the wind fluctuations are overestimated below 75 km.

3.2 MST radar technique: Poker Flat MST radar

The MST wind velocity measurement technique employing coherent backscatter radars is reviewed in Balsley and Gage (1980). Basically, turbulent mixing of the humidity and potential temperature gradients in the troposphere and stratosphere and mixing of the electron density gradient in the mesosphere produces fluctuations in the radio refractive index. Refractive index fluctuations with scale sizes of half the radar wavelength meet the Bragg scattering condition to coherently reflect a small portion of the transmitted radar signal back towards the radar. Motion of these turbulent eddies along the radar beam causes a Doppler shifting of the returned signal, which can be detected by the radar.

The Poker Flat facility was described by Balsley et al. (1980) while the radar was under construction. The system presently consists of a square antenna field, 200m on a side, which is split into 100m square quarters. Each quarter contains two sets of orthogonal planar arrays of coaxial, collinear dipole antennas. Each set of antennas is electronically phased to point at a specific zenith angle. Three of the quarters have one set phased to direct the maximum lobe of the beam pattern 15^{o} off-zenith towards

an azimuth of 64° east while the orthogonal set in those quarters is phased to point towards an azimuth of 334° east. The 64°E beam will be called the east beam and the orthogonal beam will be called the north beam for convenience. Since the radar transmits and receives on the same antenna, it is appropriate to state that the two-way beam width of the oblique beams is 1.1°.

The fourth quarter antenna set, having the same polarization as the north beam, is phased to direct the maximum lobe of the pattern vertically. Though the main lobes of the north and this vertical beam are separated by 15°, beam sidelobes may coincide. Since antenna polarization is the same, the possibility of cross talk between beams arises. Such crosstalk does exist, as will be discussed in section 3.2.2. Since only 1/4 of the antenna field is used for the aperture of the vertical beam, its two-way beamwidth is 2.2°.

The oblique beams are nominally run with a combined transmitter output of 800 kW per beam to the antenna. The vertical beam uses 1/3 the number of transmitters used in either oblique beam. In normal operation, a 16μs pulse is transmitted once every interpulse period (IPP) of 850μs. The usual 16 μs pulse length gives a range resolution of 2.2 km since the returned signal is an echo average extending over the spatial region covered by the

transmitted pulse. The detected signal is sampled at delays corresponding to 2.2 km height intervals after every pulse. Pulselengths of 2, 4 and 8 μs can also be transmitted corresponding to spatial resolutions of 300m, 600m, and 1.1 km.

3.2.1 Radial velocity determination

Here we will examine the processing used to convert the Doppler shifted signal into a radial velocity in order to determine the effect of this processing on the computed velocities. The Doppler shifted signal is sampled at delay times corresonding to selected heights or distances from the radar.

Since the Doppler shifted frequencies are small and the atmosphere is stationary for periods of a second, samples from consecutive pulses, received from the same height, are 'coherently' integrated. Coherent averaging improves the signal to noise ratio and also sets the sampling interval at 1 / (NCI x IPP), where NCI is the number of coherently integrated, consecutive samples. Sampling and coherent integration continue until 2^n coherently integrated, complex points are acquired. Then, the mean value of the 2^n point time series is subtracted from each series. This mean or DC component is due to a receiver offset or to ground clutter, which is a non-Doppler shifted return signal coming from surrounding hills, towers and other

stationary reflectors. After eliminating the DC component, a Hanning window (cosine arch) is applied to the time series to reduce the sidelobe level of the signal after the time series has been Fourier transformed. Then a complex Fast Fourier Transform (FFT) is performed on the 2^n points. A typical spectrum is shown in Figure 3.1. In practice, several of these spectra are averaged to further improve S/N and reduce the amount of data written to tape.

The frequency range covered by the spectrum is determined by the Nyquist (or highest) frequency contained in the time series. The Nyquist frequency is 1 / (2 x sampling interval) or 1 / (2 x NCI x IPP) in cycles/sec. The frequency resolution of the 2^n spectral points resulting from the FFT is determined by the length of the time series. Thus, frequency resolution is 1 / (2^n x NCI x IPP). Once the time series has been transformed to the frequency domain it can be interpreted in terms of velocity using the relation between Doppler shifted frequency (f) and radial velocity (v_r), $f = 2 v_r / \lambda$, where λ is the radar wavelength.

During routine operation, the Poker Flat MST radar switches alternately between an oblique intergration and a vertical integration cycle. Oblique integration cycle samples are coherently integrated for 0.05 s (= (NCI of 58) x 850 μs pulse periods) until 64 such points are obtained.

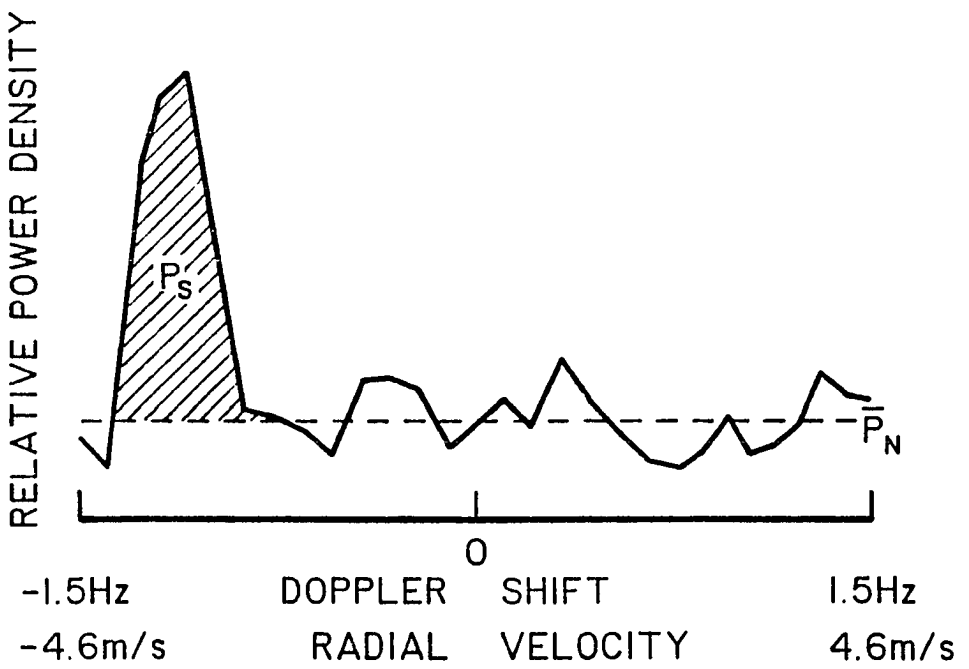

Figure 3.1 Typical Doppler power spectrum obtained by the Poker Flat MST radar.

The resultant Fourier spectrum covers the velocity range from -30 m/s to +30 m/s. With 64 points the velocity range per point is 0.95 m/s. This resolution is not adequate to accurately measure vertical velocities which are on the order of centimeters per second. During alternate cycles vertical coherent integration is done for 0.35 s. A 64 point Fourier transform covers the range from -4.3 to +4.3 m/s and individual point resolution is 0.13 m/s. These integration times have been found to cover the usual range of mesospheric, stratospheric and tropospheric velocities as well as allow the spectrum to be wider than the signal width.

The first three moments of the spectrum are computed in real time and stored on tape along with mean noise power. The three moments are (Woodman and Guillen, 1974); signal to noise ratio , S/N; mean radial velocity; and the width of the signal. S/N is just the area of the signal peak above the mean noise level (hatched area labelled Ps in the figure) divided by the total noise power (total area under the average noise level, Pn). Mean velocity is found by computing the integral of power-weighted velocity, i.e.,

$$\langle v_r \rangle = \frac{\int P_s \, v_r \, dv_r}{\int P_s \, dv_r} \qquad (3.1)$$

which allows velocity to be computed to greater precision than the spectral point resolution.

The processing sequence of DC filtering and windowing has been found to introduce a bias into velocity measurements. The bias is greatest for velocities nearest 0 m/s. We will examine this problem in the frequency domain considering the frequency spectrum centered at 0 Hz shown in Figure 3.2A. The noise is definitely non-random but useful for illustration and the actual signal introduced on top of the noise is shown by the dashed lines. Note that a large DC component has been included.

The DC filtering, or subtraction of the mean, removes all power at the zero frequency point leaving a deep notch in the spectrum, as in Figure 3.2B. The Hanning window applied in the time domain is equivalent to a convolution of a (1/4, 1/2, 1/4) weighted three-point filter in the frequency domain. The result of this convolution is shown in Figure 3.2C where it is seen that the notch has been widened. Since for small velocities, the DC filtering removes a portion of the signal power, the spectral point at 0 Hz is set equal to the mean of the adjacent points as has been done in Figure 3.2D. The result of this processing is an apparent shift of the mean velocity away from zero and an under-estimation of the signal power. The introduced signal gives a velocity of 1 point to the right

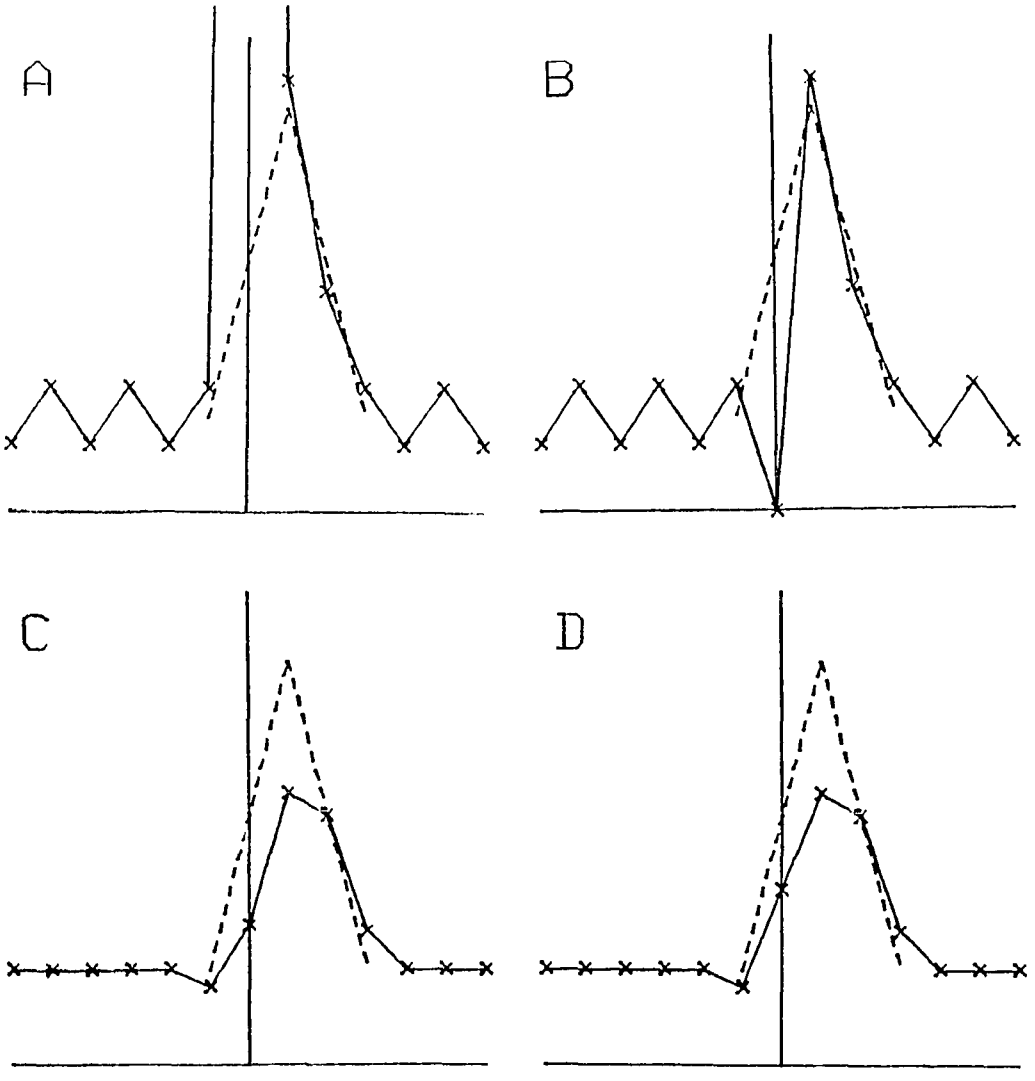

Figure 3.2 Schematic illustration of the effects of DC filtering and Hanning windowing on a power spectrum. A) Raw power spectrum with triangular shaped signal and large spike at 0 m/s or DC. B) Spectrum after removal of DC. C) Spectrum after windowing. Note loss of signal at 0 m/s point. D) Spectrum after DC point has been interpolated. Signal was designed to yield a velocity of 1 but processing has shifted the observed velocity to 1.34.

of zero if the DC spike was not present, whereas integration of the processed spectrum puts the velocity 1.34 points to the right of zero.

This bias against zero velocities has been observed in the Poker Flat radar data. The frequency distribution of velocities from heights at which only noise was present was determined. In a white noise spectrum, the signal finding algorithm selects the highest noise spike as the signal. Since this highest noise spike would be randomly distributed over a large number of such noise spectra, a uniform distribution of velocities would be expected. This is approximately what is found in the actual distribution shown in Figure 3.3. The displacement of velocities near 0 m/s away from 0 m/s is readily apparent. The notch at 0 m/s is approximately 5 spectral points wide (at the level of the uniform distribution) as would be expected from a 3 point smoothing filter.

The effect of this notch on the distribution of actual velocities can be seen in Figure 3.4, which is the distribution of velocities obtained from signals significantly above the noise threshold. Again, there is a distinct notch at 0 m/s in an otherwise Gaussian distribution.

This bias against near zero velocities is compounded by coarse frequency or velocity resolution. With spectral

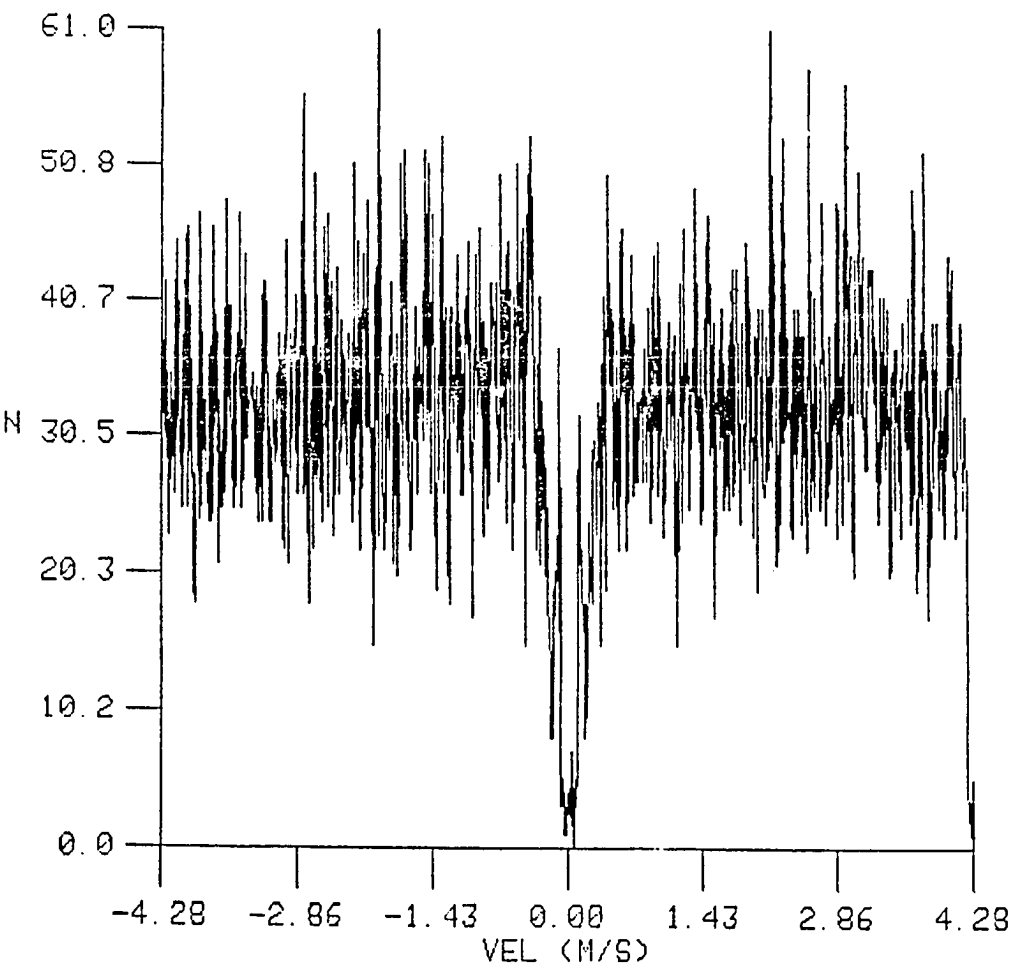

Figure 3.3 Nearly uniform distribution of velocities estimated from heights at which only noise is present. Vertical axis is number of points with velocities in each 0.01 m/s bin.

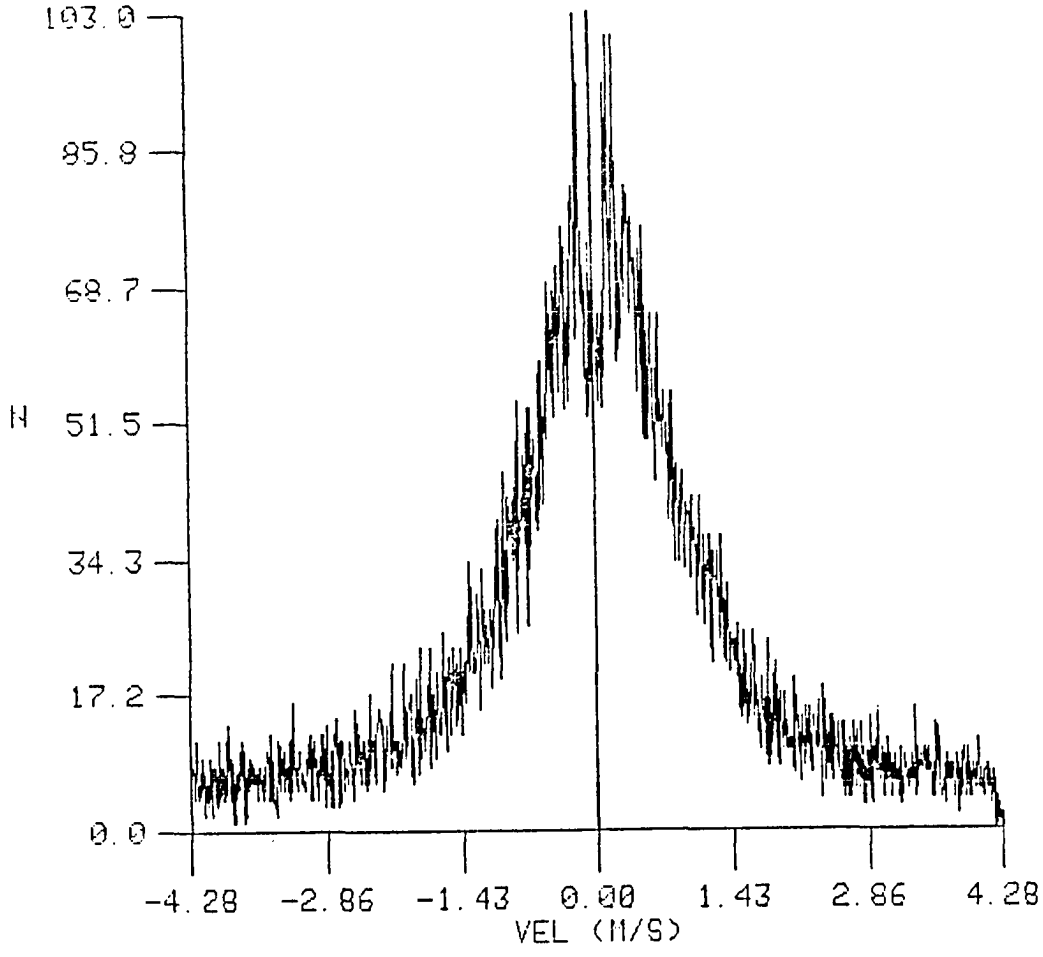

Figure 3.4 Distribution of mesospheric vertical velocities measured by the Poker Flat MST radar over days 92 to 96, 1983 . Note the small notch near 0 m/s in an otherwise Gaussian distribution.

resolution of 1 m/s, the displacement away from 0 m/s will be greater than for resolution of .1 m/s intervals. That displacement away from 0 depends on frequency resolution is shown in Figure 3.5. In this figure, two distributions with velocity resolutions of 1/8 and 1 m/s are overlain. These distributions were acquired simultaneously and were constructed using vertical velocities measured during vertical integration cycles for the finer resolution and vertical velocities measured during oblique integration cycles for the poorer, 1 m/s, resolution distribution. The only difference between the two distributions is the number of coherent integrations and thus the frequency resolution, since they were acquired at the same time, same heights and with the same radar system.

The variance of the lower resolution distribution is greater than the higher resolution distribution. Since variance is equal to the integrated power spectrum, the larger variance implies that there will be a corresponding increase in the power spectrum of near-zero vertical velocity fluctuations. Effectively, noise is added to any time or height series with the noise amplitude increasing as the velocity approaches zero.

The change in variance due to velocity resolution can be estimated from plots like Figure 3.5. To do this, we form the ratio of widths of the distributions at the half-

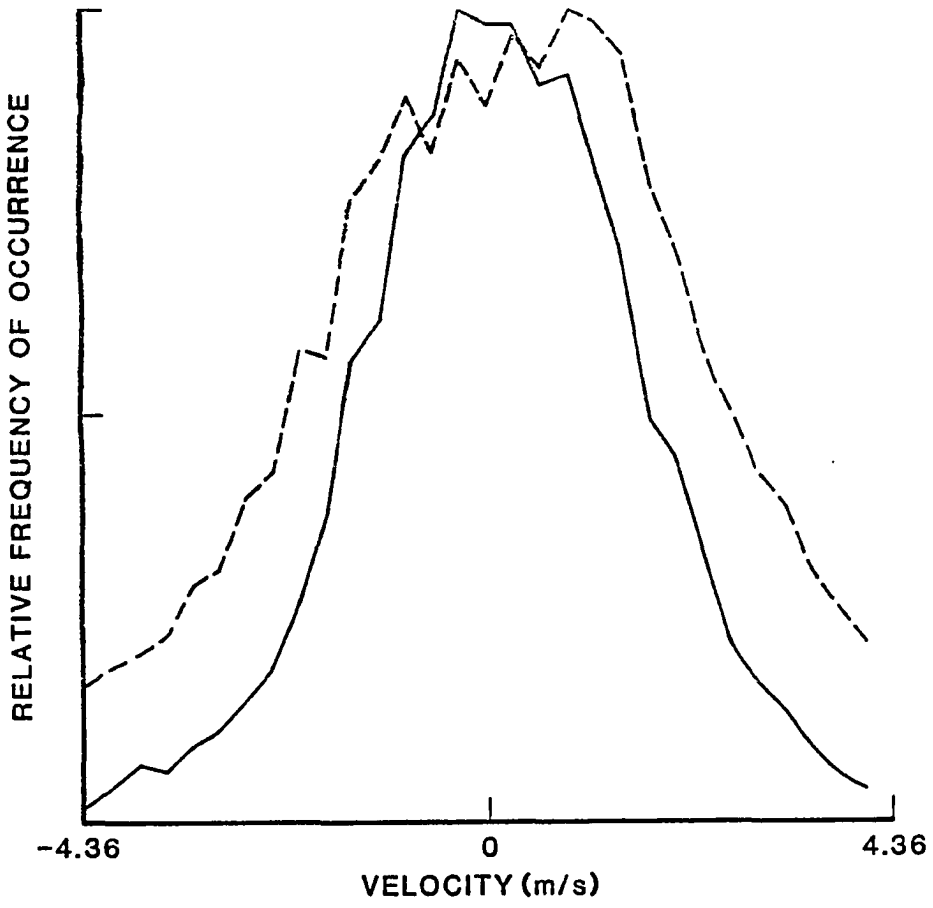

Figure 3.5 Distributions of vertical velocities simultaneously obtained with resolutions of 1.1 m/s (dashed) and 0.14 m/s (solid) per Doppler spectral point. Note the flattening of the peak and widening of the distribution with the coarser resolution.

height points. For a Gaussian distribution the width would be proportional to the standard deviation. Hence, squaring the ratio yields an approximation to the ratio of the variances. The squared ratio was found to range between 2 to 12 with the ratio being inversely proportional to the width of the higher resolution distribution. This is due to the fact that the velocities nearest zero are affected the most. Thus, the narrower the distribution, the greater the effect of the the processing and the larger the enhanced distribution of the low resolution data. For summer mesospheric velocities the ratio was about 2, the winter mesospheric ratio was about 4. The largest ratios were found for tropospheric vertical velocities.

3.2.2 Cross talk

Since the vertical and north antenna arrays have the same linear polarization (i.e., their dipoles are all parallel to an approximately east-west line) the possibility of signals from one beam interfering with signals on the other exists. As stated before, the two-way half-power beamwidths of the principal lobe of the vertical beam is 2.2^{o} while that of the north beam is 1.1^{o}. The phasing of the north antenna directs the principal lobe 15^{o} away from vertical towards the north. Thus, the two narrow main beams are widely separated in space and do not directly interfere with each other. However, an array of

uniformly driven antennas spaced at half wavelength intervals will have sidelobes with the first one being down only 13 dB from the main lobe on a one-way pattern.

Figure 3.6A is an idealized antenna pattern of two beams corresponding to the vertical and north beams of the Poker Flat radar. These are one-way patterns because we are here concerned with transmitting on one beam and receiving unwanted signals on the other beam. Note that this is a reciprocal diagram since transmit and receive beams are identical. This figure is in a log scale and simple addition of the two curves at any angle yields the combined pattern with crosstalk sidelobe levels as shown in Figure 3.6B. Figure 3.6B shows two maxima in the crosstalk pattern which correspond to transmission along a main lobe with reception through a sidelobe of the second beam and to transmission through a sidelobe of the transmitting beam with reception on the main lobe of the second beam. The maximum crosstalk level is about 26 dB. That is, any signal that is 26 dB above the noise in one beam will appear as a signal just above the noise level in the other beam.

Data demonstrating that crosstalk exists came from the STATE campaign which will be discussed in detail in chapter 4. During the period of the campaign, the radar would alternately transmit on oblique and vertical beams. For 90

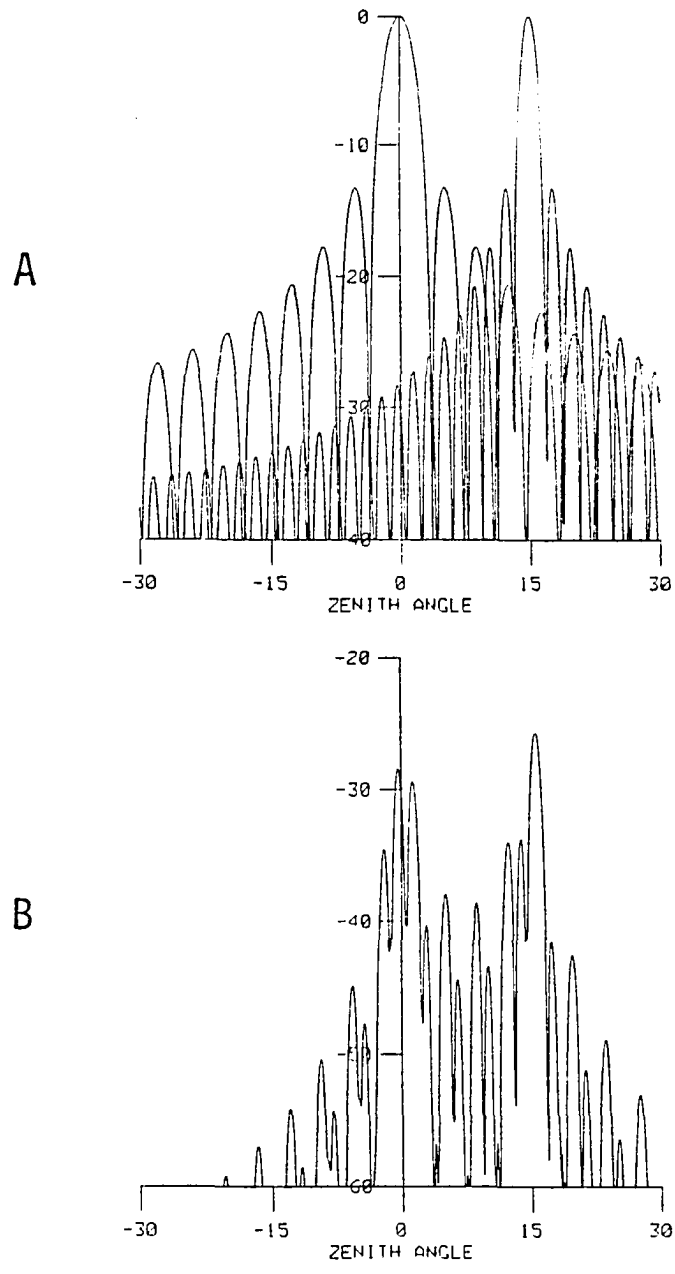

Figure 3.6 Idealized beam plots of the Poker Flat radar north and vertical beams. A) Antenna beam pattern of the north (maximum at 15° zenith angle) and the vertical beams. Vertical axis is in dB relative to the peak. B) Crosstalk pattern obtained by multiplying vertical and north patterns together. Note that the crosstalk beam has maxima at the approximate pointing angles of the north and vertical beams.

seconds, pulses were transmitted only along the oblique beams after which processing of the Doppler signal spectrum received from all three beams was performed. Then the oblique transmitters were turned off and the vertical beam turned on. Again, the signals received on all beams were processed. With this mode of operation, crosstalk would be evident if signals appeared in a beam that was not transmitting.

Crosstalk was discovered by comparing the S/N ratio measured in the transmitting beam with the S/N in the other beam at the same delay or range. This is shown in the scatter diagrams of Figures 3.7 and 3.8. The large concentration of points in the lower left of each plot comes from times when neither beam was receiving signals above the noise level. As signal strength in the main lobe of the transmitting beam increases up to about the 5 dB level, the S/N seen in the other beam is constant and near the noise level. For signals above 5 dB, the beam that is not transmitting begins to receive signals from the beam that is transmitting. The relationship between signals received from the main lobe of the transmitting beam to the signals received in the other beam is linear and direct. The only difference between the two beams is a decrease of signal strength by about 18 dB. This correspondence is between observations at the same range in both beams as

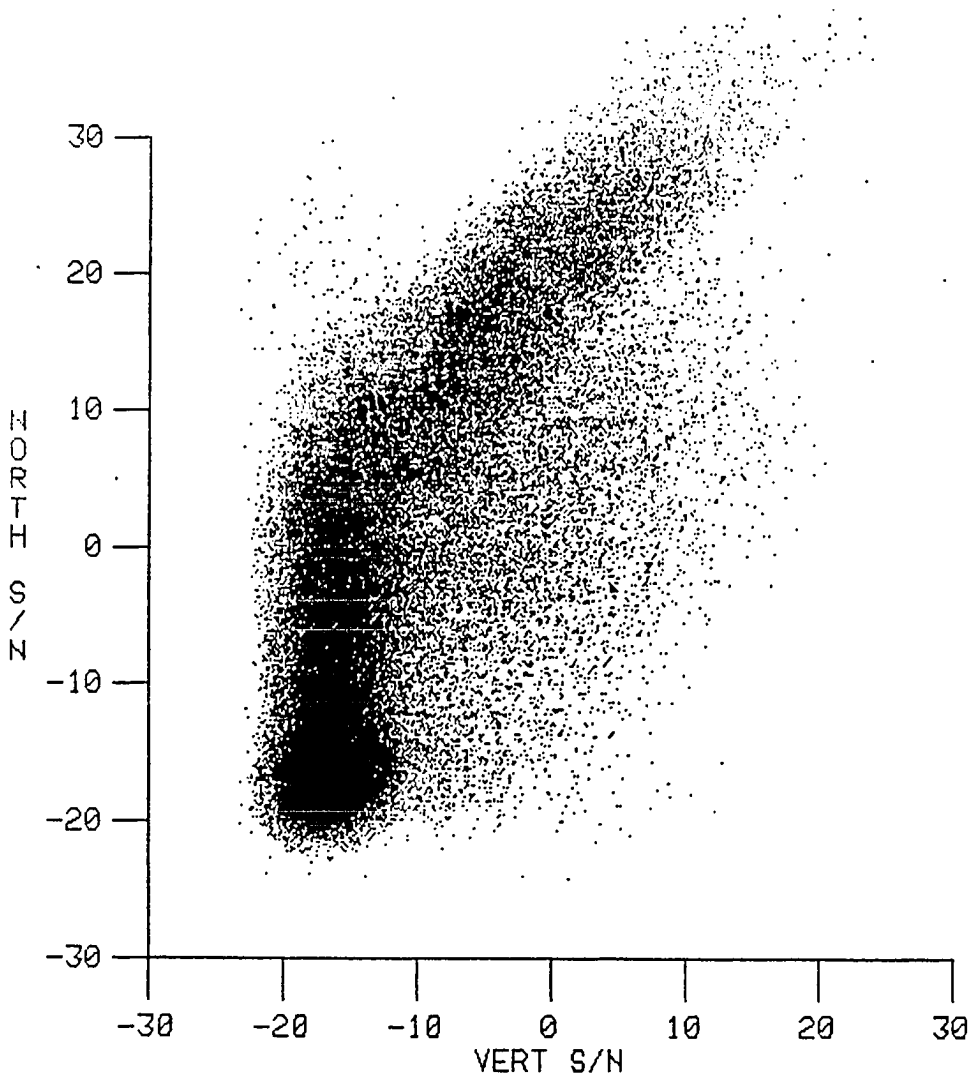

Figure 3.7 Scatter plot of signal strength received simultaneously on north and vertical beams during STATE campaign. These data are from periods when only the north was transmitting.

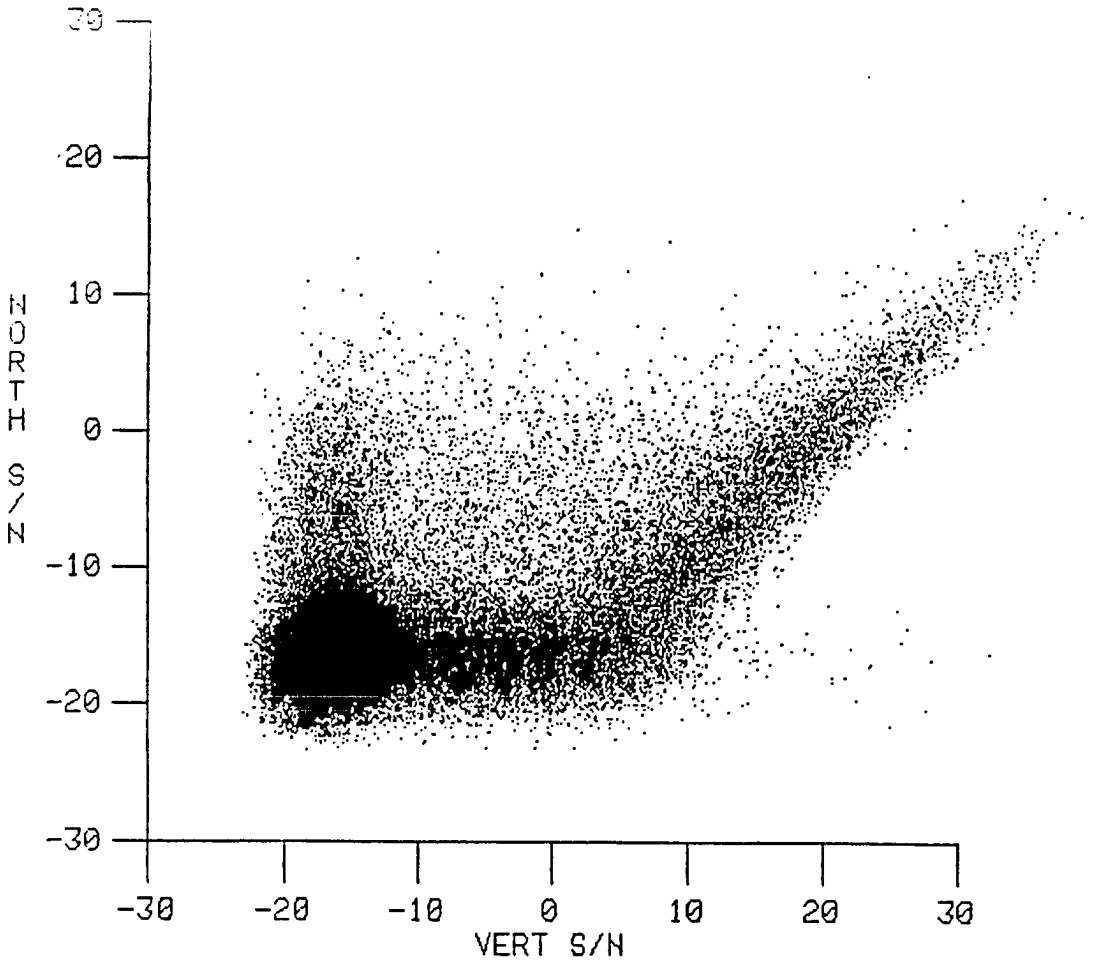

Figure 3.8 As in Figure 3.7, except that only periods when the vertical beam was transmitting are used.

would be the case for crosstalk between the transmitting beam main lobe and a receive beam sidelobe pointed along this main lobe. In this situation, both beams are simultaneously sampling the same volume.

A similar, but less distinct, relationship is observed by comparing signals received from equal heights. Crosstalk at equal heights would be manifest by pulses transmitted from a sidelobe along the main beam of the non-transmitting antenna. The equal height comparisons produce scatter plots nearly identical to Figures 3.7 and 3.8 except that the diagonal branches are broader and less well-defined. This behavior is to be expected because the vertical and north beams are separated by 23 km at an altitude of 85 km and are sampling different volumes. The signals from these separated volumes are not perfectly correlated, which causes the greater scatter in the diagonal branches.

The observed crosstalk level of -18 dB is larger than the -26 dB lobe shown in Figure 3.6B. However, the patterns in that figure are true only for an ideal antenna with dipoles ideally spaced and with perfect phasing to direct the beams. Those patterns also neglected ground reflections which can have effects on beam direction, width and sidelobe pattern. Rather, Figure 3.6B should be viewed as an indication that crosstalk is possible and that the

main crosstalk beams will be roughly aligned with the main lobes of the individual patterns.

This inherent interference between beams is to be considered whenever examining Poker Flat MST radar data. Signals from the winter mesosphere are less than 20 dB above the noise level on average (Ecklund and Balsley, 1981) and thus crosstalk has little effect. However, signals from the summer mesosphere have reached levels 50 dB above noise and certainly crosstalk must occur. One way of eliminating crosstalk is to alternately switch from transmitting obliquely to transmitting vertically and only using velocities obtained from data with the correct beam on, as was done during the STATE campaign.

It seems likely that, in general, the effect of crosstalk is minimal. Frequently, signals from the stratosphere and mesosphere are of equal magnitudes in the vertical and oblique beams despite the fact that the vertical system is some 10 dB less sensitive than the oblique system. For equal amplitude signals, crosstalk will add interference roughly 20 dB below the peak S/N. If north and vertical velocities are similiar, the signal from the opposite beam could distort the actual signal causing small errors in computed S/N and Doppler shifts. If the velocities are separated by a few m/s, the crosstalk signal would be perceived as noise added to the spectrum at a

level 20 dB below the actual signal and would only lead to a small decrease in S/N. Thus, the effect of crosstalk is usually minimal but may be important if there is a large difference in signal strength between the two beams and if the two radial velocities are similiar. In this thesis, crosstalk effects have been avoided either by alternating transmit beams or using winter data when S/N is seldom strong enough to induce crosstalk.

3.3 Comparisons of rocket and radar measured velocities

In this section, three sets of velocities measured by rockets are compared with Poker Flat MST radar estimates of wind velocities. All of these comparisons are of horizontal velocities alone, since vertical velocities are not measured by rockets. The first two comparisons are made with metrocket derived winds and have been published by Smith and Fritts (1984). The third comparison is made with data from an accelerometer sphere launched during the STATE campaign.

For the metrocket comparisons, the radial velocities measured by the radar were converted to zonal and meridional velocities under the assumptions of horizontal homogeneity and no vertical wind. By assuming horizontal homogeneity, it was possible to rotate the radar coordinate frame (334^{o}E and 64^{o}E) to the usual meridional and zonal coordinate system (0^{o} and 90^{o} E). The zero vertical wind

assumption was made in order to convert from radial to horizontal velocities. Vertical winds, measured with the vertically directed radar beam, were generally in the -1 to +1 m/s range while radial velocities along the oblique beams were in the 5 to 15 m/s range. The radial velocity in either oblique beam was a composite of the vertical wind times the cosine of 15^{o} (= .97) plus the horizontal wind, along the azimuth of the beam, times the sine of 15^{o} (= .26). Since the vertical wind was assumed to be zero, the conversion from radial to horizontal velocity was made by dividing by the sine of 15^{o} or equivalently, multiplying by about 4. Given the $\pm$ 1 m/s range of vertical velocities, it is obvious that this conversion could yield a horizontal wind differing from the actual wind by $\pm$ 4 m/s.

The observed wind profiles shown in Figures 3.9 and 3.10 indicate good agreement between the two techniques. The radar data points represent two different averaging intervals. The dots are spectral averages obtained once a minute. The vertical bars correspond to further averaging over nine of the 1 minute spectra. Spectral averaging effectively averages velocities weighted by signal strength, which accounts for differences between the 9 and 1 minute average points. The 1 minute dots give an indication of the variability of the measured winds. The longer 9 minute averaging improves signal detectability by

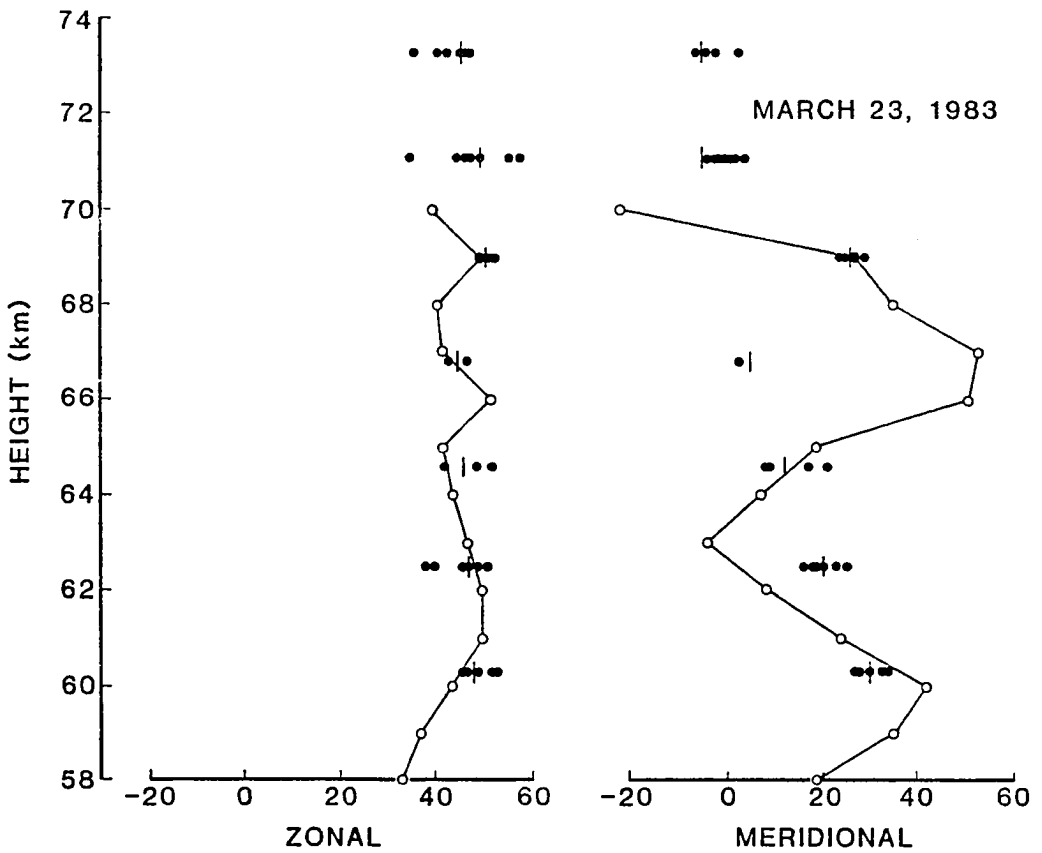

Figure 3.9 Rocketsonde (open dots) and Poker Flat MST radar wind profiles (in m/s) obtained at 1630 local time, March 23, 1983.

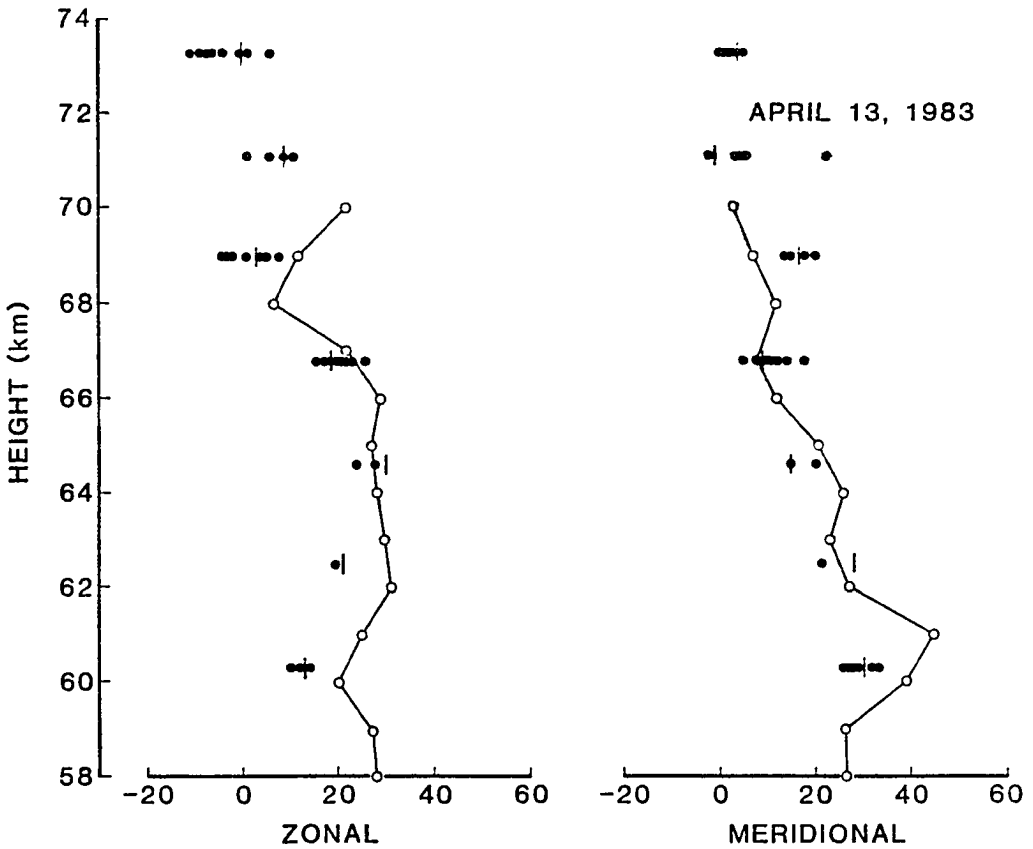

Figure 3.10 As in Figure 3.9, obtained at 1630 local time on April 13, 1983.

a factor of 3 and removes contamination of horizontal velocity estimates by vertical motions with periods less than about 10 minutes. Note that the rocketsonde fell through the 70 to 60 km region in about 1 minute.

Uncertainty in observed winds is about 5 m/s using rocketsondes and about 1 m/s for the MST radar technique (Gage and Van Zandt, 1981). With the 4 m/s 'error' introduced by assuming the vertical wind was zero, the uncertainty in both techniques is approximately 5 m/s. Clearly, most of the differences between the rocket and radar profiles are smaller than 10 m/s and well within the uncertainties given above.

Still there remain unexplained differences, most notably in the meridional component on March 23. The rocketsonde reveals a 30 m/s amplitude fluctuation with a vertical wavelength of 7 km that is not evident in the radar profile. The different spatial resolutions used in the two measurements are not sufficient to explain the difference. The MST radar winds are averages over 2.2 km thick volumes, while the metrocket data has resolution of approximately 1 km. A 7 km fluctuation would be reduced by only 25% due to the greater spatial averaging of the radar.

The most likely explanation of the discrepancy is that the rocket sampled the winds in a region 30 - 50 km north of the radar sample volumes. It is possible that a

vertically propagating gravity wave was sampled by the rocketsonde and was horizontally localized so that the radar did not 'see' it. Some credence is given to this interpretation by the fact that the mean of the rocket and radar derived profiles are nearly identical.

Analysis of the rocketsonde temperature data suggests that the amplitude of the velocity wave is perhaps an artifact of the filtering or due to a nonlinear response of the parachute to the actual wind field. The temperature profile exhibits a wave with a vertical wavelength similiar to the velocity wave. However, linear gravity wave theory and the temperature fluctuation amplitude suggests that the velocity fluctuation is a factor of 2 too large. With this discrepancy and the spatial separation of the radar and rocketsonde it is not possible to completely explain the differences between the two techniques.

To compare the radar and accelerometer winds, the horizontal winds measured by accelerometers have been converted into radial velocities that would be measured by the radar if there were no vertical wind. The meridional and zonal winds from the rocket were converted to radar coordinates for convenience. The component profiles are presented in Figure 3.11. Again, vertical velocities were in the $\pm$1 m/s range and could cause a $\pm$ 1 m/s difference in the compared velocities. Note that profiles obtained every

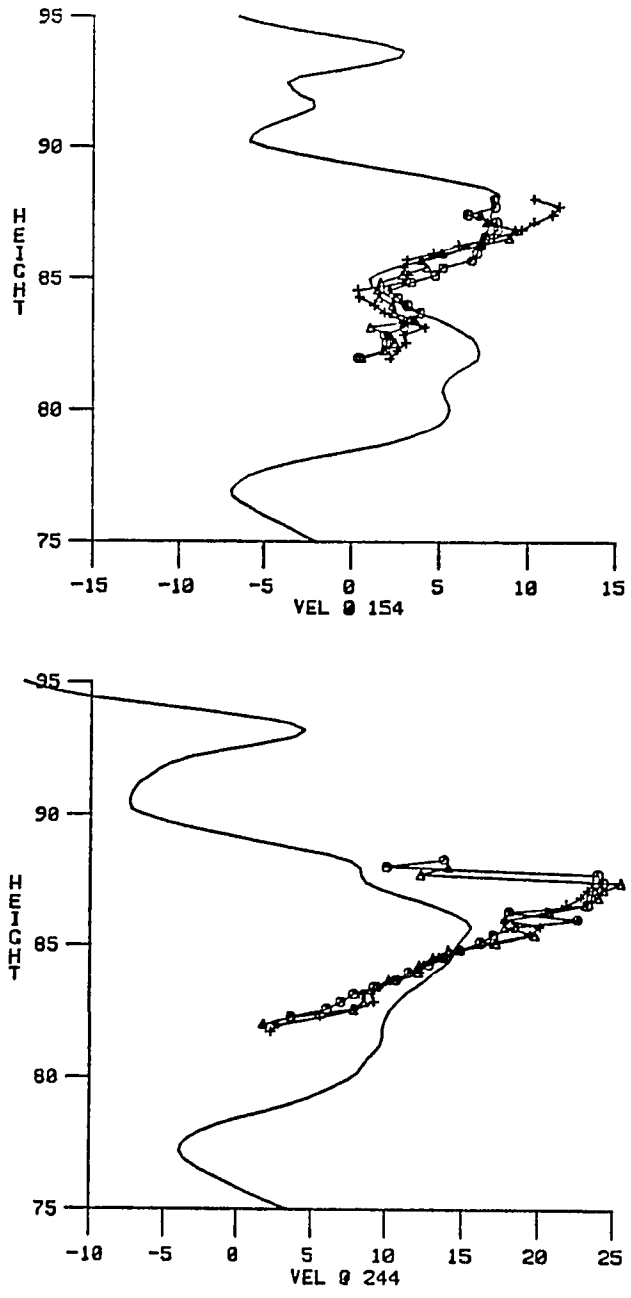

Figure 3.11 Accelerometer derived winds (smooth curves) and Poker Flat MST radar wind estimates obtained at 2055 local time, June 15, 1983. Upper plot is for winds directed opposite to the north beam and lower plot is for winds directed opposite to the east beam.

84 s by the radar are plotted from times during the 5 min that the sphere was in flight.

The two measurements were made simultaneously in time but not in space. The rocket was launched at an azimuth of 5^{o}E. At a height of 85 km on the upleg, the sphere was about 15 km from the 85 km altitude radar sample volume in the north beam and about 25 km away from the east beam. The downleg sampling was even farther north of the radar. This spatial separation allows the possibility of intervening small-scale waves that would produce differences in the otherwise general agreement between the two profiles. Also note that the rocket winds have been low pass filtered to remove fluctuations with vertical wavelengths less than 2 km.

It has been shown that on three separate occasions and with two different types of rocket techniques, the radial winds measured along the oblique beams in the mesosphere generally agree with rocket-derived measurements of the horizontal wind field. The same cannot be said about the vertical winds measured by the radar since there is no other technique that measures vertical winds. However, a comparative study between tropospheric and stratospheric vertical winds measured by the Poker Flat MST and the Chatanika radar operating at a frequency of 1290 Mhz (23 cm

wavelength) by Watkins and Jayaweera (1985) showed that both radars measured essentially the same vertical wind field. Thus, the Poker Flat MST radar is a reliable tool for obtaining atmospheric wind measurements. It should be noted that MST radars have the unique ability to perform high time resolution studies of the wind field, which can be complemented by rocket measurements of the temperature field to provide an almost complete description of atmospheric dynamics. The two techniques are complementary and every effort should be made to conduct simultaneous rocket and radar measurements for the detailed study of atmospheric dynamics.

Chapter 4

Simultaneous rocket and radar observation of summer mesospheric internal gravity waves

Since the Poker Flat MST radar began operating, strong signals have been received from a narrow height region near the mesopause during summer months. Signals during the winter months originate over a broader height interval and are significantly weaker. The signals are due to returns from spatial irregularities in the radio refractive index with scale-sizes of half the radar wavelength or 3 m for the Poker Flat radar. In the mesosphere, these irregularities are the result of turbulent mixing of the electron density gradient.

The intensity and location of the echoing regions were examined by Balsley et al. (1983), with the conclusion that the summer echoes were most likely due to dynamic instabilities near the mesopause resulting from the vertical compression of tidal and low-frequency gravity waves as they approached the strongly stable region above the mesopause. This conclusion was based on modelling of the wind shear due to vertically propagating 24 and 12 hr tidal modes and a 16 hr period wave that had been identified through spectral analysis of the radar wind measurements. These waves appeared to be sufficient to explain the occurrence of narrow regions of strong

turbulence near the summer mesopause. However, Balsley et al. were unable to make any statements about the strength of the electron density gradient. Several rocket observations have shown a steep gradient of electron density near the mesopause, but simultaneous wind and electron density measurements were not available to completely pinpoint the echoing regions. Balsley et al. suggested that concurrent rocket/radar measurements were needed under a variety of conditions to finally determine the precise nature of the strong radar echoes.

Concurrent rocket/radar measurements formed the basis for the STATE (STructure and Atmospheric Turbulence Environment) campaign performed in June of 1983. The STATE program was designed to measure the electron density gradient, turbulence intensity down to 1 m scales, neutral atmospheric density and the radar echo strength to hopefully provide measurements over extensive height and time domains, which would allow identification of the agents responsible for the enhanced radar echoes. Four instrumented payloads were launched into the middle atmosphere to measure electron density, turbulence intensity, temperature and wind velocity profiles.

In this chapter, data from an accelerometer sphere flown from the Poker Flat Research Range on June 15th, 1983, and made available by Dr. C. R. Philbrick, will be

presented and analyzed in conjunction with simultaneous Poker Flat MST radar data to demonstrate the control that large-scale internal gravity waves have in determining the location of regions of wave saturation and enhanced turbulence production. The data to be presented show that, in this instance, the turbulence near the mesopause was most likely the result of dynamic instablity a large-scale, rotary gravity wave.

4.1 Background environment

The location of the mesopause is shown distinctly in the temperature profile, obtained by the accelerometer sphere, displayed in Figure 4.1A. Note that the cold mesopause near 85 km is at a temperature of about $130^{o}K$, slightly colder than the average observed summer mesopause temperature at $65^{o}N$ of about $140^{o}k$ shown in Figure 1.1A. The temperature profile can be used to determine a Brunt-Vaisala frequency profile with the formula $N^2 = (g / T) (Tz + g/c_p)$. An N profile is shown in Figure 4.1B, where successive 10 km segments of the data in Figure 4.1A have been used to obtain T and Tz values. Note the sudden increase in N and atmospheric stability near the mesopause at 85 km.

The wind profiles of Figure 4.2 show that the wind was directed toward the southwest with a speed of 40 m/s in the 80 to 90 km region at the 2055 local meridian time of the

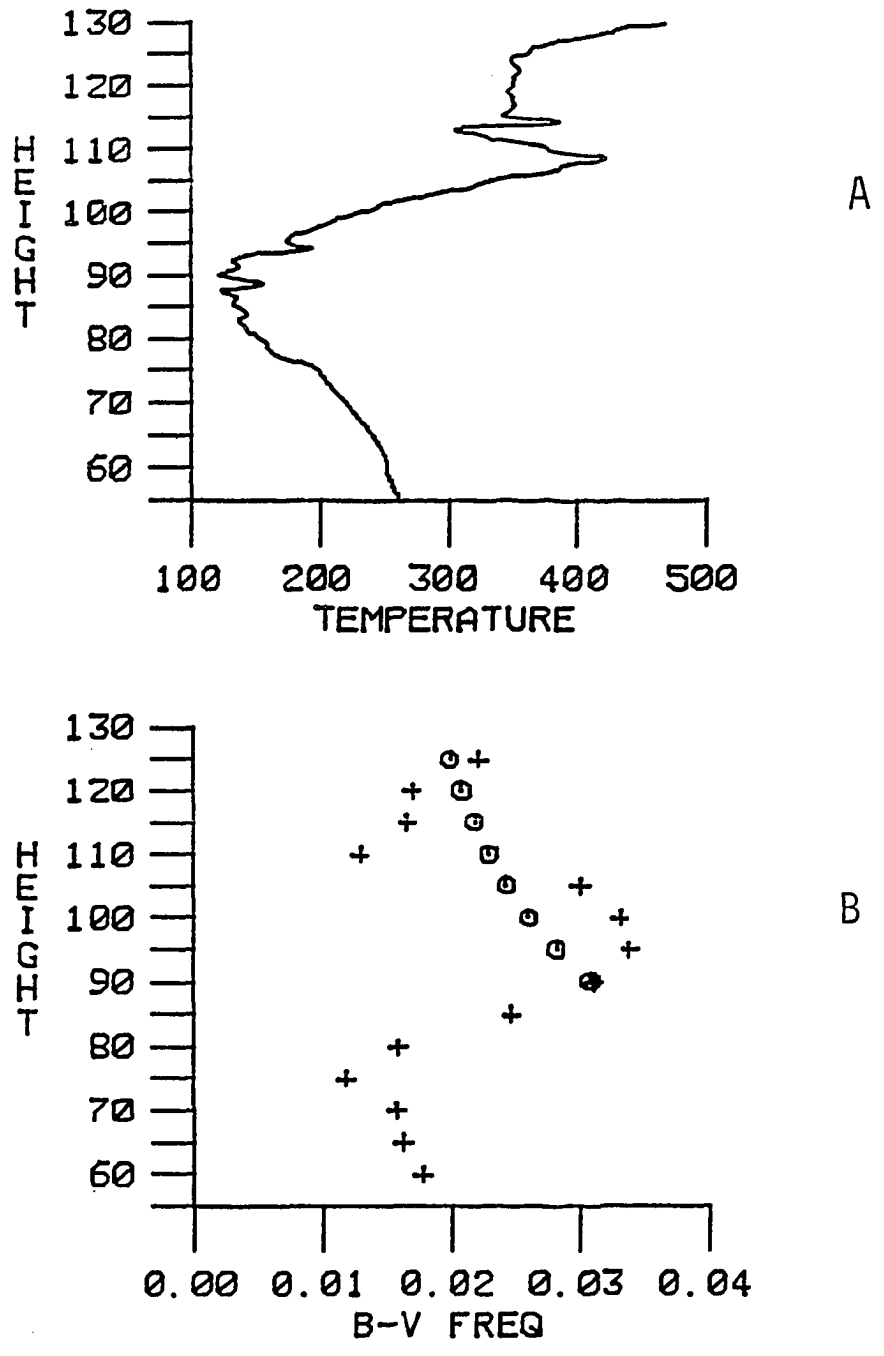

Figure 4.1 A) Temperature profile obtained by accelerometer sphere at 2055 AST, June 15, 1983. B) Brunt-Vaisala frequency profile inferred from part A. Circles are the profile after a 30 km wave was removed from the data.

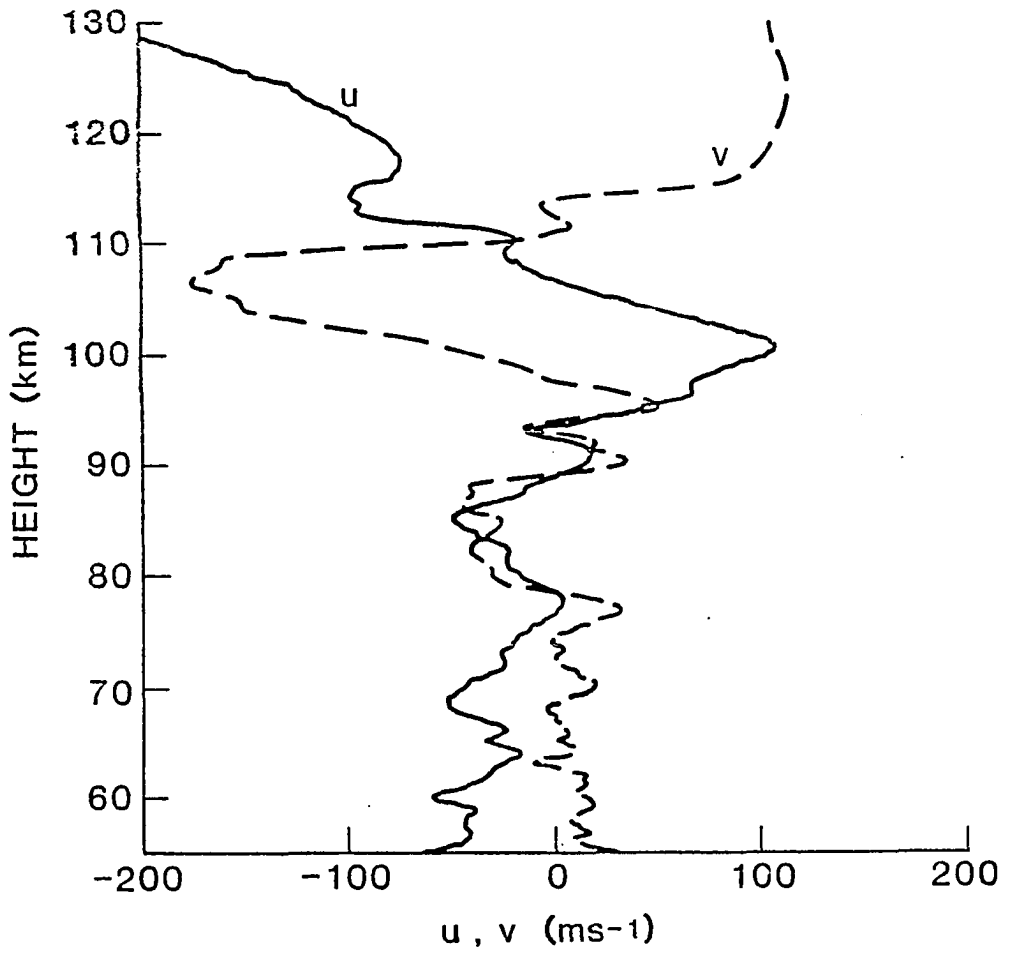

Figure 4.2 Wind profiles from the accelerometer sphere flight at 2055 AST, June 15, 1983. U is the zonal wind and V the meridional wind component.

accelerometer flight. However, overlaying the zonal and meridional profiles demonstrates that the wind was directed towards different azimuths at other heights. This rotation of wind direction with height is one indication of the presence of a large-amplitude rotary or inertio-gravity wave.

The temporal and spatial extent of significant signals received by the Poker Flat MST radar can be inferred from the plot of radar measured horizontal wind vectors shown in Figure 4.3. In this figure, supplied by Dr. Ben Balsley of NOAA's Aeronomy Lab, north is toward the top of the page and the length of an arrow is proportional to the wind speed. The radar was operating with a spatial resolution of 300 m along each beam. The horizontal wind vectors were determined from 15 minute averages of the velocities measured in each oblique beam. The assumptions that the vertical velocity was zero and that the horizontal wind field was homogeneous, at least over scales on the order of the 30 km beam separation, were made in order to compute the horizontal winds.

Only velocities from signals that were clearly above the radar noise level were used in the averages. Thus, Figure 4.3 shows that the S/N was not sufficiently strong to allow continuous sampling of the 80-90 km region. The regions of strong echoes changed altitude with time,

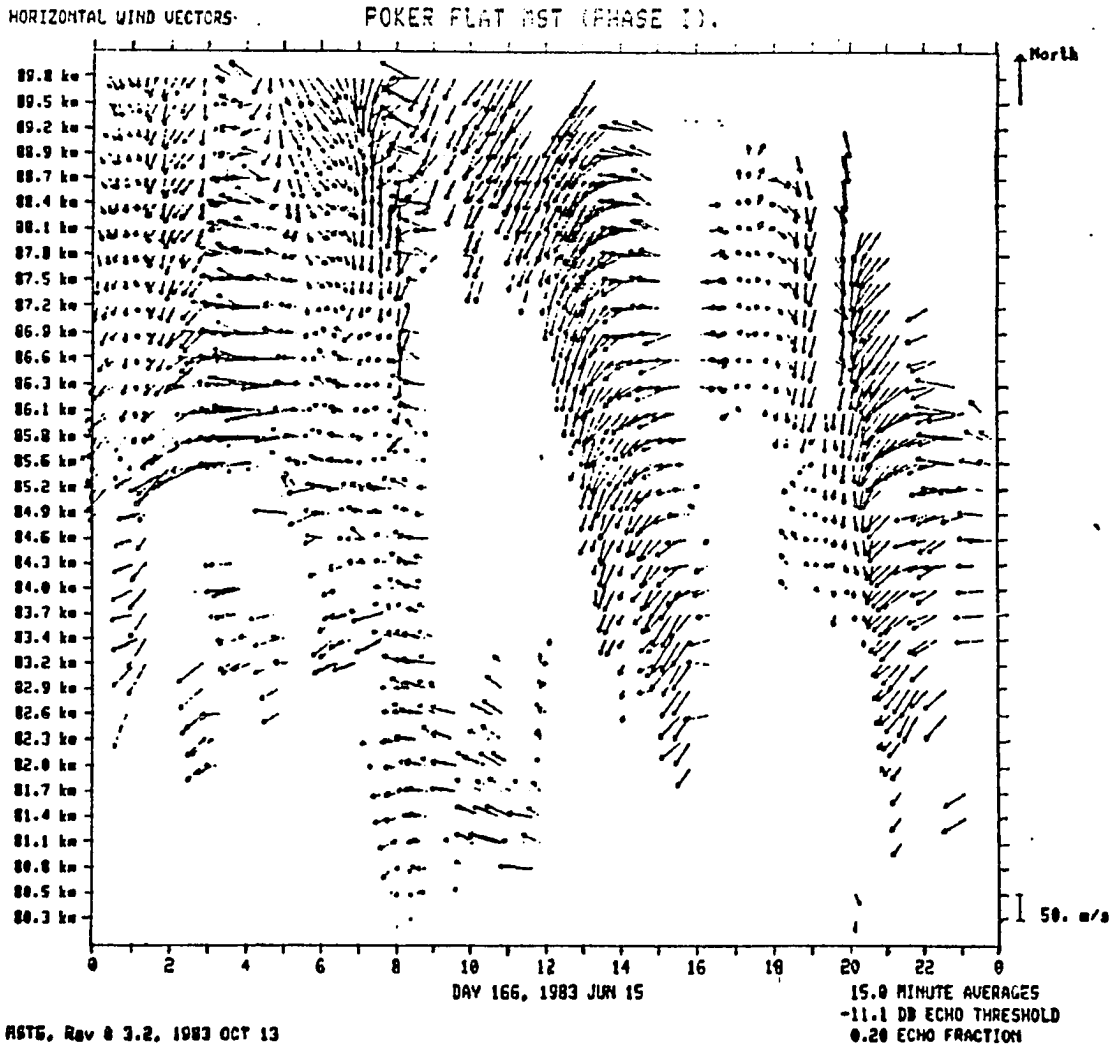

Figure 4.3 Time-height cross section of horizontal winds estimated from Poker Flat MST radar data. Blank regions occur where the return signal was too weak to yield reliable wind estimates.

especially in the latter half of the day. It can be inferred that the location of the strongest turbulence or of the steepest electron density gradient or both were descending with time at 1400 and 2100 AST.

Summarizing the mesospheric environment on June 15, 1983, the winds were generally directed to the south and west, the mesopause was near 85 km, the Brunt-Vaisala frequency (which is a measure of atmospheric stability) was smallest below 85 km and there was a factor of 2 increase in N at the mesopause. As will be shown in the next section, the location of the mesopause and areas of smallest stability were imposed largely by the temperature perturbations associated with the passage of a large-scale gravity wave.

4.2 Wave observations during STATE

The characteristics of several waves were deduced by least squares fitting of sine waves to rocket and radar measurements. The rocket obtained a nearly instantaneous height profile from which vertical wavelengths, amplitudes and heights of maximum amplitude were obtained. Time series at discrete heights were obtained by the Poker Flat MST radar, and sine wave fitting yielded periods, amplitudes and time of maximum at each height. The optimum vertical wavelengths and periods were determined by varying the wavelength or period until the sum of the squared

differences between the data and the fitted curve (the residual variance) reached a minimum. In each case, a large-amplitude wave was apparent in the raw data which allowed good approximations of wavelength and period to be used for the initial points of the curve fitting procedure. 95% confidence limits accompany each of the fitted parameters. These limits were calculated using the approach of Jenkins and Watts (pp. 132 -139, 1968). The 95% confidence limits (i.e., the limits that would contain the actual value of the parameter with 95% probability) may be overestimated since in each step of the calculations the largest limit was assumed.

4.2.1 Large-scale wave in the radar observations

The Poker Flat MST radar was taking data with 300 m range resolution at intervals of 3 minutes routinely during the STATE campaign and was switched to 1 1/2 minute intervals for brief periods about the times of the rocket launches. In order to minimize cross-talk, the radar routinely transmitted on oblique beams for 1 1/2 minutes, then turned off the oblique transmitters and operated only the vertical beam. Thus, consecutive oblique radial velocity estimates came at 3 minute intervals. A sample of the measured velocities is given in Figure 4.4, which contains time series of velocities along the east beam. The erratic lines on the plot are the raw velocity data

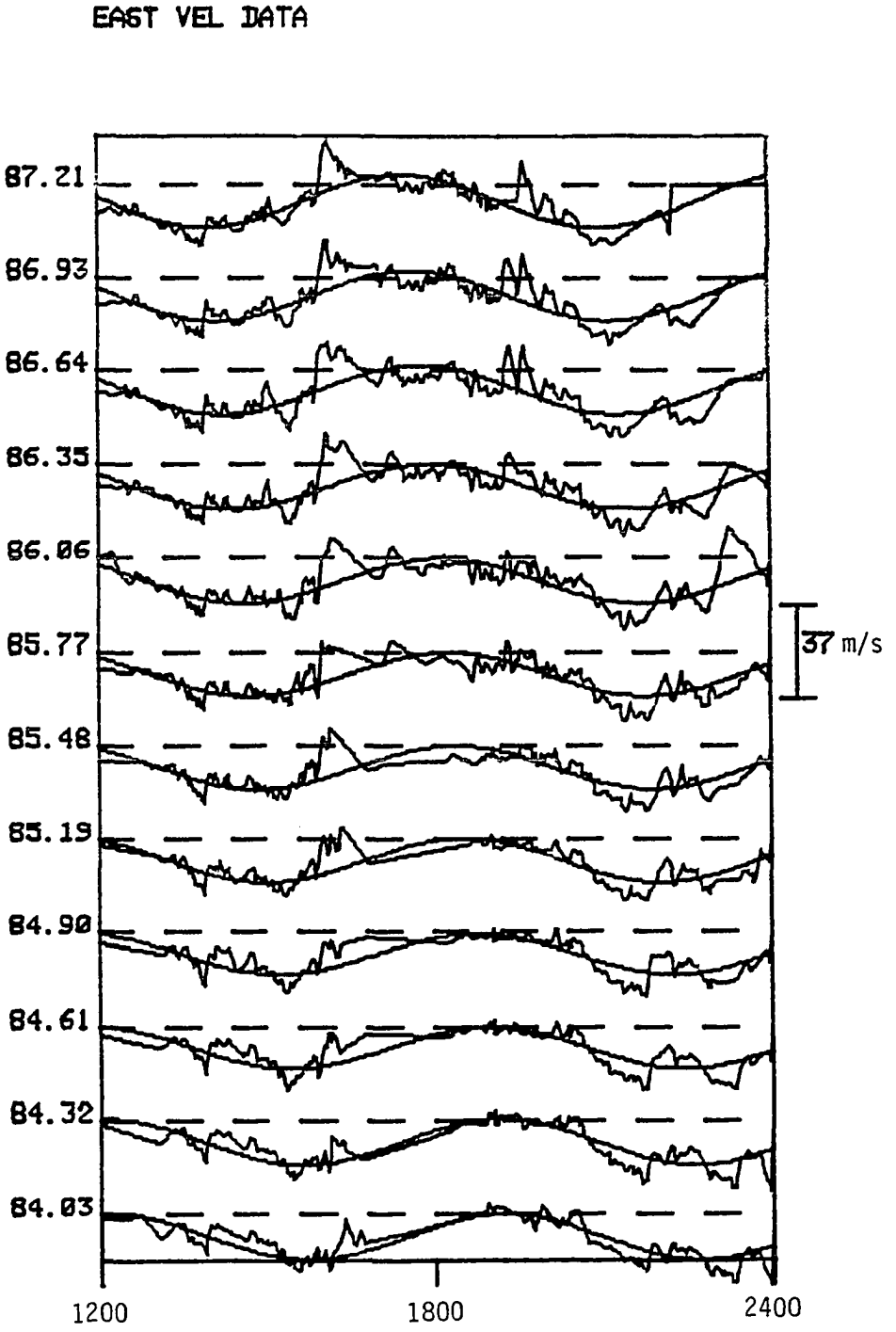

Figure 4.4 Time series of wind speeds measured along the east beam on June 15, 1983. Times are in Alaska Standard Time (local meridian time).

that have been linearly interpolated for ease in plotting. The straight, interpolated line segments connecting the data near the center of the plot at the lowest heights indicate regions where the signals were weak and no velocity measurements could be made.

Figures 4.3 and 4.4 clearly demonstrate that a nearly sinusoidal motion with a period of approximately 7 hrs. dominated the oblique velocity time series. Least squares fitting of sine waves over the data set from 1200 to 2400 and over all heights showed that indeed the best fit period was 7 hrs. Thus, at each height, estimates of the amplitude of the wave and its phase were obtained from fits of functions of the form $A \cos(\omega t + \phi)$, where ω is the best fit wave frequency and ϕ is the estimated phase of the wave. The time of maximum wave amplitude can be found from setting the argument of the cosine function to 0, which yields the time of maximum equal to $- \phi/\omega$. The wave fits have been superimposed on the measured velocities of Figure 4.4 to illustrate the success of this procedure.

The estimates of amplitude and phase for each beam and each height are plotted in Figure 4.5. Note the very smooth progression of phase with height for the two oblique beams and the relatively uniform increase of amplitude with height. The variations of phase with height give estimates of the vertical wavelength, which are 20 and 17.5 km for

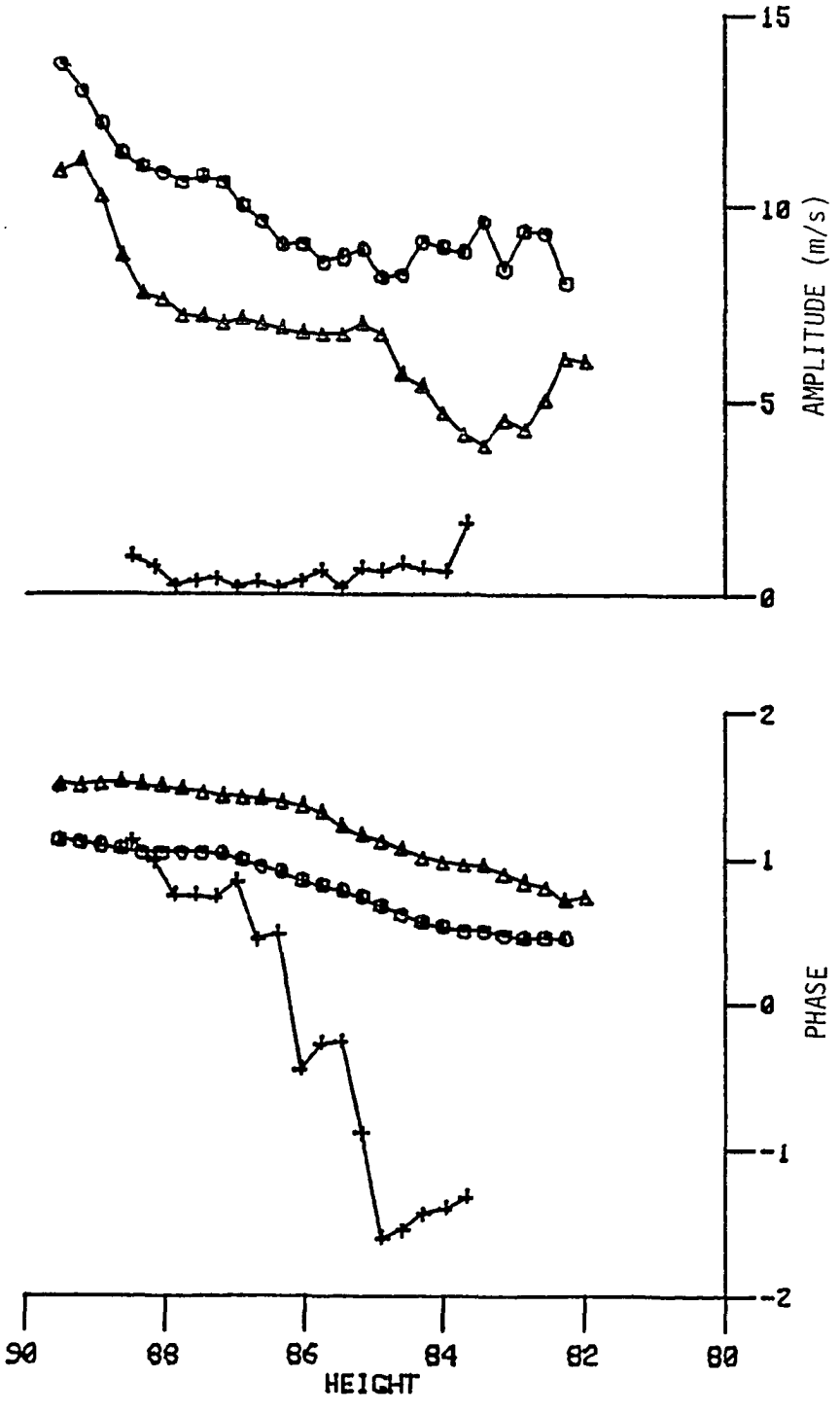

Figure 4.5 Phase (in units of π) and radial amplitude of sine waves fitted to data at each height over the period from 1200 to 2400 AST, June 15, 1983. Assumed period was 7 hr. Circles are for east beam, triangles for north and crosses for vertical.

the east and north beams. These and other wave parameters are given in Table 4.1.

Since the amplitudes are different in the two orthogonal beam directions and there is a phase difference between the two beams, the resultant perturbation velocity vector at any height will trace out an ellipse. This is also evident from its period which is about half of the local inertial period, implying the Coriolis force operates on the wave-induced particle motions, generating a rotary wave. The parameters for the sine wave observed in each of the orthogonal beams can be combined to produce estimates of the maximum amplitude of the ellipse associated with the wave at any height and the azimuthal direction of the maximum wave amplitude and estimates of these parameters are plotted in Figure 4.6.

Figure 4.6 shows that the amplitude of the inertio-gravity wave was fairly constant with height up to 86 km and that the direction of the major axis of the ellipse was along a line running from 50^{o} to 230^{o}E. Since the velocity perturbation is expected to be a maximum in the direction of wave propagation, this wave was inferred to propagate along the direction of the major axis, toward 50^{o} or 230^{o}E. In principal, the phase of the vertical velocity data could be used to determine which of the two directions is the direction of wave propagation because the vertical velocity

Table 4.1
Large-scale wave characteristics on June 15, 1983

	Radar data	Rocket data
Data window	1200-2400 AST 82 - 89 km	2055 AST 85 - 130 km
Period	7 hr	
λ_z	19 km	30 km
u'	38 $\pm$ 5 m/s	82 $\pm$ 9 m/s
T'		59 $\pm$ 5^{o}
T' (using u' and polarization relations)	20^{o}	69^{o}
propagation dir.	230 $\pm$ 10^{o}	186 or 295 $\pm$ 55^{o}
assumed N	0.03 rad/s	0.023 rad/s
U-c	121 m/s	110 m/s
c	151 m/s	
u' / U-c	0.26	0.75
T_z / (T_z + g/c_p)		0.73
u' / v'	1.48	1.98
intrinsic period		
using U-c	8.74 hr	
using u'/v'	9 hr	6.67 hr

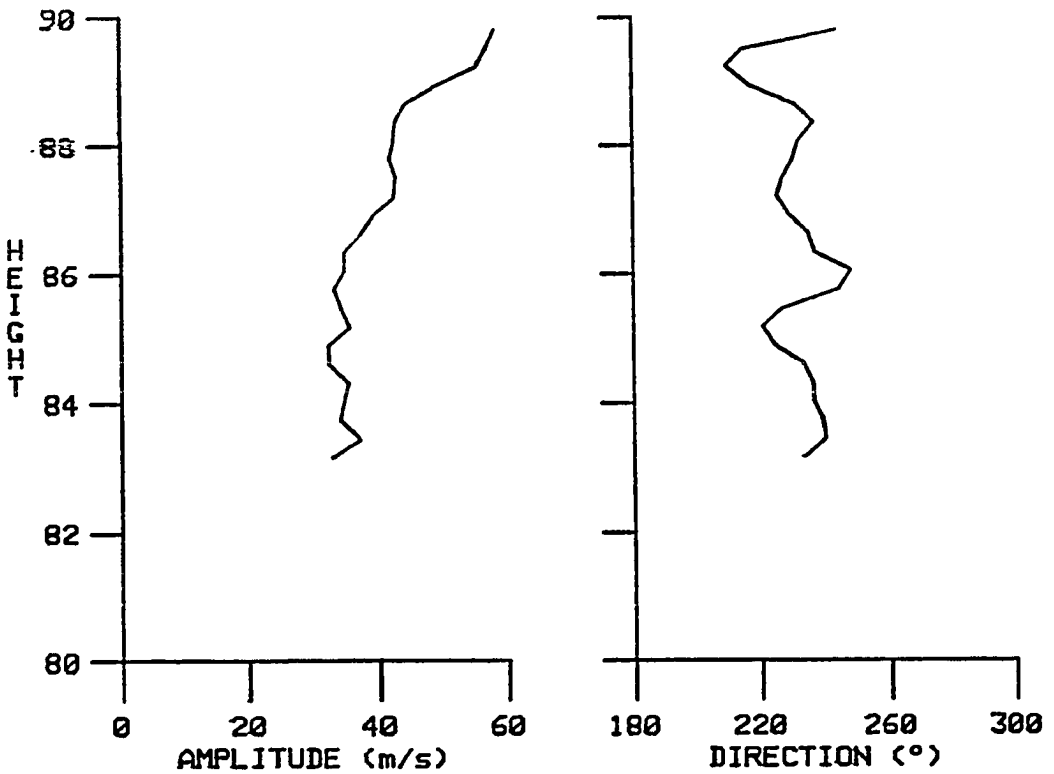

Figure 4.6 Estimated horizontal amplitude (u') and propagation direction of the 7 hr wave as a function of height.

is at a maximum when the horizontal perturbation vector is maximum in the direction of wave propagation. However, the vertical phase data of Figure 4.5 are much more variable than the oblique data and produce equally variable estimates of propagation direction. The erratic behavior of the implied phase is due either to the very small vertical velocity associated with this wave, being buried in the noise of the other motions present or by the poor velocity resolution used during the campaign and the attendant DC filter problems (see section 3.2.1). Fortunately, accurate vertical wave velocity estimates were not needed in this analysis because temperature data from the rocket flight and the S/N data from the radar were used to establish the wave propagation direction to be towards the southwest at approximately 230^{o}E.

The direction of energy propagation can be determined from consideration of the rotation of the perturbation velocity vector with height and an estimate of U in the direction of wave propagation. Figure 4.3 shows that the perturbation vector rotates clockwise with time (at a fixed height) and clockwise with height (at a fixed time). This is the sense of rotation corresponding to an upward propagating wave with a horizontal phase speed greater than the mean wind speed ($c > U$) or to a downward propagating wave with $c < U$ in the norther hemisphere. Note that

positive velocities are defined to be in the direction of horizontal wave propagation, i.e., c > 0. If U > c then it must be that U-c < U. U-c can be crudely estimated from eqn 2.18 and knowledge of N and m. With N = .03rad/s and a vertical wavelength of 19 km, U-c is approximately 90 m/s. The mean wind in the direction of wave propagation is 30 m/s to the southwest. Clearly, U-c cannot be less than U and therefore, c is greater than U and energy propagation is upward.

Values of the intrinsic or Doppler shifted frequency can also be obtained with the above parameters in two independent ways. The first method uses the value of U-c obtained from the vertical wavelength.

Algebraic manipulation of the expression for the real part of m (eqn. 2.16) yields the relation

$$|U-c| = \left(\frac{f^2}{k^2} + \frac{N^2}{m^2}\right)^{1/2} \qquad (4.1)$$

The observed frequency is much smaller than N, so it was assumed that $N^2 - \beta^2 \simeq N^2$ to get the above expression. An estimate of k is needed before U-c can be accurately computed. Since $c = \omega/k$, an estimate of c is equivalent to an estimate of k. c is obtained from $|U-c| + U$, where the choice to add rather than subtract U is made because c > U. Thus, U-c is obtained from an estimate of k, which is in turn determined from U-c . The final value of U-c is

computed using an iterative scheme. First, U-c is calculated assuming k is infinite. This value of U-c gives an estimate of c and k. This new k is then used to compute the next value of U-c, etc. until U-c and k attain constant values. This scheme gives estimates of U-c and c as 121 m/s and 151 m/s. Then the intrinsic period (equal to $2\pi/k(U-c)$) is 8.74 hrs.

The other method is to note that the ratio of u' to v' is equal to $k|U-c|/f$ (eqn 2.22). Then from a determination of the ratio of the magnitude of the major axis of the velocity ellipse to the minor axis, which for this wave was 1.48, it is found that $k|U-c|$ was 13.2 hrs / 1.48 or 9 hrs. very close to the intrinsic period obtained from the first method.

The saturation condition can be investigated using the derived value of U-c and the wave amplitude. The ratio, u' / U-c = 40 / 151 = .26, is less than the monochromatic wave saturation threshold. Since this is an inertio-gravity wave it is more appropriate to consider not just the convective instability threshold but also the influence of the transverse shear at the point of maximum wave amplitude. From the formulation of Fritts and Rastogi (1985) reproduced in eqn 2.31, a value of u' / U-c = .84 is obtained for a 9 hr period wave and again the observed amplitude is less than the saturation threshold.

An estimate of the intrinsic period can be used to estimate the horizontal wavelength since the ratzof the vertical to horizontal wavenumber is equal to the ratio of the Brunt-Vaisala to intrinsic frequency. The horizontal wavelength, estimated in this manner, is approximately 2600 km.

Thus, the observed values of vertical wavelength, period and wave amplitude give a picture of a wave with an intrinsic period of 9 hrs. having an amplitude that is less than the instability threshold amplitude by about 1/3.

4.2.2 Large-scale wave in rocket observations

The Nike-Hydac rocket carrying the accelerometer instrumented sphere was launched at 2051 AST on June 15th and required approximately 5 minutes to complete both the upleg and downleg trajectories through the 130 to 55 km altitude. The velocity and temperature structures inferred from the accelerometer data are shown in Figures 4.1 and 4.2.

To separate the small scale perturbations from the large scale mean profiles, the temperature and velocity data were differenced between adjacent sample points, which were placed at 250 m intervals. The differenced data are shown in Figure 4.7. The differenced data below 75 km are not shown because the density fluctuations could not be separated from the wind fluctuations due to the lack of

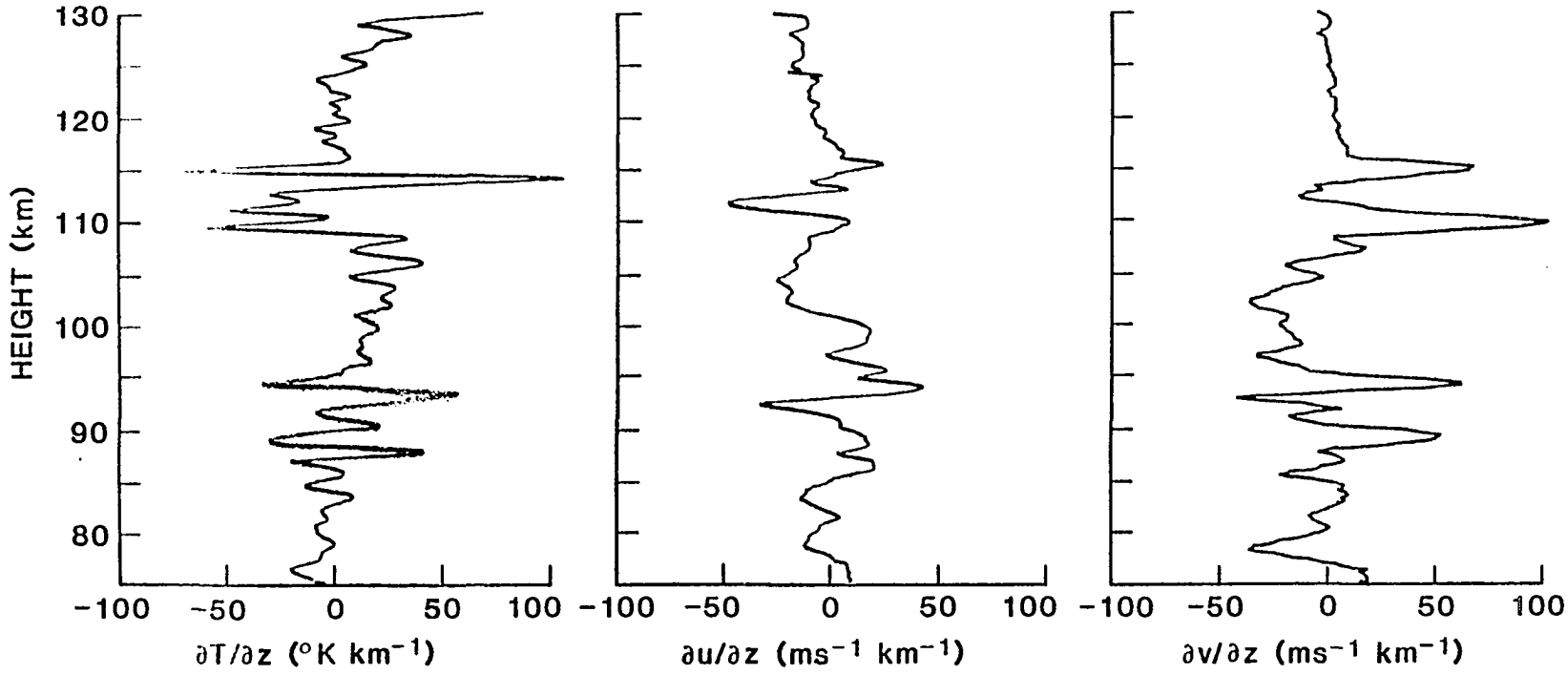

Figure 4.7 Differenced data of the profiles in Figures 4.1 and 4.2.

upleg data below that height as described in section 3.1.2. Note the large variance over small height regions at heights of 90 and 112 km in all three plots. Also note the long wavelength sinusoidal variation present, especially in the temperature plot. Differencing acts as a high-pass filter so the presence of the long wave component after differencing indicates that its actual amplitude in the raw data is quite large.

Having identified the long wave-like perturbation in these plots it was possible to perform least squares fitting to the raw data profiles. In order to avoid the bias that would be introduced by the large scale mean temperature profile (especially the sharp minimum at the mesopause) the fitting was done only to the data from 85 to 130 km. Because N and U-c vary slowly over this region, a wave of constant amplitude, over the entire 45 km, was fit to the data. Before performing the sine wave fitting the linear trend was removed from each data series. This effectively left variations about the mean shear. The time mean profile could not be removed since only one profile was available.

Varying the vertical wavelength of the sine wave fit revealed the best fit wavelength to be 30 km in the temperature data and 27 km in the meridional velocity data. However, the residual variance of the fits to the zonal

velocity data indicated that the best fit wavelength was greater than 40 km. This inability to clearly identify a wavelength near 30 km in the zonal data is very possibly due to the large scale mean flow that was not removed from the zonal wind profile. Assuming that identification of the wave in two of the three profiles indicated the wave was present, parameters were obtained for a 30 km wave fit to all three profiles. These parameters are presented in Table 4.1.

The zonal and meridional amplitudes and phases of the wave fits can be combined as before to determine the maximum amplitude and the direction of the major axis of the velocity perturbation ellipse. The maximum amplitude is 81 m/s and the direction was 6^{o} or 186^{o}. To decide if the wave was heading to the south or north, use was made of the phase of the temperature perturbation. Recall that the maximum of the wave induced temperature perturbation occurs a quarter wavelength below the velocity maximum in the direction of wave propagation. Since the maximum temperature perturbation occurs at an altitude of 78 km, the wave is inferred to be propagating in the direction of the velocity perturbation vector at an altitude of 85 km or towards 295^{o}. The uncertainty in the propagation direction from the rocket data may again be attributed to the lack of

a good mean profile to remove from the data before determining the wave parameters.

The consistency of the wave interpretation of the observed fluctuations can be checked using the polarization relations (eqn 2.25). Specifically, T' can be computed from values of N, $\overline{T}$ and u' yielding T' = 69^{o} while the observed temperature perturbation amplitude is 59^{o}.

With information on the temperature as well as the velocity perturbation of the wave, it is possible to check on the proximity of the wave amplitude to the instability threshold by two independent means. One is to examine the wave induced temperature lapse rate in relation to the mean lapse rate. For an instability to occur the perturbation lapse rate must be of sufficient magnitude to drive the atmosphere into a superadiabatic state. Such a condition occurs when $T_z / (\overline{T}_z + g / c_p) = 1.0$. For the 30 km wave this ratio was 0.78. The mean lapse rate was obtained from the trend which was removed from the data before the wave fitting procedure. The result of removing the wave from the raw data is shown in Figure 4.8, where it can be seen that a nearly linear increase of temperature with height remains after the wave is removed.

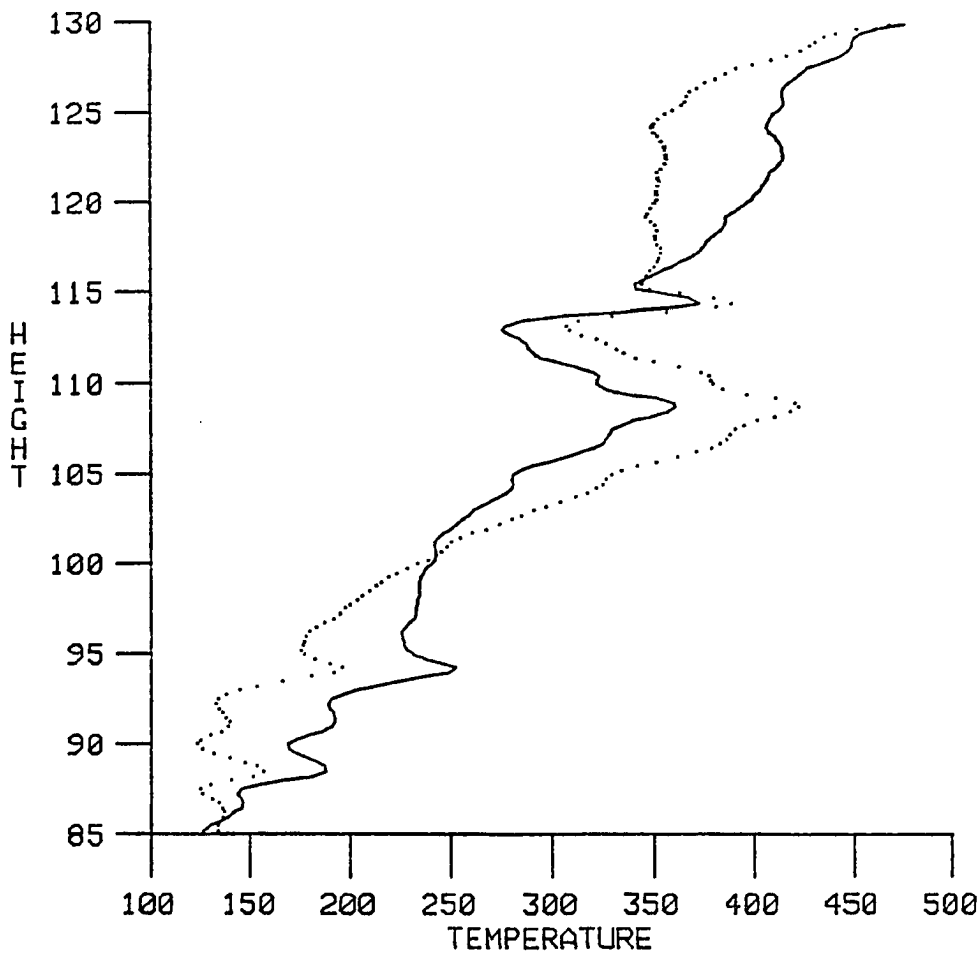

Figure 4.8 Original temperature profile (dots) and the temperature profile after the 30 km wave was removed (solid). Note the steady 6°K/km increase of temperature with height of the solid line.

The maximum amplitude can be used to examine the instability criterion as before using the vertical wavelength to obtain a value of U-c. The ratio of perturbation velocity to intrinsic phase speed is u' / (U-c) = 82 / 110 = .75. Again, this wave has an amplitude that is less than the linear saturation amplitude, but closer to the reduced amplitude computed for an intrinsic period of 9 hrs. The ratio of the amplitude of the major axis to that of the minor axis of the ellipse is 1.98, very similiar to that found using the radar data.

4.2.3 Consolidation of radar and rocket wave data

The Poker Flat radar data indicate the presence of a 7 hr period wave of large amplitude between the heights of 82 to 88 km during the latter half of June 15, 1983. The accelerometer sphere data revealed the presence of a 30 km vertical wavelength wave of large amplitude in the 85 to 130 km height region at about 2055 AST. We will here demonstrate that both data sets measured the characteristics of the same wave.

First, we will address the apparent differences between the observations. The vertical wavelength in the rocket data was 27-30 km yet in the radar data it was determined to be 19 km. However, vertical wavelength is proportional to U-c and inversely proportional to N. An upward propagating wave would be vertically compressed as it

entered regions of larger N immediately above the mesopause and would experience an increase in vertical wavelength as it propagated through the region of decreasing N above the mesopause. Thus, much of the difference in vertical wavelength estimates could be accounted for by the decrease of N with height above 85 km shown in Figure 4.1B. Also note that the vertical wavelength from the rocket data may be overestimated due to the presence of the deep temperature minimum at the mesopause even though we tried to avoid the influence of the mesopause by only using the data above 85 km.

Wave amplitude is greater in the rocket data by more than a factor of two over the radar data. This growth of the wave with height is to be expected. The radar data are centered at 85 km and reliable coverage extends 3 km above and below. The rocket data were fit from 85 to 130 km so the parameters are r.m.s. estimates made over a height range centered at 110 km. Between 85 and 110 km there are about 3 or 4 scale heights. Since unsaturated wave amplitudes grow in proportion to $e^{z/2H}$, growth by a factor of 5 would occur from 85 to 110 km in the absence of dissipation or reflection. Such an increase in amplitude would have brought the wave amplitude much above the saturation amplitude. Above that altitude at which the wave became saturated, the wave amplitude would be limited

to the saturation amplitude. The amplitudes estimated from the rocket data do indicate the wave was saturated. Thus, it can be seen that the differences in wavelength and amplitude can be explained by propagation through an environment with varying density and N.

The two data sets also yield several wave parameters that are in agreement. Both data sets reveal similiar directions of propagation as well as the same direction of rotation with height and therefore the same direction of energy propagation. The location of the most negative temperature gradient in the rocket data very nearly coincides with the location of the maximum wave amplitude in the radar data as would be expected for a linear, monchromatic gravity wave. This point is illustrated in Figure 4.9. The series of crosses are locations of the maximum velocity amplitude of the wave inferred from the least squares fits. The dot at 85.4 km near 2055 locates the largest negative temperature gradient determined from the rocket data. As can be seen both sets of observations place the most negative perturbation temperature gradient of the large-scale wave in close proximity to the most intense echoing regions implying a direct connection between the dissipation of wave energy and the presence of 3 m turbulent irregularities in the radio refractive index.

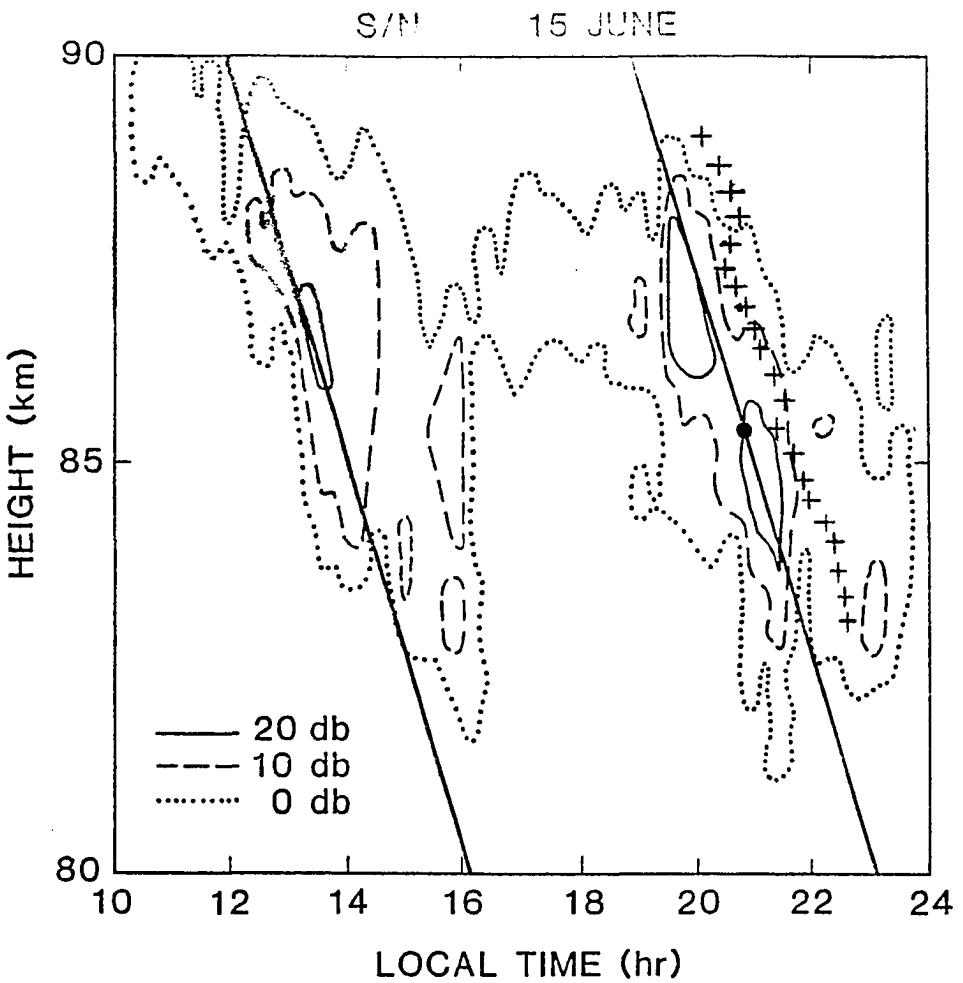

Figure 4.9 Contours of S/N averaged over both oblique beams. Crosses are locations of the maximum amplitude of the 7 hr rotary-gravity wave. Dot at 85 km is location of most unstable lapse rate in temperature perturbation observed in rocket data . Slanted line illustrates the motion of the most unstable lapse rate with the phase speed of the 7 hr wave.

4.2.4 Observations of other waves

The extended height coverage of the rocket data allowed the vertical wavelength, amplitudes and directions of propagation to be determined for two other smaller scale waves as well. Unfortunately, only the largest amplitude, 7 hr wave could be isolated in the radar data so no frequency information is available for these other waves.

Between the heights of 75 and 95 km, a 12 km vertical wavelength wave is apparent on the rocket wind profile of Figure 4.2. The zonal and meridional components of that wave appear to be equal and in phase, implying that this wave is a plane wave propagating at a 45^{o} angle to the coordinate axes. The parameters of this wave, given in Table 4.2, reveal that it is below the saturation limit for monochromatic waves. Since it is a plane wave there is no need to consider the reduced limit needed for rotary waves.

The other wave of interest was found by computing coherence spectra between the wind components and the temperature profile at 10 km intervals. In the 85 to 95 km region, the coherences between all pairs of profiles were significant for a 2.5 km vertical wavelength wave. The parameters for this wave from least square sine wave fitting are also given in Table 4.2. The large uncertainties associated with this wave are due to the small amplitude of the wave compared to the other perturbations present in the data and to the short length

Table 4.2
Small-scale waves in rocket data of June 15, 1983

Data window	75 - 95 km	85 - 95 km
λ_z	12 km	2.5 km
u'	20 $\pm$ 8 m/s	9.5 $\pm$ 10 m/s
T'	7.6 $\pm$ 6^o	8.9 $\pm$ 7.5^o
T' (using u' and polarization relation)	6.2^o	4.7^o
propagation dir	40 $\pm$ 45^o	11 $\pm$ 26^o
assumed N	0.02 rad/s	0.03 rad/s
U-c	38 m/s	12 m/s
u' / U-c	0.54	0.80
T_z / (T_z + g/c_p)	0.63	1.6
u' / v'	5.7	2.4

of the data segment over which it is visible. However, the wave appears to be above the saturation limit and seems to be propagating downwards. Since this wave is propagating downward against the density gradient, it was probably locally generated.

Radar data from June 17th, 1983 also revealed a rotary wave propagating through the 80-90 km region and again modulating the echo-producing areas. The horizontal winds computed as for Figure 4.3 by the Aeronomy Lab are shown in Figure 4.10. Note the two regions of enhanced S/N extending down below the lower heights at 6 and 830 AST. The best fit period was found to be 190 minutes or 3.17 hr using the data from 0400 to 1000 AST. The amplitudes and phases of the fitted 190 minute wave are shown in Figure 4.11 and the amplitude and direction of propagation of the corresponding rotary gravity wave are presented in Figure 4.12. The deduced wavelengths and saturation percentages are given in Table 4.3.

Again, it can be seen that the radar echoes are strongest (at least at the lowest heights) where the perturbation velocity is at a maximum in the direction of wave propagation (205^{o}E). As for the 7 hr wave, the wave amplitude is about half the saturation amplitude but this wave is clearly influencing the echo-producing regions at that phase where the wave-induced temperature perturbation

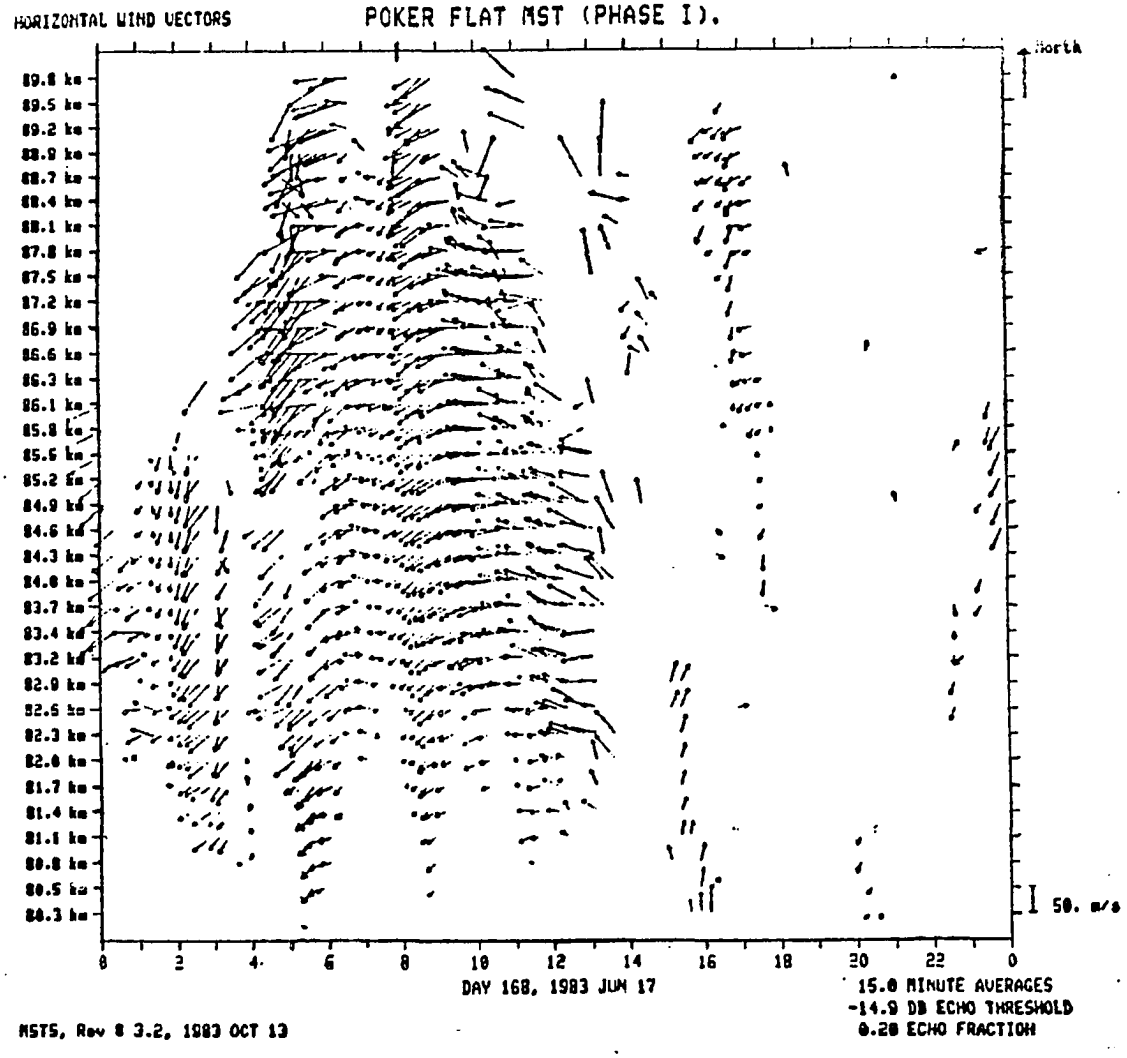

Figure 4.10 Similar to Figure 4.3, but for June 17, 1983.

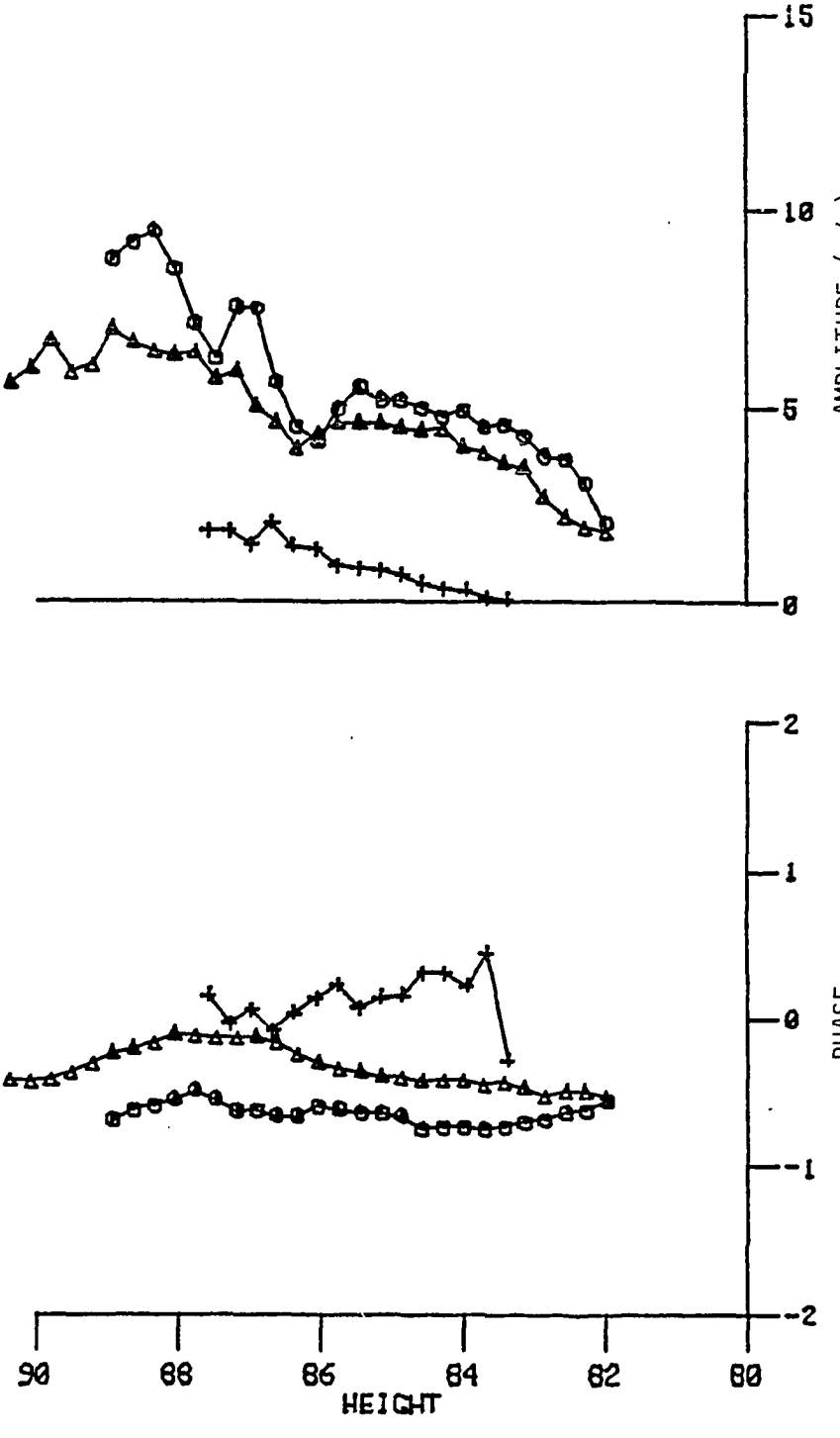

Figure 4.11 Phase (in units of π) and radial amplitude (in m/s) of the sine wave fits to the data at each height in the east (circles), north (triangles) and vertical (crosses) beams. The fits were made to the data from 0400 to 1000 AST, June 17, 1983.

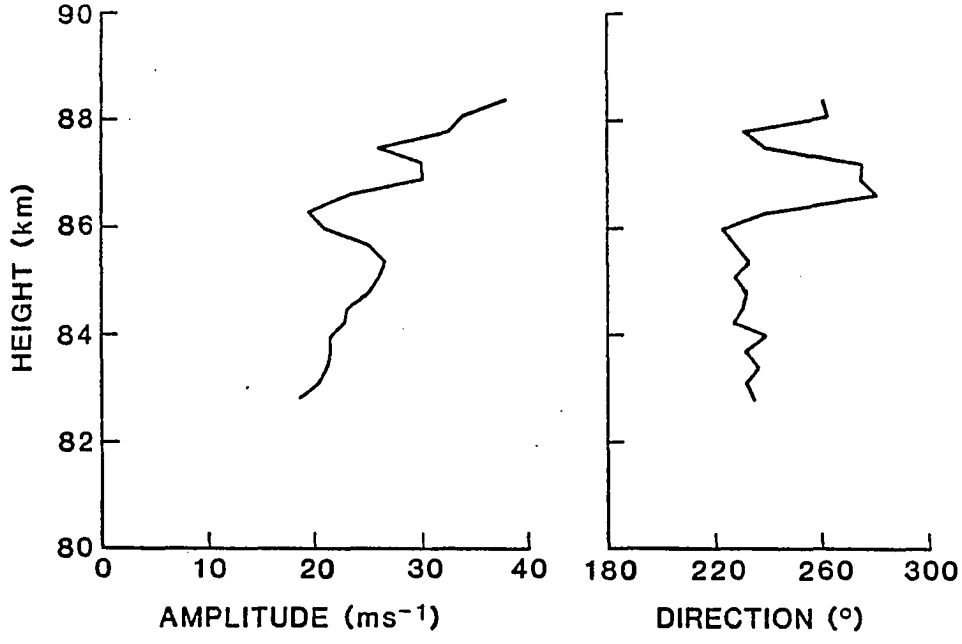

Figure 4.12 Horizontal amplitude (u') and direction of propagation for the 190 wave on June 17, 1983.

Table 4.3
Large-scale wave characteristics in radar data
on June 17, 1983

Data window	0400 - 1000 AST 84 - 88 km
Period	3.17 hr
λ_z	21, 42 km
u'	25 $\pm$ 4.5 m/s
propagation dir.	205 $\pm$ 20^o
assumed N	0.025 rad/s
U-c	83, 166 m/s
u' / U-c	0.3, 0.15
u' / v'	1.79
c	128, 211 m/s
intrinsic period	
using U-c	4.9, 4.1 hr
using u' / v'	5.7 hr

is most negative rendering the environment most nearly unstable.

4.3 Wave effects near the summer mesopause

Large-amplitude, large-scale, low-frequency gravity waves clearly have an effect on the regions of 3 m scale size turbulence near the summer mesopause. Balsley et al. (1983) presented several years of Poker Flat radar data, frequency spectra covering periods of several days and model calculations to show that the strong radar echo obtained near the summer mesopause was a result of the vertical compression of tidal and gravity wave motions as they approached the mesopause and larger background values of N. The vertical compression increases the wave amplitude relative to that needed for instability by decreasing the vertical wavelength, which would lower the Richardson number and, if the amplitudes and compression were large enough, would result in the appearance of shear generated turbulence. The waves analysed in this chapter are not tides because they are propagating mainly to the south while tides follow the sun. Also, the periods of the waves do not correspond to tidal periods.

It has been shown that the regions of greatest signal strength (most intense 3 m turbulence) and the regions of large variance in the rocket data are associated with a minimum in vertical shear of the wave velocity and the most

negative temperature gradient in the wave-induced temperature perturbation. The strong signal regions that descend with time (Figures 4.3 and 4.8) appear only once per wave period, in that phase of the wave in which the local Richardson number is the smallest. Thus, the 3 m turbulence occurs where the wave is most nearly dynamically unstable, though the wave amplitude is below the instability threshold.

The data imply that the 7 hr wave was not of sufficient amplitude to be unstable at 85 km. At 112 km, the wave was more likely unstable and appeared to reach the saturation threshold, but it would be unlikely that the Poker Flat radar would receive signals from this region because the necessary 3 m scale-size irregularities are viscously damped at those altitudes. Even though the 7 hr wave did not exceed the saturation threshold at 85 km, wave energy was being dissipated since the wave amplitude was constant from 82 to 86 km. Also, energy was being supplied to small-scale (3 m) turbulence as evidenced by the strong radar echoes in Figure 4.8. Thus, the dissipation of this wave can not be attributed to monochromatic wave saturation and it seems likely that a superposition of waves is necessary to explain the observed wave saturation. Amplitudes were derived for monochromatic waves in an environment assumed free from other perturbations. The

fact that several waves could be identified on June 15 suggests that the superposition of waves was an important factor in the saturation of the long wave. It could also be the case that the small-scale wave activity at 90 and 112 km is a result of harmonic generation of waves by the large-scale, large-amplitude wave, as has been shown to occur by Fritts (1985).

Smaller-scale, higher-frequency waves would see the temperature and velocity perturbations of the 7 hr wave as the background environment. The nearly isothermal lapse rate induced by the 7 hr wave and the transverse shear of the wave lowered the local Richardson number to less than 10 where the perturbation velocity was largest in the direction of wave propagation. In this environment, smaller-scale waves could contribute to dynamical or convective instability more readily than if the 7 hr wave had not been present. The turbulence produced by small-scale wave breaking would remove energy from the 7 hr wave. Thus, the saturation threshold should be reduced in accounting for the saturation of a broad spectrum of waves.

The STATE campaign has demonstrated the utility of simultaneous rocket and radar experiments since the description of the wave dynamics presented here is much more complete than would have been possible with either

instrument alone. The rocket provided vertical structure and temperature data while the radar provided a time history of the waves. The data have shown that large scale waves modulate the mesopause turbulence field. The electron density probes showed that the largest gradients in electron density were at 84 km on June 15th and at 85 and 88 km on two other days. This variation of height could be due to gravity wave transport of atmospheric constituents though the exact relation between wave dynamics and electron density is not clear. Thus, the regions of intense radar echoes are determined by the turbulent mixing of the electron density gradient resulting from gravity wave saturation as concluded by Balsley et al. (1983). Wave saturation appears to be enhanced in this region due to the decrease of the vertical wavelengths of long waves propagating into the strongly stable region at and above the very cold, high-latitude summer mesopause. These data also suggest that saturation of the gravity wave spectrum is due to a superposition of waves.

Chapter 5

Mesospheric gravity waves observed during the winter

The seasonal variation of heights and intensities of mesospheric echoes received by the Poker Flat radar has been mentioned in the previous chapter. Winter echoes are obtained at lower altitudes (60 - 80 km compared to 83 - 89 km), are weaker by about 23 dB (a factor of 200) and cover a a much broader height range than the summer echoes. These differences and possible causes were examined by Balsley et al. (1984). They concluded that the winter echoes were due to upward propagating gravity waves achieving saturation amplitudes below 60 km and continuing to saturate up to at least 80 km. The satruated waves were said to be generating turbulence. The radar was assumed to be sensitive to the turbulence above 60 km because electron densities were large enough there to effectively paint the turbulence. The lack of radar echoes above 80 km was attributed to the increase of kinematic viscosity with height to the point where 3 m scale size turbulence is stongly damped above 80 km. (Kinematic viscosity is proportional to temperature. 3 m turbulence does occur at 86 km in summer because the temperature is lower.)

To illustrate the gravity wave interpretation the results of an analysis presented by Fritts et al. (1984) will be used. Fritts et al. identified a 10 hr period

inertio-gravity wave in the velocity data obtained by the Poker Flat radar on October 11, 1981. The results from that analysis will be supplemented in this chapter with data from the following two days, which suggest an increase of wave frequency with time. Analysis of several other higher frequency, small-scale waves will also be presented. The interaction of these waves with the mean flow will be examined. Most of the wave motions had amplitudes less than halfthe saturation limit but were clearly undergoing dissipation. The waves were found to propagate mainly north- south and therefore could not contribute to zonal wind deceleration.

5.1 Winter mesosphere and echo characteristics

Temperatures in the winter mesosphere at the latitude of Poker Flat are generally warmer than summer temperatures, and the temperature gradient below the mesopause is smaller. The mesopause is less distinct than the deep temperature minimum observed in summer. In fact, there is a broad temperature minimum from about 60 to 90 km as can be seen in Figure 1.1A.

The Poker Flat radar receives echoes in the 60 to 80 km region from about the middle of September to some time in May. These echoes appear daily during the period when the mesosphere is sunlit. It has also been observed that the strength of the echoes is directly correlated with cosmic

noise absorption measured by riometers (Ecklund and Balsley, 1981). The riometers indicate the presence of energetic particle precipitation. Dr. Richard Goldberg (private communication, 1985) suggests that during periods of energetic particle precipitation, positive ions are formed at mesospheric heights. Then, when the weak winter sunlight reaches the mesosphere, photodetachment of electrons produces the increases in electron density and density gradient necessary for the Poker Flat MST to obtain echoes. Thus, the ability of the radar to monitor mesospheric winds is restricted to daylight hours and times of riometer absorption.

A sample of the winds measured on Oct. 11, 1981 at a height of 66.8 km is shown in Figure 5.1. The early morning onset and evening disappearance of the echoes is readily apparent in the vertical time series, since the vertical beam was about 10 dB less sensitive than the east and north beams. During the study period examined here the radar was in its routine operation mode with a time resolution of 1 minute and spatial resolution of 2.2 km.

5.2 Wave observations

The period of October 9 - 13, 1981 was chosen for analysis because it had been previously shown (Balsley et al., 1984, Fritts et al., 1984) that the data for October 11th could be interpreted as clearly revealing the

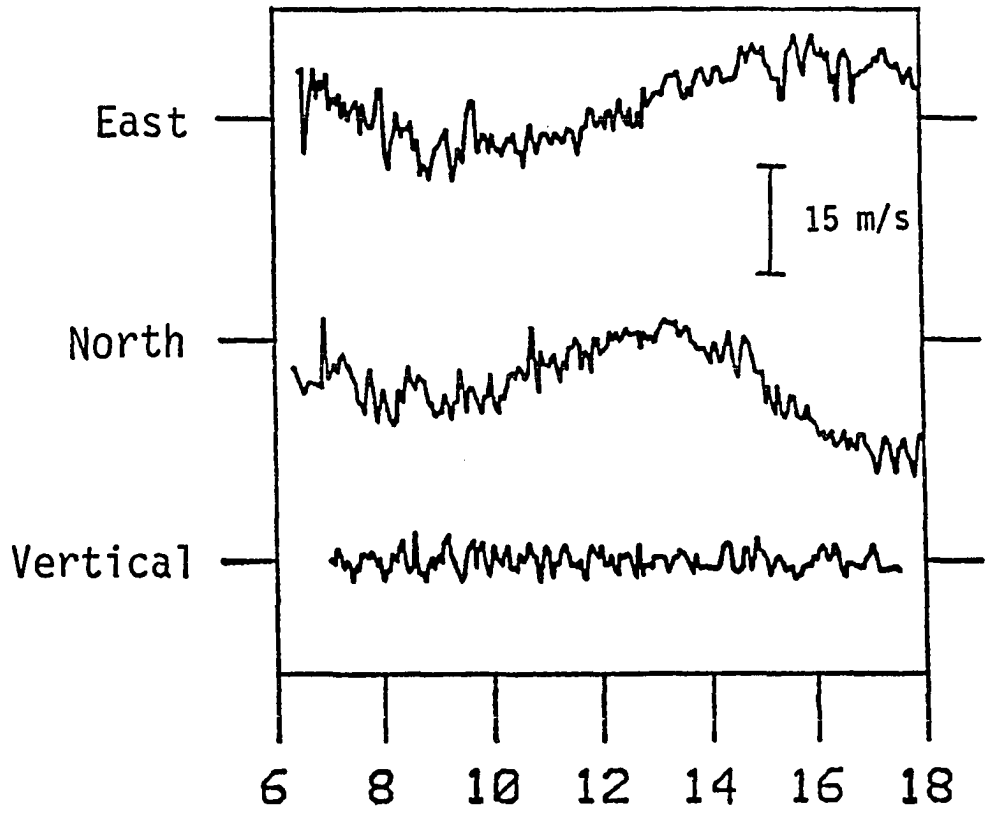

Figure 5.1 Radial velocities measured at 66.8 km on Oct 11, 1981. Positive velocities (above the horizontal zero lines on either side of the graph) are to the east (64°E), to the north (334°E) and upward. Local time in hours is given along the horizontal axis.

saturation of a large-amplitude, low-frequency inertio-gravity wave. The observed wave was vertically transporting southward momentum and so could not account for the zonal deceleration that is theoretically expected to operate above the peak of the 'polar night jet', a region of strong eastward winds in the 50 - 60 km region (see Figure 1.1B).

Waves were identified in the winter data in much the same way as they were identified in the summer data described in Chapter 4. That is, the period of an apparent sinusoidal motion was determined and then sine waves were fit to the data from all three beams and all available heights. The period was varied until the squared residual error was at a minimum and the amplitudes and phases of the sine waves were measured from the least squares fitting procedure. The analysis varied somewhat after the amplitudes and phases were found depending on the frequency of the fitted wave.

Low-frequency, inertio-gravity waves were analyzed with the same methods used in the previous chapter with one important difference. The vertical velocities were measured with a resolution of .13 m/s per Doppler spectral point. This resolution was nearly adequate to permit the determination of the small vertical components of the low frequency waves. Instead of using temperature data (which

was not available) to determine the direction of wave propagation, we used the fact that the vertical velocity maximum occurs at the same time as the maximum horizontal velocity perturbation in the direction of wave propagation.

To identify a high-frequency wave on top of large amplitude, low frequency waves it was necessary to apply band- pass filters to the data with results as shown in Figure 5.2. The packet nature of the waves is obvious from the amplitude variation in this figure. An indication of the small spatial scale of the waves is given by the fact that the three beams, which are separated by 17 km at a height of 67 km, do not always show the same motions. Once a coherent wave train was spotted a small window (2 to 5 wave periods) was established so that the wave could be found to be coherent within the window over several heights in all three beams. The original unfiltered data was fit with a sine curve plus linear trend to eliminate any long wave effects. Again, information on amplitude and phase as well as mean background flow was obtained.

The next step was to plot the phase information, or equivalently the time of maximum amplitude, as a function of height and look for equal phase progressions with height in all three beams. Matching phase progressions were easily obtained for the large amplitude, low frequency waves because they dominated the horizontal velocity fields

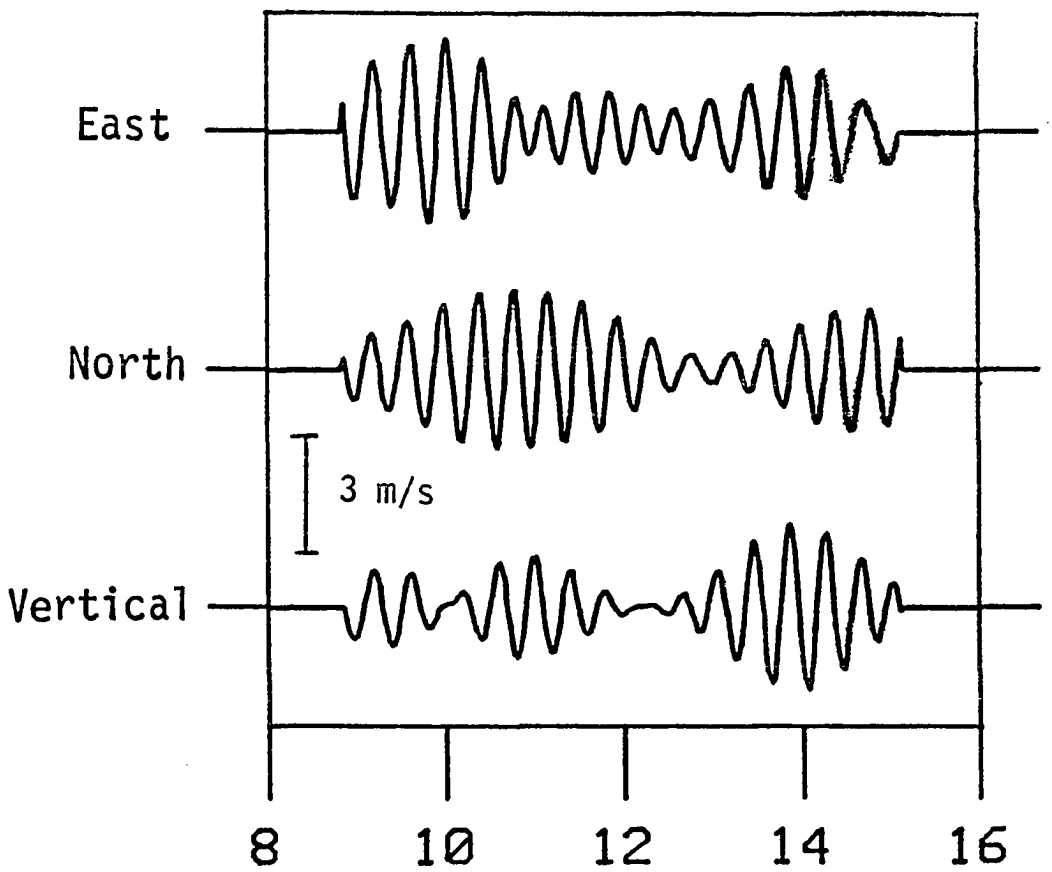

Figure 5.2 Digitally filtered velocities obtained from the data of Figure 5.1, using a bandpass filter with 3 dB points at frequencies corresponding to periods of 19 and 31 minutes and a center period of 25 minutes.

and could be readily fitted with a sine wave through the apparently random, higher frequency, small amplitude (about 1 m/s) gravity wave noise. However, the vertical velocity components of the long waves were not so readily apparent in the vertical velocity data because their amplitudes (.1 to .5 m/s) are less than the vertical velocities of the high frequency waves (1 m/s). Thus, vertical beam phase progressions appear noisier than those in oblique beams but appear to have the same slope as the oblique progressions allowing positive identification of the wave to be made.

Phase progressions for the high-frequency waves were not as coherent as for the low-frequency waves. There are several possible sources of interference, such as waves of similar frequency propagating in different directions or with different vertical wavelengths or that are masked by the larger amplitude waves of different frequencies. This last complication of low amplitudes could affect one measured component preferentially over the other two if the wave phase fronts were propagating along a radar beam. The wave perturbation velocity would then be nearly perpendicular to the radar beam, producing little Doppler shift of the radar signal and passing by without being observed.

Once a prospective gravity wave had been identified by linear phase progressions with height, its vertical

wavelength could be determined from the plotted data. Typical vertical wavelengths were about 15 km.

To determine the horizontal wavelength and phase speed, different assumptions were made for the low- and high-frequency waves. The low-frequency waves were identified as inertio- gravity waves from the phase plots and were analyzed in the same manner as the low-frequency waves in Chapter 4 were analyzed. The direction of propagation was determined from the major axis of the ellipse traced out by the perturbation velocity vector. Since the horizontal (u') and vertical (w') velocity components are in phase in the direction of wave propagation, it was possible to check the direction given by the ellipse axis by determining which direction would be in phase with w' from the phase plots. Most of the waves were propagating to the south (Table 5.1). Amplitudes, u', phase speed (c), and intrinsic phase speed (U-c) and u'w', in the direction of wave propagation, are given in the table.

The approximate horizontal wavelength was computed using the ratio of horizontal and vertical perturbation amplitudes and the continuity equation. Then, horizontal phase speed can be calculated as horizontal wavelength divided by the wave period. For the long-period waves, it was assumed that all three beams were sampling the same phase of the wave and that the measured phase differences

Table 5.1
Low-frequency wave parameters

Time of occurrence	10/11/81	10/12/81	10/13/81
Time	1300 AST	1300 AST	1300 AST
Height	58 - 72 km	62 - 73 km	62 - 71 km
Period (hrs)	10	7.67	5.16
Intrinsic period (hrs)	11.2	6.6	5.6
λ_x (km)	3640	860	1650
λ_z (km)	14.5	16.2	25.7
u' (m/s)	19.2$\pm$3.0	19.5$\pm$3.4	9.8$\pm$4.8
w' (m/s)	0.16$\pm$.35	0.36$\pm$.34	0.15$\pm$.29
Propagation dir.	195^o	160^o	230^o
c (m/s)	101	31	89
U-c (m/s)	90	36	71
u'/U-c	0.21	0.53	0.14
U_t (m/s/day)	9	~0	9.1

were due solely to the wave component differences. Then, with the measured vertical perturbation velocity being much smaller than the horizontal velocities, the measured oblique perturbation velocity components could be converted to actual horizontal components, neglecting vertical motions, with little error.

To retrieve horizontal wavelengths for the high-frequency waves, it was assumed that the phase differences between the three receivers was due to the differing times of arrival of the wave packet at the spatially separated sample volumes of the three beams. Assuming that only plane waves were propagating across the three independent beams at any single height, it was possible to compute an estimate of the phase speed and propagation directions across the three beams using the arrival time lags alone. A check on these values could be made by comparing the amplitudes measured along the beam pointing directions with the amplitudes that would be obtained from a wave travelling in the inferred direction. With the phase speed and the mean flow velocities in the direction of wave propagation, the proximity of the wave amplitude to the saturation threshold could be investigated. We have examined high-frequency waves occurring on October 11th and found that the 10 hr wave presented a highly variable mean

flow to the much shorter, higher frequency waves as will be discussed below.

5.2.1 Low-frequency waves

Large-amplitude, low-frequency waves were identified on the three days, October 11th to the 13th. The derived parameters are given in Table 5.1 where it can be seen that the waves were directed mainly to the south and the frequency appeared to increase with time. The uniform nature of the low- frequency motions suggests a common source about 5000 km to the north of Poker Flat.

The observed phase progressions and height profiles of the wave amplitude of the 10 hr wave on October 11 are shown in Figure 5.3 taken from Fritts et al. (1983). From the slope of the phase lines, the vertical wavelength is estimated to be 14.5 km. Since the horizontal to vertical amplitude ratio is about 120 to 1, the horizontal wavelength has been determined to be about 1740 km giving a horizonal phase speed of 48 m/s. The slope of the phase plots and the clockwise rotation of the perturbation velocity with time and with height indicate that the wave was propagating energy upwards and that the wave was travelling faster than the mean wind. The wave was travelling to the south as can be seen from the fact that the vertical velocity was a maximum about half a wave period before the maximum velocity in the north beam. The

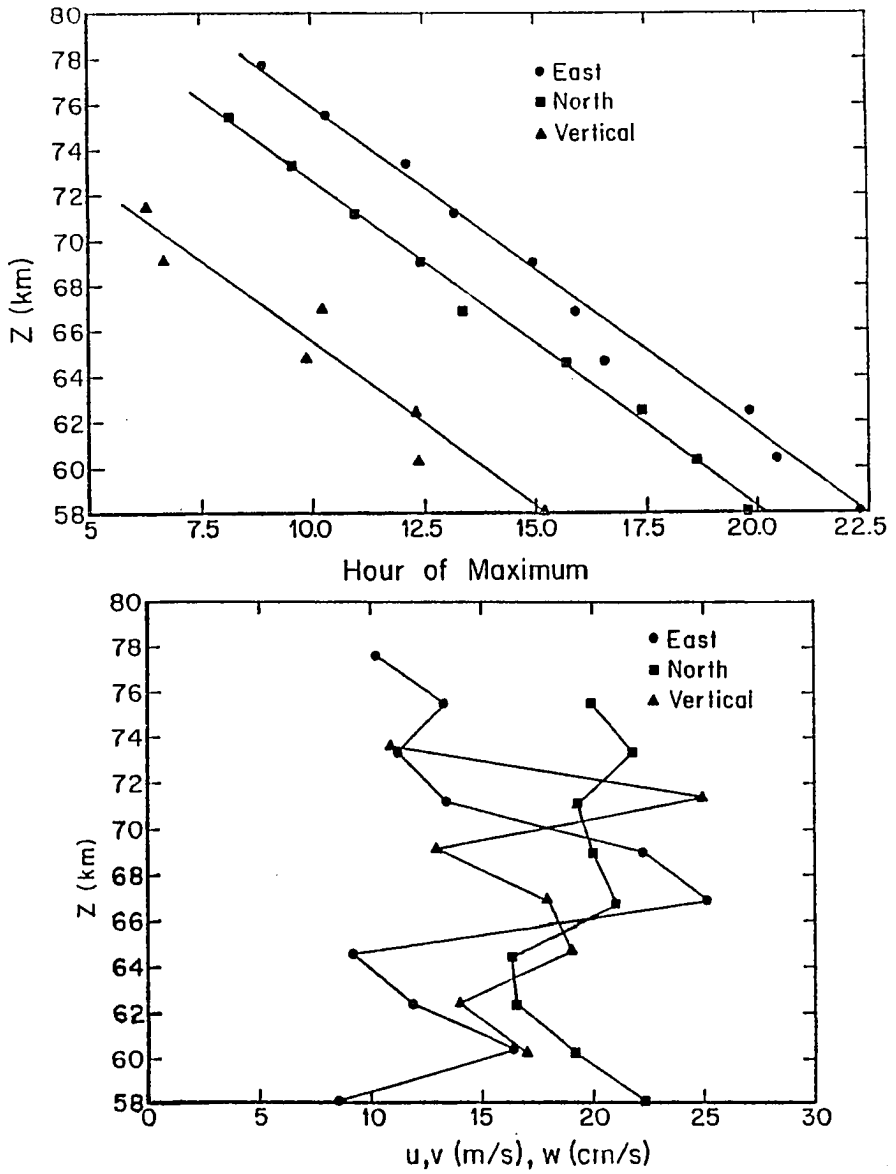

Figure 5.3 Phase (or time of maximum) and horizontal amplitude profiles for the 10 hr wave observed on Oct 11, 1981. For this figure alone, velocities have been converted to geographic coordinates (i.e., East is 90°E). From Fritts et al. (1984).

mean wind in the direction of wave propagation, over the 60 to 66 km height region, was near 11 m/s so that the intrinsic phase velocity was U-c = 37 m/s.

An estimate of the intrinsic frequency is needed in order to compute the saturation threshold. There are three methods of estimating the intrinsic frequency. The first method depends on an accurate measurement of w'. Horizontal wavelength and phase speed are estimated as in the preceding paragraph. Then, using U in the direction of wave propagation, the intrinsic frequency can be directly calculated and for this wave was found to be $2\pi / k(U-c)$ = 13.1 hrs. However, the 95% confidence limits for the vertical velocities are generally equal to or greater than the inferred vertical amplitudes, implying a straight line could have been fit to the data with equal confidence. However, the phases of the waves fit to the vertical velocity data provide distinct and clearly non-random progressions with height that match the phase progressions in the other beams. While the vertical amplitudes are known only to within a factor of two, the phase data clearly show that the wave motions are consistent in all three beams. It must be noted that a factor of two error in vertical velocity will produce a similar error in horizontal wavelength and phase speed. Thus, more precise measurements of vertical velocity are needed.

The second method is to iteratively estimate, as in section 4.2.1, U-c and k using the dispersion relation and the observed values of vertical wavelength (14.5 km) and U (11 m/s) and a value of N (0.02 rad/s from the CIRA 1972 model atmosphere). With this method, U-c is equal to 90 m/s, horizontal wavelength is 3640 km and the intrinsic frequency is 11.2 hr.

The final method is to use the ratio of the maximum velocity along the major axis of the ellipse to the minimun perturbation velocity along the minor axis at each height. For this method, the values of intrinsic period range from 5.8 to 11.4 hr. Uncertainties in wave amplitudes result in roughly 3 hr uncertainties in intrinsic period estimates.

The observations that c > U and that the velocity perturbation vector rotates clockwise with time and height imply upward energy propagation and that the intrinsic period is longer than the observed period. It must be that the intrinsic period is greater than 10 hr and less than the inertial period of 13.2 hr. The physically possible estimates given above range from 10.7 to 13.1 hr. Probably, the most reliable estimate is the 11.2 hr based on the vertical wavelength.

The saturation amplitude for this inertio-gravity wave can be calculated using the intrinsic frequency, k(U-c). With an intrinsic period of 11.2 hr, a value of 0.69 is

found to be the saturation threshold, u' / U-c, using eqn 2.26. The measured value of u' / U-c is 0.21. The nearly constant height profiles of wave amplitude indicate that this wave was saturated even though its amplitude was probably smaller than the saturation threshold. Since the wave was travelling to the south, the mean flow acceleration of 9 m/s per day, calculated using an H of 7 km, an assumed constant u' of 19 m/s and 3640 km and 14.5 km for horizontal and vertical wavelengths in eqn 2.28, induced by this wave was principally in the meridional direction.

The analysis for the following day is presented in Figure 5.4. The dominant wave motion was found to have a period of 7 hours and 40 minutes. The relative phases indicated that the wave was propagating to the southeast, about 20^{o}E of south. The inferred horizontal wave amplitudes increased approximately exponentially with height. The increase followed an $e^{z/2H}$ curve with H = 3.7 km from 62 to 71 km. The vertical velocity was approximately constant with height. This wave appeared to grow faster than ρ-1/2. Computation of the wave drag indicates that this wave was extracting energy from the mean flow. It must be noted that waves can appear to grow by propagating into an environment with a different value of N. The vertical wavelength changes in proportion to N

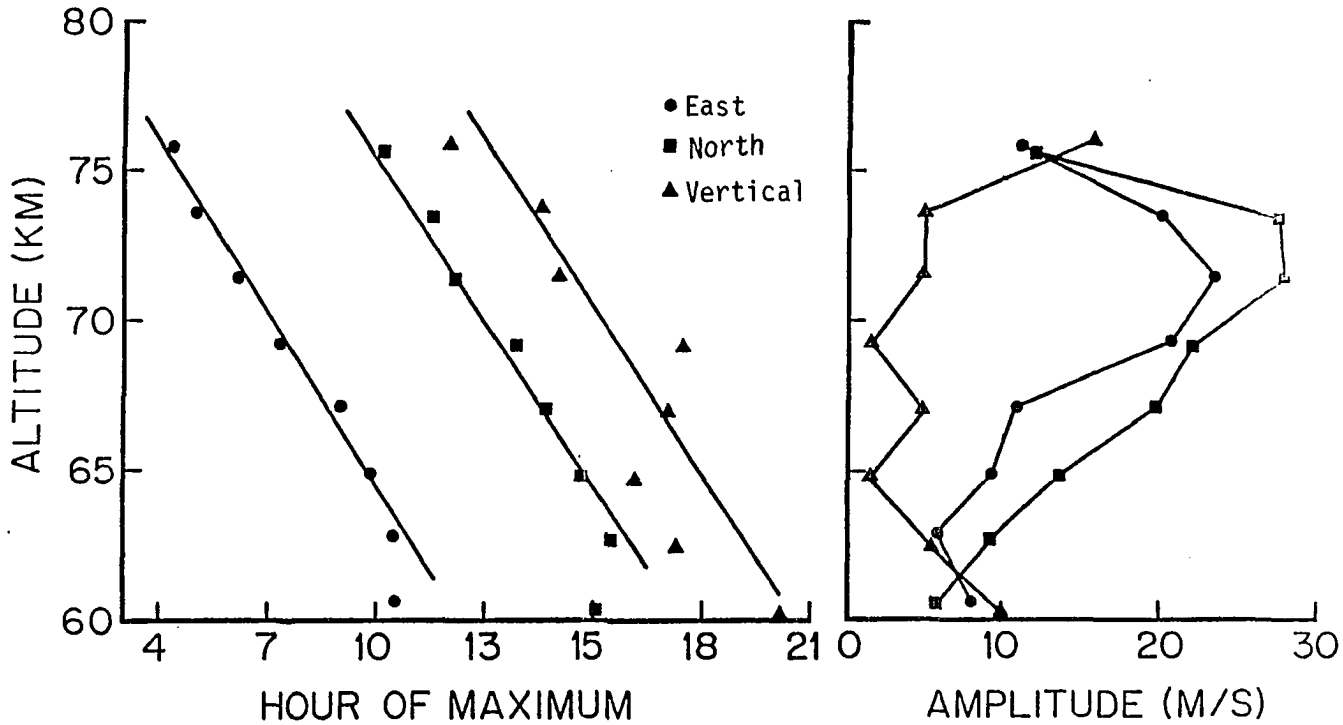

Figure 5.4 Phase and amplitude profiles for the 7 hr and 40 min period wave on Oct 12th. Velocity amplitudes are in radar coordinates. Vertical velocities have been multiplied by 10 to display them on the same scale.

and if the wave is compressed, u' would increase as w' would decrease. In any case, this wave propagated through the observing region with very little dissipation.

With both u' and w' growing with height we can use $u'\lambda z/w'$ to estimate the horizontal wavelength and phase speed. In this case the wave amplitude was less than half the convective instablity condition at 66 km, but it may have become unstable at greater altitudes. During October 12th, other waves must have been contributing to the instability of the wave field to generate the turbulence that allowed the radar to observe the low-frequency wave motion.

A low-frequency wave was also observed on October 13th having a period of 5 hours 10 minutes. This wave was also headed to the south, suggesting a common origin for the low frequency waves. As for the previous wave, the horizontal velocity perturbation was smaller than the estimated U-c. Thus, this wave could not saturate by itself, but its amplitude was nearly constant with height implying that this wave was being dissipated.

Neither of the long waves clearly identified on October 12th and 13th had sufficient amplitude to meet the saturation condition by themselves. Also, all the low frequency waves were headed mainly toward the south and therefore could not account for zonal mean flow changes,

only changes in the meridional flow. During the period, any zonal flow accelerations must have been caused by the saturation of higher frequency waves. Several higher frequency waves are examined in the following section.

5.2.2 High-frequency waves

The results of the analysis of the high frequency gravity waves are given in Table 5.2. An example of the amplitude and phase profiles of a wave with a period of 25 minutes is given in Figure 5.5.

The data for this wave are very noisy and it is difficult to find linear trends in the figure. Yet, over the interval from 65 to 70 km a reasonable fit can be made to the data. In that interval, the east and vertical beams record nearly the same wave amplitude and the perturbations in those two beams appear to be almost exactly in phase, whereas the north beam shows a much weaker amplitude and the presence of the wave about 16 minutes before the other receivers. The amplitudes and phases are consistent with a plane wave that is travelling towards an azimuth of 154^{o}E (directly opposite to the north beam direction) with almost equal vertical and horizontal wavelengths. The direction of propagation and the slope of the phase fronts then put the wave velocity vector close to perpendicular to the northward directed radar beam, causing a small amplitude to be recorded by the north beam.

Table 5.2
High-frequency wave parameters

Time of occurrence (AST)	1000	1200	1230	1330	1500
Window length					
Time (hrs)	1.25	1.5	3	1.5	1.2
Height (km)	58-62	58-62	62-66	64-68	64-75
Period (min)	26	28	50	25	20
Intrinsic period (min)	39	16	24	23	22
λ_x (km)	28	18	56	26	19
λ_z (km)	18	40	9	18	37
u' (m/s)	1.$\pm$.95	.3$\pm$.37	1.6$\pm$.9	1.1$\pm$.8	.4$\pm$.53
w' (m/s)	.63$\pm$.8	.5$\pm$.83	.25$\pm$.5	.74$\pm$.5	.6$\pm$.77
Propagation dir.	15^o	25^o	300^o	154^o	27^o
c (m/s)	12	11	18	18	19
U-c (m/s)	8	19	38	20	17
u' / U-c	0.12	0.01	0.04	0.06	0.02
U_t (m/s/day)	3.9	0.8	2.4	5.0	1.4

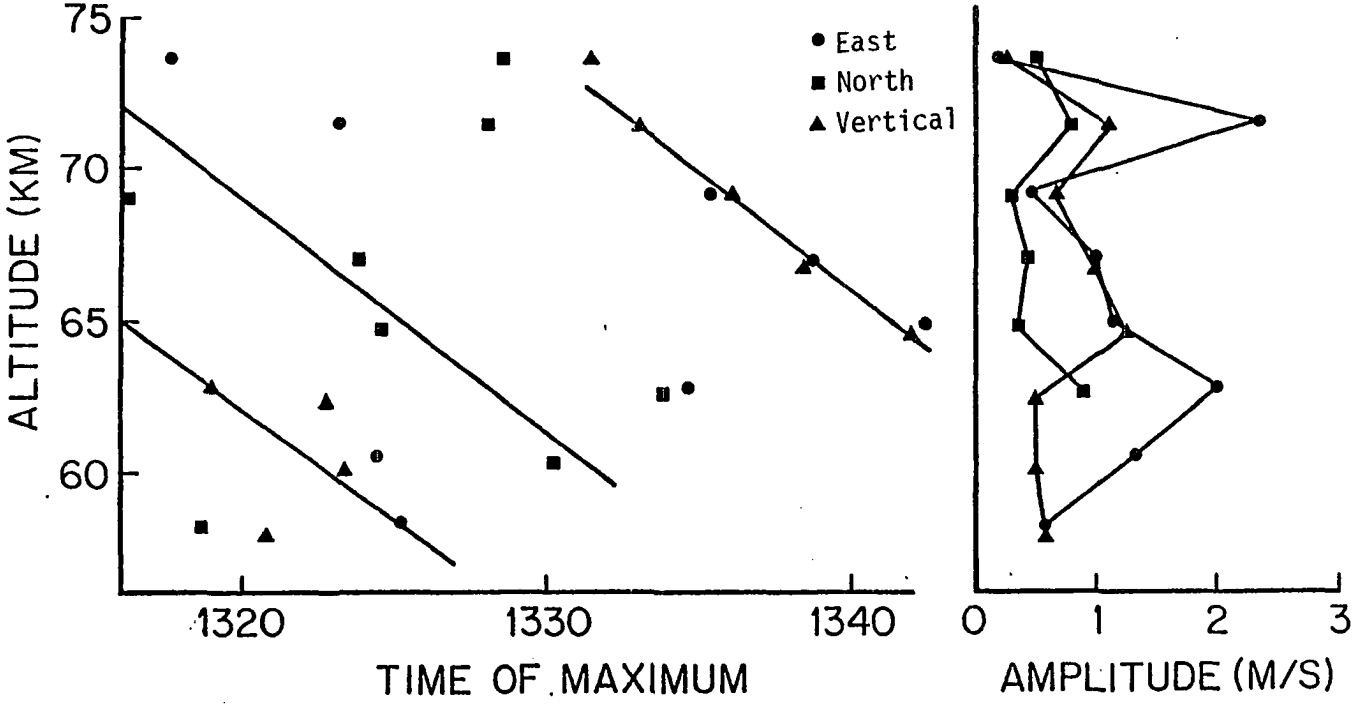

Figure 5.5 Phase and amplitude profiles for the 25 min period wave on Oct 11th. Amplitudes are of radial velocity components. Sloped line in lower left corner is an extension of the line in upper right that has been shifted by one wave period.

The data for U, over the 1.5 hours that the wave was phase coherent, also are not constant because the 10 hour wave contributed to the mean velocity field experienced by this shorter wave. However, over the 65 to 70 km region, the mean flow was approximately constant and an average was obtained for that region. Above 70 and below 65 km, large shears in U could be discerned so the 25 minute wave gave a consistent progression only over about half a vertical wavelength of the 10 hour wave.

The presence of the 10 hour wave would greatly filter and distort a uniform distribution of gravity waves with small phase velocities. At some points in the low-frequency wave and for certain high-frequency gravity wave phase speeds, critical levels would be formed and those waves would be absorbed. A varying mean flow will also have an effect on the vertical wavelength as illustrated by the approximate dispersion relation (eqn. 2.18), $m = N / (U-c)$. A wave-like U, such as that presented by the 10 hour wave, would modulate the vertical wavelength of shorter period waves and may be a cause of the noisy phase progression of Figure 5.5. In the case that U approaches c of the high-frequency waves, the vertical wavelength decreases, $u' / U-c$ becomes larger and instabilities will develop to dissipate the wave.

The other high-frequency waves of Table 5.2 were plagued with similiar problems and we have given the parameters only for the 6 or 8 km where everything could be consistently well fit. The facts that downward phase progression, that c was greater than U and that regions of constant amplitude were found for all waves suggest the waves were propagating energy upward and entering a region of saturation. These waves contributed to the accleration of the mean flow in several directions.

It was not possible to identify any monochromatic wave that was sufficiently near saturation to produce the observed turbulence. Therefore, the data point to a combination or superposition of waves as the cause of the wave field instability and the resultant turbulence and mean flow accelerations in the winter mesosphere. In the next section possible wave-mean flow effects are examined.

5.3 Mean flow characteristics

All radial velocity measurements from each oblique beam obtained during a given day were averaged to get the daily mean velocities shown in Figure 5.6. In this figure, positive velocities are associated with velocities toward 64^{o}E and toward 334^{o}E. Averaging over 10 to 14 hours effectively eliminates any vertical contribution to the radial velocity making it possible to convert these winds

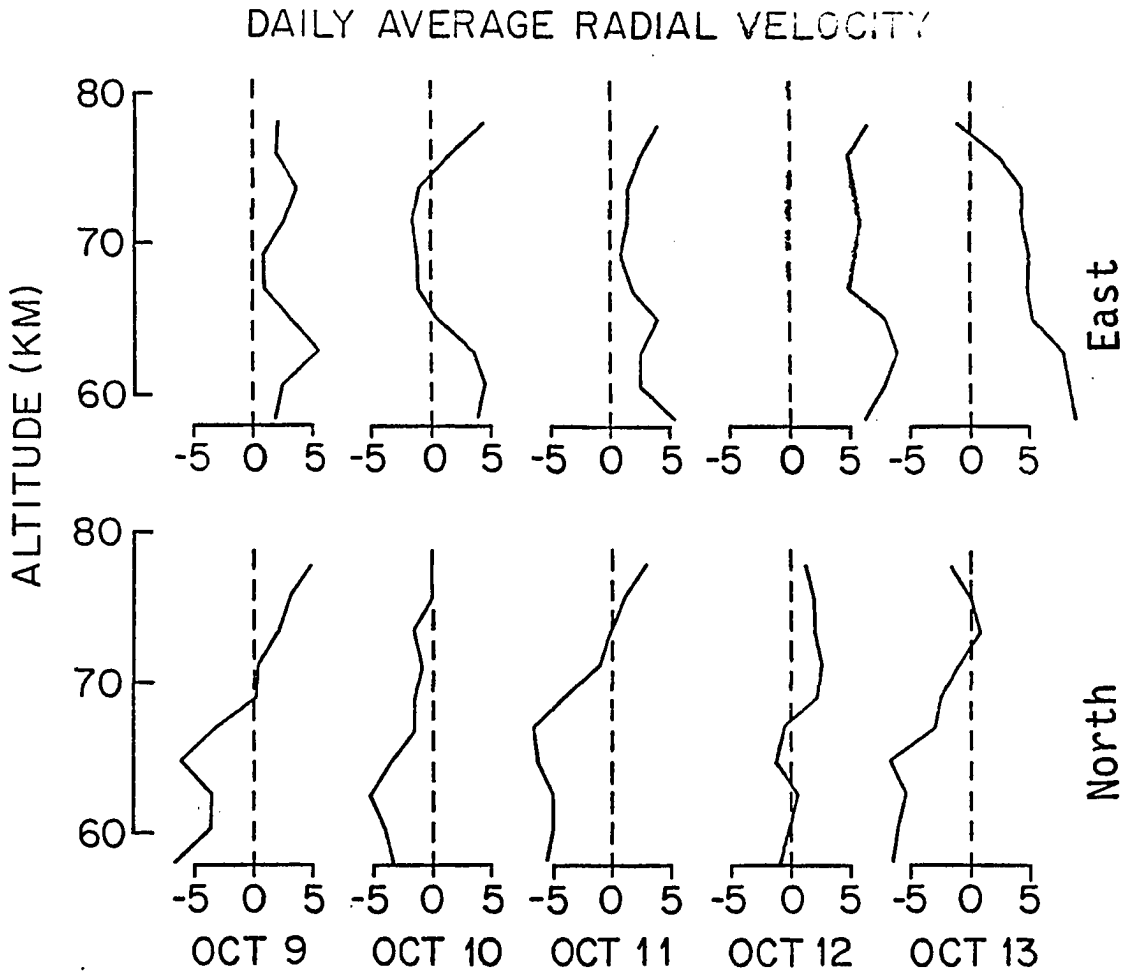

Figure 5.6 12 hour average mesospheric radial velocities (in m/s). Horizontal winds can be estimated by multiplying the velocities by 4 and rotating the axes.

to mean horizontal winds with a $1/\sin(15^{o})$ scale factor or roughly a factor of 4.

These averages are not true daily means because only 12 hours of data has been averaged. However, motions such as tides that would give a bias to the computed means do not appear as persistent features in the winter data. The horizontal velocities vary from day to day by tens of meters per second and if stationary tides were present they must have been small relative to the daily fluctuations.

One clue as to the source of the daily fluctuations is found in the root mean square deviations of the radial velocities from the computed daily mean velocity as shown in Figure 5.7. These deviations give an indication of the level of wave activity present. For example, the rms deviations for October 12 clearly reflect the height profiles of the amplitude of the 7.67 hr wave.

If the observed deviations were caused by non-dissipating, vertically propagating gravity waves, the deviations would increase with height proportional to $\rho^{-1/2}$ or $e^{z/2H}$. The dots on the October 9th curves are proportional to $e^{z/2H}$ with an H of 7 km, the largest scale height found in this region using the CIRA 1972 model atmosphere. As can be seen from the October 9th data, the chosen scale height is on the large side since the data exhibit a growth rate greater than the exponential curve

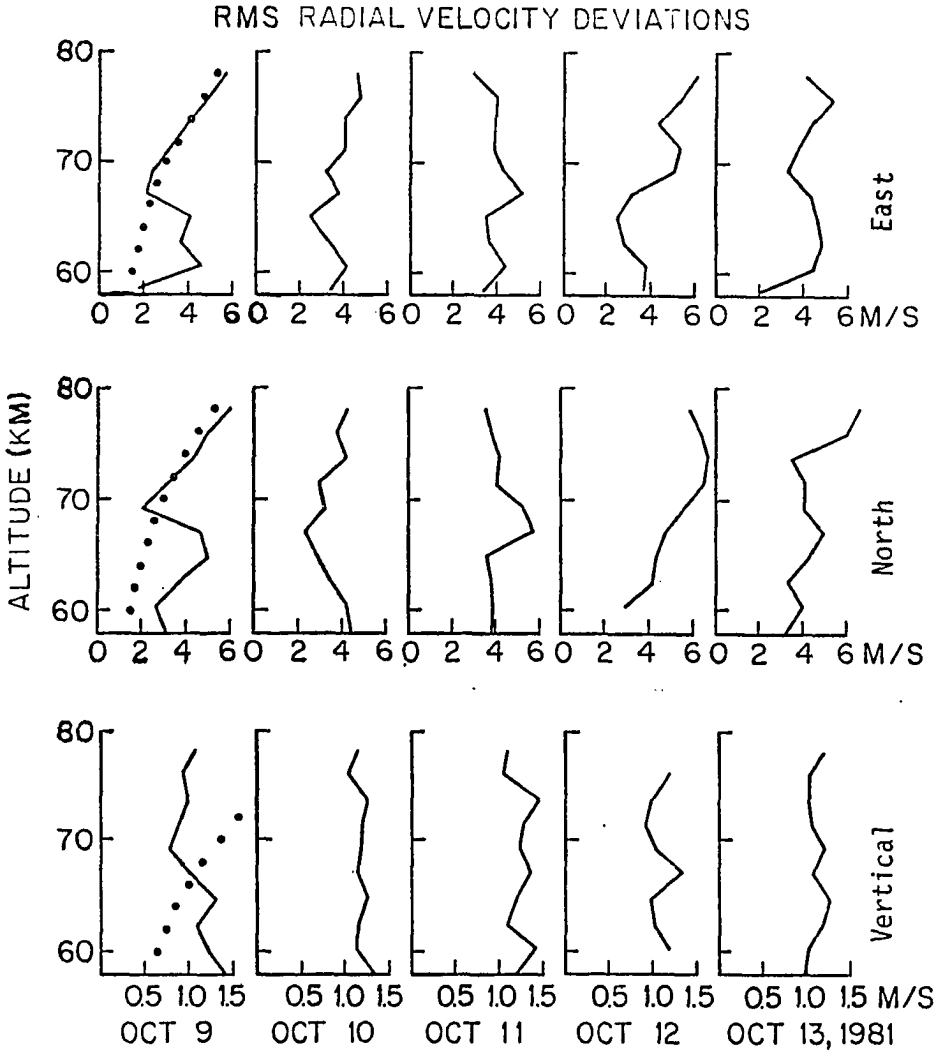

Figure 5.7 Root mean square velocity deviations from the means of Figure 5.6. Dots on leftmost profiles follow $e^{z/2H}$ curve with H = 7 km.

above 70 km. Again, waves propagating into regions of greater stability or decreasing U-c can exhibit growth of horizontal wave amplitudes at rates greater than the density decrease demands. However, several curves are constant with height and, in general, growth seems to occur at a rate equal to or less than $e^{z/2H}$. The approximately constant height profiles of velocity variations provide strong evidence for gravity wave saturation, since the curves do not exhibit exponential increases with height as expected for non-dissipating gravity waves.

Deviations in both oblique beams are approximately equal implying that the processes generating the deviations are homogeneous and isotropic. Yet, the mean flow accelerates toward specific directions requiring the accelerating agents to act non-isotropically. Specifically, the rms deviations on October 11th are equal in the two beams, yet the mean flow accelerated from the 10th to the 11th by up to 20 m/s to the south at 68 km. The saturation of the 10 hr wave can partially explain both sets of figures. As the wave period was close to the inertial period, the perturbation velocity contributions to either direction were nearly equal. The wave was saturating and providing an acceleration of about 9 m/s per day to the south. For this one wave, rms deviations would

appear nearly isotropic but mean flow accelerations would occur only toward the south.

Thus, evidence has been provided that a superposition of gravity waves with frequencies spanning a broad range lead to saturation, since no single wave could explain the observed saturation by itself. Changes in the mean wind reflect a convergence of momentum flux due to the saturating waves producing an acceleration in the direction of wave propagation. Larger scale motions, such as propagating planetary waves, also affect the mean flow in the mesosphere, but as can be seen from the above discussion and the accelerations given in the tables, gravity waves are quite capable of producing significant changes in the mean flow.

Chapter 6

Mesospheric Wind Spectra

In the previous two chapters, studies of nearly monochromatic gravity waves have been presented. It was shown that only the largest amplitude waves could be accurately identified and then only in the oblique beams. The search for single waves provides some insight into the behavior of waves but reveals little about average wave activity or the average scales and frequencies of mesospheric gravity waves.

Questions on the general nature of gravity waves and velocity fluctuations can be addressed through spectral analysis. By Fourier decomposing series of measured velocity values into frequency or wavenumber spectra, the average properties of all waves present can be examined. In this chapter, radial (along the radar beam) wavenumber power spectra will be presented and discussed. One problem with studies of spectral amplitudes is that the phase relations between the various wind components are lost, which means that all types of motions, not just gravity waves, are included in the spectra. Thus, a predictive model of gravity wave spectra is needed to identify that portion of the observed spectra that is due to gravity waves.

Radial wavenumber spectra, acquired with resolutions of 300 m and 1-3 minutes, will be presented. These spectra are compared with a 'universal' gravity wave model proposed by Van Zandt (1982, 1985). Initial indications are that the observations are consistent with a gravity wave model but because of uncertainties in the vertical velocity spectra, introduced by the DC filter - windowing process described in section 3.2.1, the comparisons do not exclude contributions from other types of motions.

The mesospheric wavenumber spectra are similar in shape and have amplitudes that are within a factor of 2 of stratospheric and tropospheric spectra, after scaling to a common value of N^2. This lack of growth with height from the troposphere to the mesosphere, for small vertical wavelength waves, reveals the existence of a saturation amplitude limit for wavenumber spectra to be discussed at the end of this chapter.

6.1 Possible spectral components

Recent studies of mesoscale (one to thousands of kilometers) wind fluctuations have led to two very different theories on the origin and evolution of such fluctuations. One view holds that the fluctuations are due to a spectrum of gravity waves transporting momentum vertically (Dewan, 1979; Van Zandt, 1982). The second view is that the small-scale motions are due to stratified, two-

dimensional (2D) turbulence. This stratified turbulence is characterized by turbulent eddies with wind fluctuations constrained to occur primarily in a horizontal plane that do not, in general, lead to vertical motions (Gage, 1979; Lilly, 1983).

No definitive conclusions have been made on the nature of the mesoscale fluctuations because both theories make similar predictions for some of the spectral properties of the motions. Both theories predict that horizontal wavenumber spectra of horizontal velocity fluctuations should be proportional to $k^{-5/3}$ (Dewan, 1979; Gage, 1979). A -5/3 power law also applies to frequency spectra. Van Zandt's 'universal' gravity wave model, which is an empirical model, employs an ω-5/3 while the stratified turbulence frequency spectrum is assumed to fit an $\omega^{-5/3}$ power law by a 'Taylor' transformation of the horizontal wavenumber spectra. This transformation assumes that the isotropic turbulence is frozen in and advected by the mean flow to produce the -5/3 sloped frequency spectrum. Hence, neither horizontal wavenumber nor frequency spectra of horizontal velocity fluctuations, by themselves, can be used to differentiate between stratified turbulence and gravity waves.

Both types of motions are undoubtedly present in the atmosphere as they are in the ocean (Muller et al., 1978).

The separation of the oceanic turbulence and wave spectral contributions was achieved through use of a dense array of current and temperature sensors. By examining spatial and temporal coherences between velocity components measured at vertically and/or horizontally separated locations throughout the array, Muller et al. found that the majority of the fluctuation spectrum could be explained by a wave model, but that temperature and current 'finestructure' also contributed. This finestructure has been tentatively associated with 2D turbulence by Muller (1984).

It would be desirable to quantitatively partition the atmospheric velocity spectrum between waves and 2D turbulence in order to study the evolution of the spectrum and the interaction of the motions with the environment. Since gravity waves transport energy and momentum vertically as opposed to 2D turbulence, which operates only horizontally, an accurate determination of the gravity wave energy and momentum flux at a specific height would provide estimates of mean flow drag, vertical transport of heat and chemical constituents and changes in turbulence intensity caused by variations in gravity wave saturation at other altitudes.

Separation of the atmospheric velocity spectrum has proved difficult due to the impossibility of measuring all

three wind components over a dense horizontal and vertical spatial array with high time resolution. However, MST radar measurements have permitted an initial assessment of the relative contribution of gravity waves to the spectrum.

6.2 Gravity wave spectral model

The spectral model proposed by Van Zandt (1982, 1985), employed in the following comparisons, is patterned after the successful empirical model of oceanic internal gravity wave spectra by Garrett and Munk (1972, 1975). Employing accumulated frequency and wavenumber spectra obtained in the deep ocean, presumably far from wave sources or sinks, Garrett and Munk were able to generate model spectra that matched observed spectra over a wide range of sites and conditions.

Van Zandt (1982) adapted the Garrett and Munk model to atmospheric spectra based on observations of the frequency wavenumber spectra of horizontal velocity fluctuations. He was able to take the form of the Garrett and Munk model and with minor changes in exponential powers, obtain reasonable fits to frequency, horizontal and vertical wavenumber spectra that had been obtained at widely varying locations and in different seasons. A basic assumption of the model is that the total gravity wave energy spectrum is composed of two separable components: one being the frequency

spectral component and the other the wavenumber spectral contribution.

Since the frequency and wavenumber components are assumed independent and separable it might seem as though any frequency or wavenumber spectrum could be made to fit the model. However, the gravity wave dispersion relation between frequency and vertical and horizontal wavenumbers does provide a consistency check and a means of transforming one type of spectrun to another. Van Zandt (1982) demonstrated that average frequency and vertical and horizontal wavenumber spectra agreed with the model spectra to within a standard deviation of the observed spectra (about a factor of 2).

The model wavenumber spectrum is obtained by integrating the total energy expression over frequency and the frequency spectrum is obtained by integrating over the wavenumber spectrum. These simple manipulations are all that is needed for spectra of horizontal or vertical wind fluctuations since the model was formulated from such observations. However, the composition of the gravity wave spectrum along an oblique path is needed for use with MST radars since it is not possible to separate the horizontal and vertical spectral components from measurements made along oblique beams. Extrapolating the model to predict fluctuation spectra along any oblique path requires further

use of gravity wave theory. We will review the derivation of obliquely sampled gravity wave spectra to indicate what parameters the model requires. (For a detailed derivation see Van Zandt (1985).)

Several studies of frequency spectra of radar measured velocities have been published (Balsley and Carter, 1982; Frezal et al., 1981; Rottger, 1981 and Vincent, 1984). The spectra generally exhibit a power law relation between power spectral density and frequency of the form $A\omega^{-p}$. The exponent p is in the range from 1.1 to 2.0 with the most frequent value being 5/3. One such spectrum, from Balsley and Carter (1982), is shown in Figure 6.1. This spectrum was obtained during two consecutive summers from a height near the mesopause using velocities measured along the east beam. From the inertial frequency ($f = 2.1(10^{-5})$ cycles/s) to the Brunt-Vaisala frequency ($N = 3(10^{-2})$ cycles/s), power spectral density is proportional to $\omega^{-5/3}$.

The model can be used along with the frequency spectrum of horizontal velocity fluctuations to predict the amplitude and shape (or slope) of the vertical velocity frequency spectrum. Horizontal to vertical wave amplitudes can be related to frequency using the continuity equation (eqn 2.21) and the dispersion relation (eqn 2.18) with the result

$$u' / w' = N / \omega$$

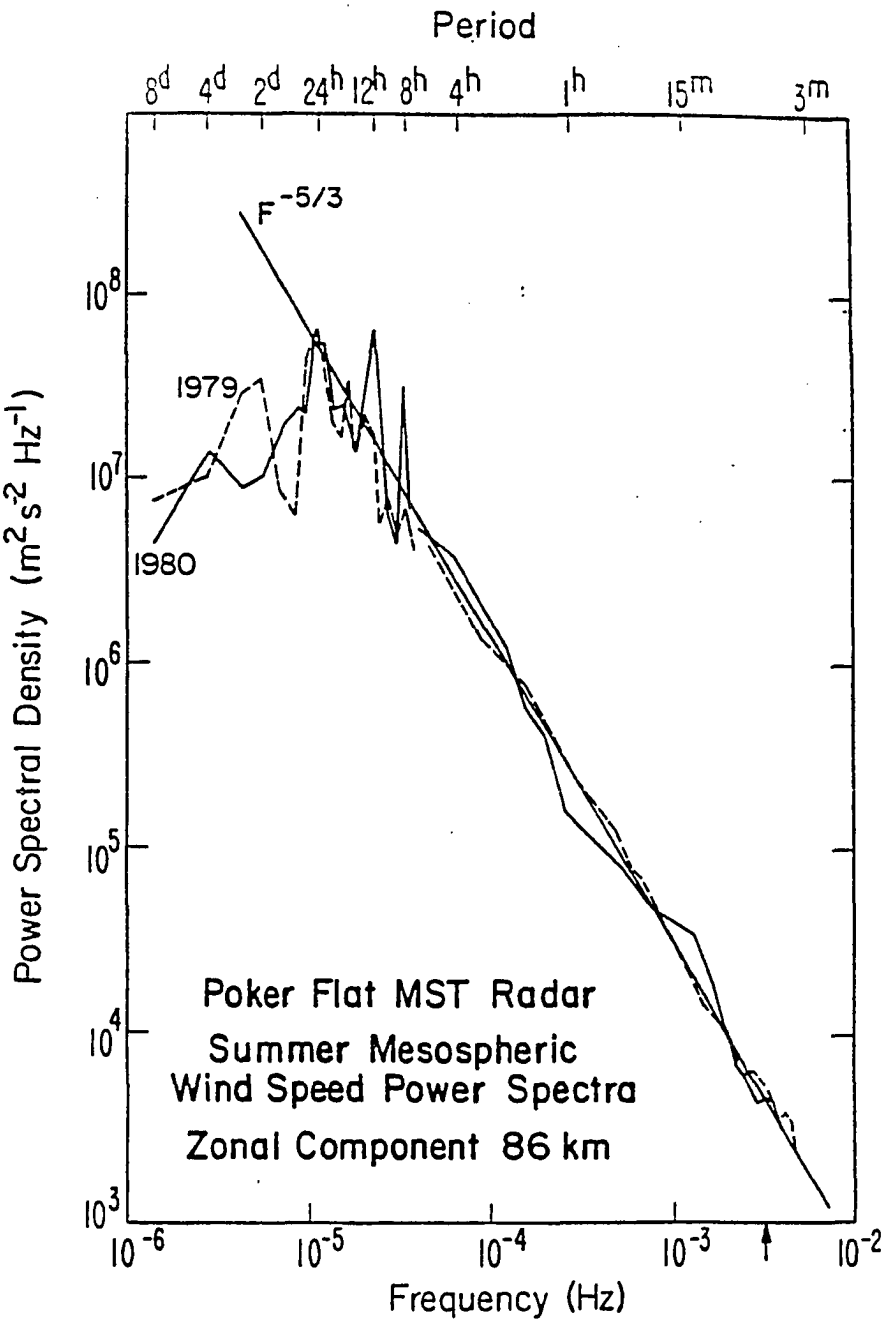

Figure 6.1 Power spectra of zonal wind fluctuations from Balsley and Carter (1982).

assuming the mean wind is zero and $N > \omega > f$. Thus, if the horizontal velocity power spectrum, u'^2, is proportional to $\omega^{-5/3}$, then the vertical velocity power spectrum, w'^2, is proportional to $\omega^{1/3}$. Vertical velocity spectra usually exhibit an -1 shape in contrast to the +1/3 slope predicted by gravity wave theory. However, some vertical velocity frequency spectra do have an ω^0 shape under 'quiet' wind conditions (Ecklund et al., 1985).

These observations have led to the hypothesis that the model does not match the observed frequency spectra because the model assumes that the mean wind is zero. A non-zero mean wind results in a Doppler shifting of the wave frequency measured by a stationary observer to another frequency. This Doppler- shifted frequency is the important one in determining the characteristics of propagating gravity waves.

The neglect of Doppler shifting has no effect on vertical wavenumber spectra. This can be seen by considering an atmospheric fluctuation spectrum observed in a zero mean wind environment. If an observer is in motion relative to the atmosphere with the zero mean wind, he will observe a frequency spectrum different from that seen by a stationary observer. However, if the moving observer made an instantaneous vertical sounding of the atmosphere he must observe the same vertical wavenumber spectrum as

observed by the stationary observer since the observer motion can have no effect on the motions of the atmosphere. The uncertainties in the model that may prevent an accurate match of frequency spectra do not enter into consideration when discussing vertical wavenumber spectra. For this reason we have concentrated on observations of vertical wavenumber spectra.

The gravity wave velocity perturbations measured along an oblique beam will be a combination of horizontal and vertical velocity perturbations. The ratio of horizontal to vertical velocity perturbations for gravity waves is determined by the gravity wave dispersion relation which in this formulation is obtained from a WKB solution to the wave equation. With the dispersion relation and the zenith angle of the sampling vector, a formula is derived for the measured wave perturbation in terms of the absolute amplitude and frequency of a wave. Though, as pointed out by Van Zandt (1982), there is evidence for a uniform wave amplitude over a wide range of observing sites and seasons, we avoid any uncertainty in the amplitude by using ratios of spectral amplitudes observed at different zenith angles. The absolute amplitude cancels out of the ratio. If the fluctuations are due to gravity waves, then the ratio should agree with the ratio predicted by the gravity wave dispersion relation. Thus, we are not investigating the

universality of the gravity wave model but rather the application of the gravity wave dispersion relation to the observed fluctuations.

6.3 Observed vertical wavenumber spectra

Mesospheric wind velocities were obtained from a vertical beam and two oblique (15^{o} off-zenith) beams, between heights of 82 to 88 km, during the STATE campaign in June 1983 and also during a similar radar campaign in July 1984. Before transforming the velocity measurements to wavenumber spectra, spurious points due to aircraft and meteors in sidelobes and other types of interference were removed. An empirical editing procedure was used similar to those described by Carter (1983). The velocity time series from each beam and from each height was examined for accelerations greater than 3 times a running average of acceleration. Any points exceeding that limit were removed from further processing.

In order to compute ratios of oblique to vertical spectral densities over the greatest range of wavenumbers, individual profiles were selected that continuously covered the largest height interval. This height interval was limited by the vertical system which is about 10 dB less sensitive than the oblique system. The final height interval was also determined by the number of resultant spectra, with equal numbers of points, available to be

averaged together to improve the confidence level. Thus, the height interval (and corresponding wavenumber interval) selected was a compromise between the greatest interval available and the interval continuously sampled most frequently.

The linear trend of each selected profile was removed leaving fluctuations about the mean shear. The profiles were 'prewhitened' by differencing data points from successive heights, which is approximately equivalent to taking the first derivative. The differenced data were then cosine windowed to ensure periodicity of by smoothly reducing the data to zero at the endpoints and to minimize power leakage across the spectra. The differenced profiles were then transformed to the wavenumber domain using an FFT (Fast Fourier Transform) routine. The real and imaginary coefficients were squared and added to obtain a power estimate at each wavenumber. Finally, the wavenumber spectra were adjusted to reverse the effect of the differencing and the cosine windowing. The spectra were normalized, such that integration of a spectrum equalled the variance of the original profile, yielding power spectral densities.

Several power spectra were averaged together to narrow the confidence limits. The extent of the averaging was determined primarily by the extent of vertical winds

measured over a sufficiently large height range. Since the radar echoes were not continuous in time, averaging when signals were strong in the vertical beam means that our observed spectra are representative only of periods during which the intensity of 3 m scale-size, refractive index irregularities was greatest. The mesospheric irregularities are due to turbulent mixing of the electron density gradient. Thus, the level of turbulence and/or the electron density gradient was enhanced during the selected periods. These spectra, from times of enhanced radar signal strength, probably represent an upper limit to averag power spectra from the summer mesosphere over Poker Flat.

Spectra from three such periods are shown in Figures 6.2, 6.3 and 6.4. Each spectral curve is labelled by the beam from which the velocities were obtained with the number of spectra in each average given in parentheses. 95% confidence limits have been computed for the curve in each figure with the smallest number of averaged spectra, using the degrees of freedom for a Bartlett spectral window and the procedure of Jenkins and Watts (1968). Successive velocity profiles are not completely independent so the actual degrees of freedom are less than we have used and the confidence limits somewhat broader.

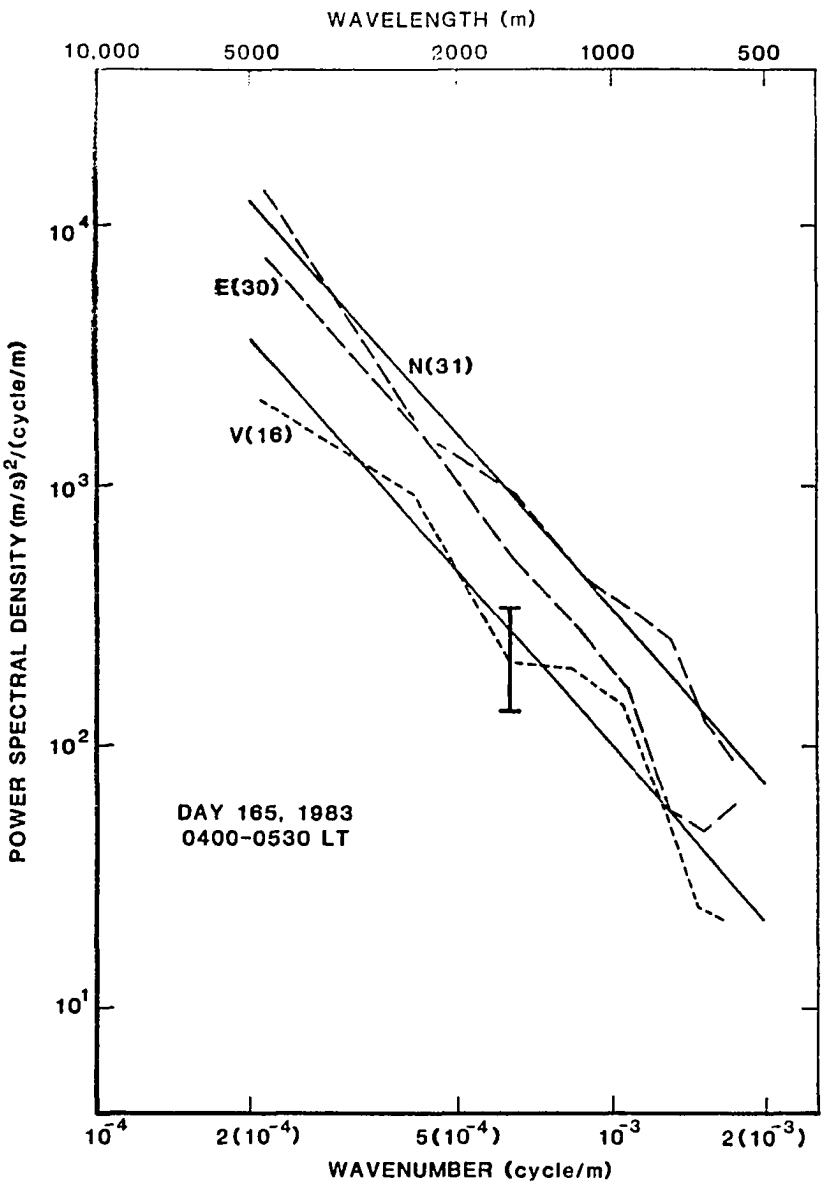

Figure 6.2 Vertical wavenumber spectra for day 165, 1983 (June 14). Dashed lines are spectra computed from observations along East, North and Vertical beams. Each spectra is the average of the number of spectra in parentheses obtained between 0400 and 0530 local time. Error bar is approximate 95% confidence limit. Solid lines are the model spectra.

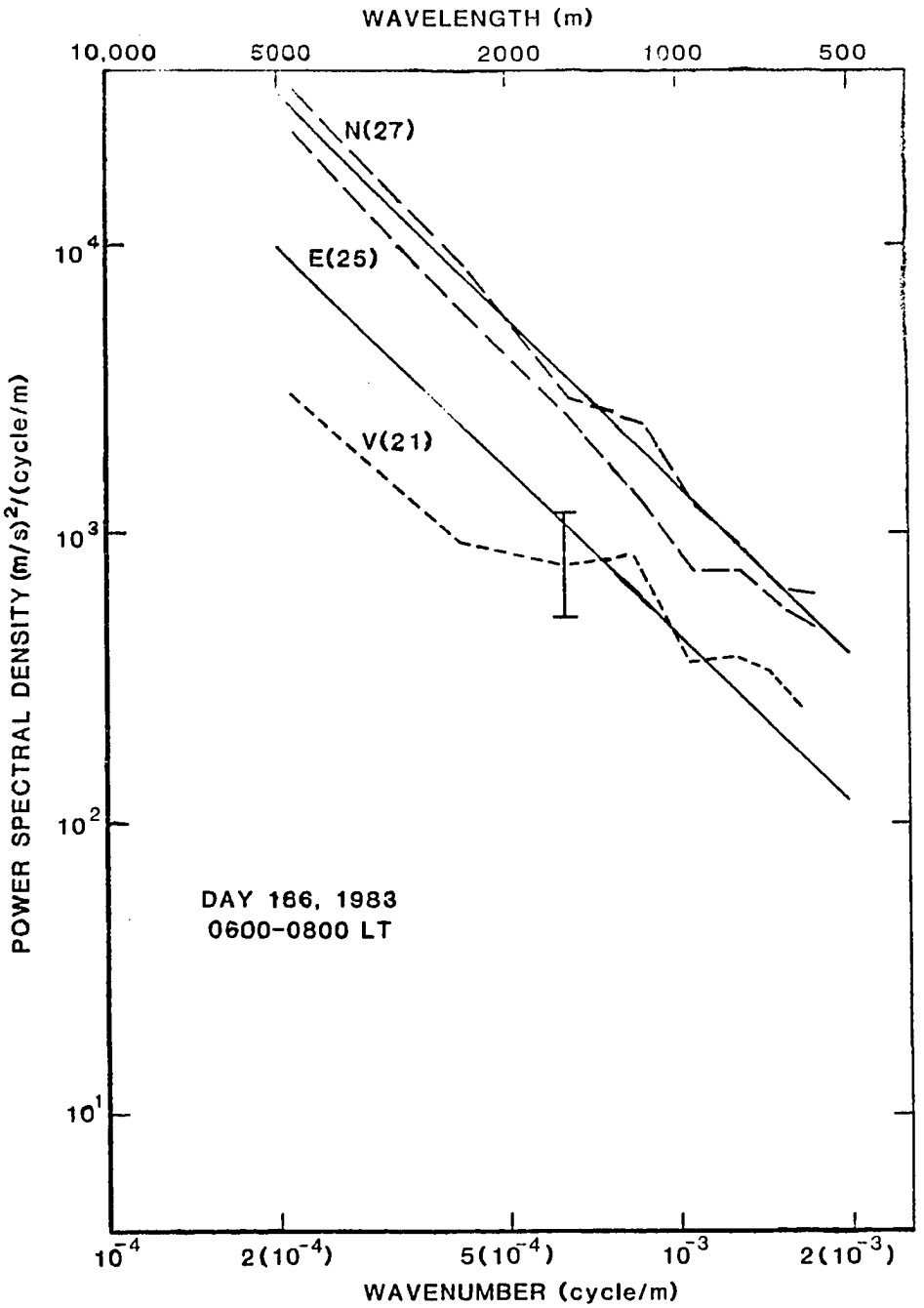

Figure 6.3 Same as Figure 6.2, but from day 166, 1983 (June 15).

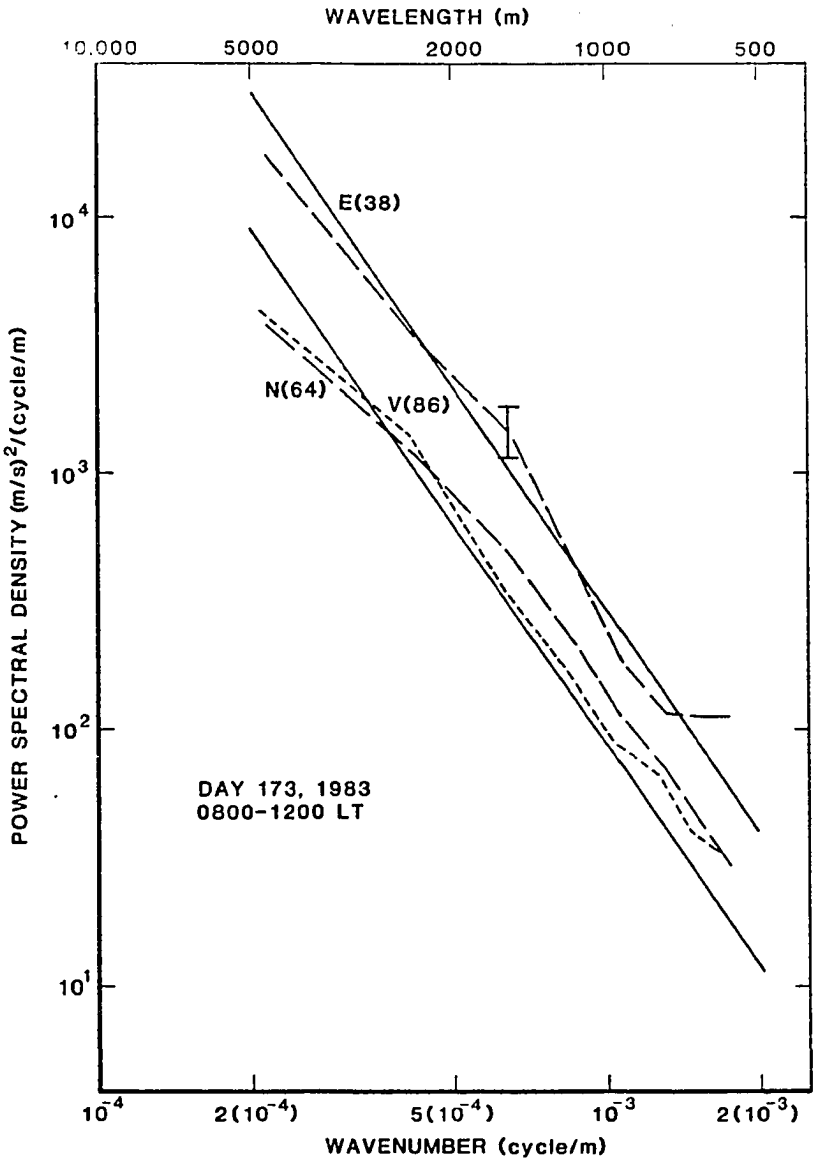

Figure 6.4 Same as Figure 6.2, but from day 173, 1983 (June 22).

To apply the model to the data we specified the zenith angles of the radar beams, the slope of the horizontal velocity perturbation frequency spectra and the limits on the range of gravity wave frequencies. The theoretical frequency limits are the inertial frequency and the Brunt-Vaisala frequency. The frequency spectral slope was taken to be -5/3 and the inertial frequency used was fixed by the latitude of the Poker Flat radar. The Brunt-Vaisala frequency was estimated to be .02 rad/s from a temperature profile derived from rocket data obtained during the STATE campaign. We have used Van Zandt's (1985) calculations with his n = 0.002984 cycles/s which corresponds to N = 0.019 rad/s. The model ratio was computed using a wavenumber spectral slope of - 2.5. We also specified the averaging period as 1.5 minutes.

In fitting the model curves to the observed spectra, the spectral slope was chosen to give the best straight line fit to the oblique spectra. The best fit slopes were approximately - 2.3, -2. and -2.8 for the spectra of days 165, 166 and 173 respectively. Grand averages of these spectra plus four other summer spectra produced average slopes of -2.23, -2.19 and - 1.92 for the east, north and vertical spectral. Note that the model ratio is insensitive to the specified wavenumber slope parameter. Thus, choosing a slope of - 2.5 applies equally well to

each of the figures. Once a straight line had been fit to the oblique spectra, the model ratio was used to construct the expected vertical velocity spectra. The model curves are plotted as the solid lines in the figures. The agreement is good for high wavenumbers.

The average of the seven spectra is shown in Figure 6.5. The log of the average observed ratio from the seven profiles was 0.3 at the 10^{-3} point (1 km wavelength), while the model predicted a log ratio of 0.53. There is also an indication of considerable day to day variability and anisotropy of the spectra in the east and north beams.

6.4 Comparison of the model and observed spectra

The spectra computed from the radar observed velocities exhibit several points of similarity. The magnitudes of the oblique spectra are generally within a factor of 3 of each other. The spectral slopes from separate beams are approximately parallel. Indeed, the average of the seven spectra results in equal power spectral densities for the two oblique beams. However, the slopes of the vertical power spectra are not as steep as the oblique spectra and an instrumental bias may account for this discrepancy. As demonstrated in section 3.2.1, summer mesospheric vertical velocity energy spectra may be artificially enhanced by a factor of 2 as a consequence of the DC filter - windowing processing. Since the processing has the largest effect on

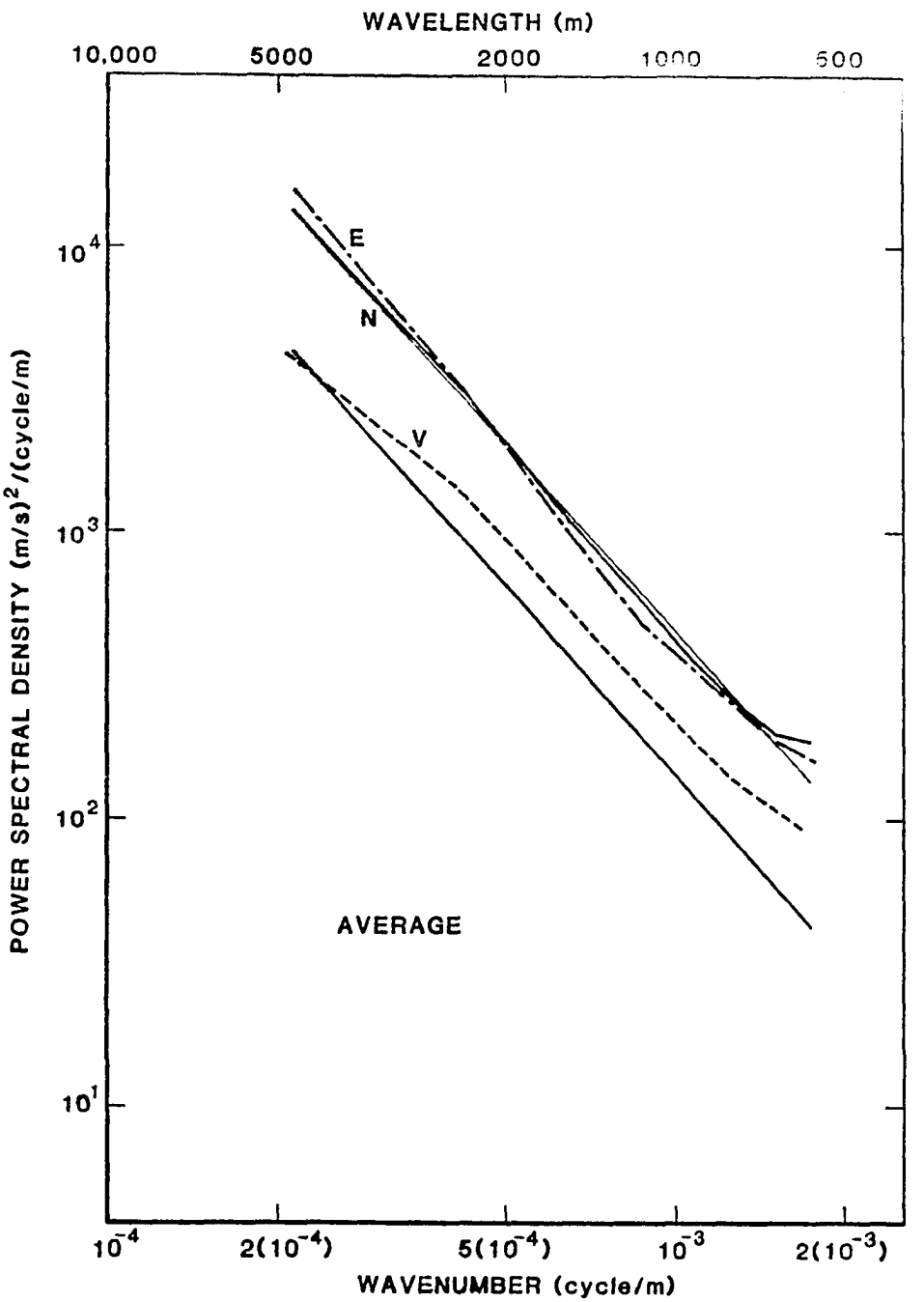

Figure 6.5 Average spectra obtained from all spectra contributing to Figures 6.2 - 6.4 and spectra from 4 other periods during the summers of 1983 and 1984. The thin straight line amongst upper curves is the model spectra. Note the increase in amplitude of the vertical spectra at high wavenumbers.

velocities closest to 0 m/s, we hypothesize that the smallest amplitude portions of the spectra are affected the most. For vertical wavenumber spectra, the high wavenumber segment has the smallest amplitudes. Increasing the spectral amplitude at the high wavenumber end of the spectra would also decrease the spectral slope and may explain the smaller slope observed on the vertical spectra.

The agreement between the observed spectra and the gravity wave model, while not perfect, does provide justification for a gravity wave interpretation. With this comparison, the relative contributions of gravity waves and 2D turbulence to the fluctuation spectra can begin to be addressed. Since 2D turbulence does not generate vertical motions, on average, the observed vertical velocity spectra are primarily due to gravity waves. Then that portion of the oblique spectra that agrees with the vertical spectra plus the log of the model ratio is probably contributed by gravity wave motions. The excellent agreement shown in the figures suggest that most of the velocity fluctuations are gravity wave motions and that there is little contribution from 2D turbulence. The average spectra show a log ratio of 0.3 at the 1 km wavelength point. As stated before the DC filter - windowing may account for a factor of 2 increase in the vertical spectral amplitude which means that the log of the actual vertical velocity spectra could

be 0.3 less than the measured amplitudes. This suggests that the oblique spectra may be larger than the vertical by a factor of 10.6, whereas gravity waves could account for a factor of 10.53, via the model calculations. Thus, there is a 17% surplus energy above the gravity wave spectral amplitude that could be attributed to 2D turbulence.

The fluctuation spectra exhibit azimuthal anisotropy that varies from day to day. For instance, on day 173, the north and vertical spectra are nearly equal, implying that the north beam is recording only vertical fluctuations while horizontal fluctuations are principally aligned east-west. With measurements in only two directions, determination of the exact shape of the azimuthal dependence is impossible. This anisotropy has an impact on the agreement between the model and observations but the difference cannot be quantified until similar measurements are made over a broader range of azimuth.

The observed anisotropy can result from anisotropy in wave sources or from the selective transmission of gravity waves through an anisotropic wind field at lower levels. However, anisotropy argues against domination of the spectra by 2D turbulence, as such turbulence would presumably lead to azimuthally isotropic horizontal velocity fluctuations.

Isotropy is recovered when spectra are averaged for a sufficiently long period. Averages of the seven sets of spectra show that the mean east and north spectra are approximately equal in contrast to the short term averages presented in the figures. These observations seem to suggest that the fluctuation spectrum is isotropic over long time scales, but that large anisotropies can exist for breif periods. This long term isotropy is most likely not a consequence of 2D turbulence but due to a spectral amplitude limit to be discussed in the next section.

6.5 Saturated wavenumber spectra

The gravity wave model used in our comparison has been billed as 'universal' (Van Zandt, 1982) in that mean observed spectra have similar amplitudes, independent of season or meteorological conditions. Dewan et al. (1984) have published further evidence for universality, exhibiting stratospheric vertical wavenumber spectra of horizontal wind speed inferred from the motions of smoke trails, observed in New Mexico, Virginia and Manitoba and at times ranging from April to September, that are very nearly identical. As will be discussed, wave saturation provides an accurate and simple explanation for this apparent universality.

We have combined vertical wavenumber spectra of horizontal wind fluctuations from several sources that

cover the height range from the ground to 130 km in Figure 6.6. These spectra show that small vertical scale waves are saturated throughout the lower and middle atmosphere. The troposphere curve is the smoothed spectrum of speed deviations from a time averaged profile of winds obtained with the use of Jimspheres by Endlich et al. (1969). This curve is an average of the spectra from six wind profiles, acquired at roughly 2 hr intervals, from which the average wind profile has been subtracted. The profiles covered heights from the ground to 16 km at Cape Kennedy and thus were primarily tropospheric data. Endlich et al. state that at high wavenumbers (> 1 cycle/km) the slope is approximately -2.5.

The best fit curve of Dewan et al. (1984) to their stratospheric spectra is displayed as the stratosphere curve in Figure 6.5. This curve follows an $m^{-2.7}$ power law from a wavenumber of 10^{-3} (= 1 km) down to .05 cycles/m (= 20 m).

The curve labelled mesosphere in the center of the graph is the inferred horizontal velocity spectra from the average of the six summer time spectra described in the previous section. The average vertical velocity spectral amplitude was subtracted from the oblique spectra and the result multiplied by $(1/\sin 15^{o})^{2}$ to convert to horizontal velocity spectra. Note that the average east and north

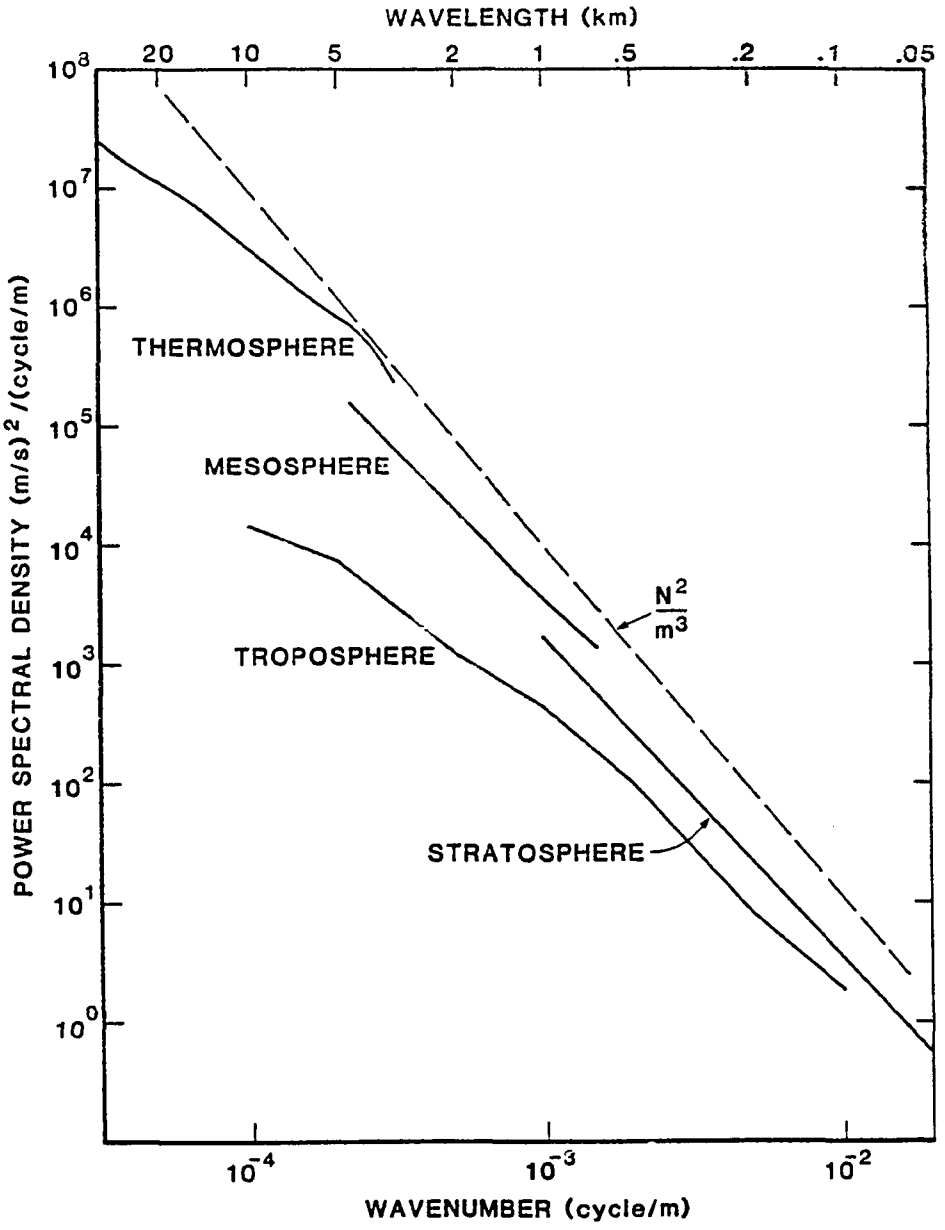

Figure 6.6 Composite plot of vertical wavenumber power spectral density from several sources. Note that the spectra from stratopshere, mesosphere and lower thermosphere have about the same amplitude and that it is less than the theoretical single wave saturation limit of $(N/m)^2$.

beam spectra were very nearly equal and so only one curve is plotted. The other curves are spectra of scalar wind speed while this mesosphere curve is the spectra of a single component of the wind and therefore may be an under estimate of the wind speed spectra by possibly the square root of 2, as the east and north spectra are approximately equal.

The thermosphere spectra was obtained from winds measured from 85 to 130 km by the three-axis accelerometer sphere during the STATE campaign. This spectra is of the scalar wind speed measured by the rocket and has been smoothed by two passes of a 3 point running average to increase the confidence level but this curve remains the most uncertain in the figure.

Figure 6.6 clearly shows that not only the spectral shape but the amplitude is very similiar from the stratosphere to the lower thermosphere. This spectral similarity can be extended to the troposphere by scaling the spectra to a common value of N^2. Dewan et al.'s data as well as the radar and STATE data were obtained from regions with an N of approximately .02 rad/s (Brunt-Vaisala period near 5 minutes). The troposphere typically has a value of N that is half the stratospheric N. Thus, an increase of Endlich et al.'s data by a factor of 4 is

indicated which would very closely align the curve with Dewan et al.'s data at the higher wavenumbers.

The amplitude limit of short vertical scale fluctuations is quite likely the result of convective and dynamic instabilities acting to dissipate wave energy. The instabilities arise when the waves attain a certain saturation amplitude. The saturation amplitude for waves with frequencies far from either f or N is $u' \sim U-c = N/m$. The power spectral limit of N^2 for an N of 0.02 rad/s is plotted on Figure 6.6. Since $(N/m)^2$ is an amplitude of a single wave, it is multiplied by 1/m in order to convert amplitude to power spectral density. This conversion implies that the wavenumber bandwidth of saturated waves is 1/m. Note that, in general, the spectral amplitudes are less than this saturation limit by a factor of 4, so that wave amplitudes are approximately 50% of U-c. This coincides with the observations of individual waves presented earlier since those waves also had amplitudes less than or comparable to 50% of U-c even though they had constant amplitudes over a scale height or two and appeared to be saturated.

The superposition of waves can cause saturation at amplitudes less than the single wave saturation amplitude as has been shown in simulations by Fritts (1985). Fritts (1985) found that the superposition of 3 waves with

different wavelengths and amplitudes led to saturation of the waves at amplitudes of 0.2 to 0.8 (U-c).

The saturation amplitude could also be reduced by the presence of low-frequency waves. If the waves at any wavenumber have a frequency distribution similiar to that shown in Figure 6.1, a reduction of saturation amplitude could be inferred from the analysis of Fritts and Rastogi (1985), as discussed in section 2.2. Low-frequency, rotary gravity waves produce dynamic instabilities at amplitudes less than U-c because the transverse shear at that phase of the wave where stability is a minimum can lead to small values of the Richardson number and the subsequent production of turbulence. Since low-frequency waves comprise the bulk of the horizontal velocity frequency spectrum, the overall saturation amplitude could be somewhat reduced. However, it should be noted that all the low-frequency waves examined in Chapters 4 and 5 had amplitudes less than the reduced saturation amplitude and most were less than 50% of the reduced amplitude.

The fact that vertical wavenumber spectral amplitude is independent of height would appear to contradict theoretical predictions (Hines, 1960) and observations (Justus and Woodrum, 1973; Balsley and Garello, 1985 and references therein) of wave amplitudes growing with height. For conservative, non-dissipating waves, wave amplitude

must grow with height, inversely proportional to the square root of density, in order to keep the kinetic energy flux constant in a uniform environment. Observations do show that wave amplitudes increases with height but usually at a rate less than that indicated by theory. Growth with height is inferred from the fact that the amplitude of the gravity wave portion of observed frequency spectra increase with height.

The growth of kinetic energy density with height is illustrated in Figure 6.7, adapted from Balsley and Garello (1985). The line segments in the troposphere and stratosphere and again in the mesosphere are kinetic energy densities per unit volume obtained by integrating radar-observed, frequency spectra over selected bands and then multiplying by density. The 1 - 6 hr period band is considered to be representative of gravity wave frequencies.

The continuous curve, to the right of the Balsley and Garello estimates, is from a study by Justus and Woodrum (1973). They obtained average wave amplitude estimates by differencing rocket measured velocity profiles made at nearly the same time on consecutive days. This difference was assumed to be due to gravity waves and not tidal or planetary waves because the differences were over an integral multiple of days or tidal periods. Thus, tides

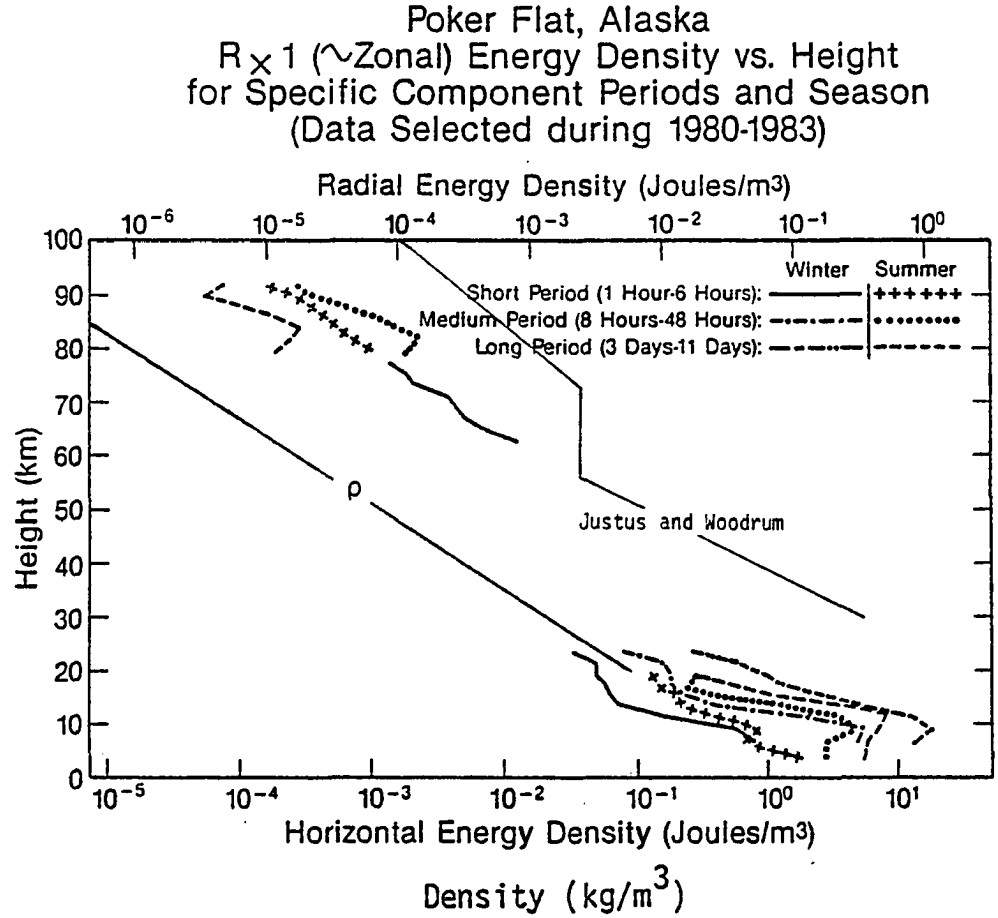

Figure 6.7 Kinetic energy density vs. height from Balsley and Garello (1985). Gravity wave kinetic energy density from Justus and Woodrum (1973) is also plotted.

would be removed and planetary waves were assumed to have periods much larger than a few days. Again, multiplication of squared wave amplitude by density produced kinetic energy density estimates.

Both sets of data show wave amplitudes growing with height. If wave amplitudes were held constant the observed curves would parallel the decrease of density with height shown by the line labelled ρ. The discrepancy between the growth of frequency spectra with height and the constant amplitude of the wavenumber spectra with height can be explained by the saturation of vertically propagating gravity waves.

The wavenumber spectra do not, in general, extend to low enough wavenumbers to identify a break in the spectral slope hypothesized to occur at m_*. Van Zandt (1982, 1985) hypothesized that such a break would occur near a mean wavenumber, which he labelled m_*. The form of wavenumber dependence of Van Zandt's model spectrum is $1/(1+(m/m_*)^3)$, where we have chosen the exponent as 3 to conform to the single wave saturation amplitude of N^2/m^3. With this form for the spectrum it can be seen that for $m < m_*$, the spectrum flattens out and is below the continuation of the m^{-3} continued from higher wavenumbers.

A plausible scenario for the growth/non-growth of the spectra is that the small-scale waves (λ_z < 1 km) are

saturating throughout the lower and middle atmosphere. Those waves that grow with height have longer vertical wavelengths corresponding to vertical wavenumbers less than m_*. Waves with these larger vertical wavelengths have amplitudes less than the saturation limit and can grow in amplitude as they propagate to higher levels. These longer waves attain saturation amplitudes at correspondingly greater heights, effectively moving m_* to smaller wavenumbers. Recall that in this initial, gravity wave model, it is assumed that the frequency and wavenumber components are separable, which allows waves with $m < m_*$ to be distributed across the frequency spectrum and permits significant portions of the frequency spectrum to be below the satruation limit.

The theoretical variation of the spectrum with height is illustrated in Figure 6.8, which was constructed using the form of Van Zandt's wavenumber spectrum and normalizing the individual spectra to be equal at high wavenumbers. The differences between the three curves are the result of specifying different values of m_*. The selected m_* correspond to vertical wavelengths of 1, 5 and 20 km for the troposphere, stratosphere and mesosphere, respectively.

This scenario agrees with a few observations of vertical wavelengths that have been made. Sato and Woodman

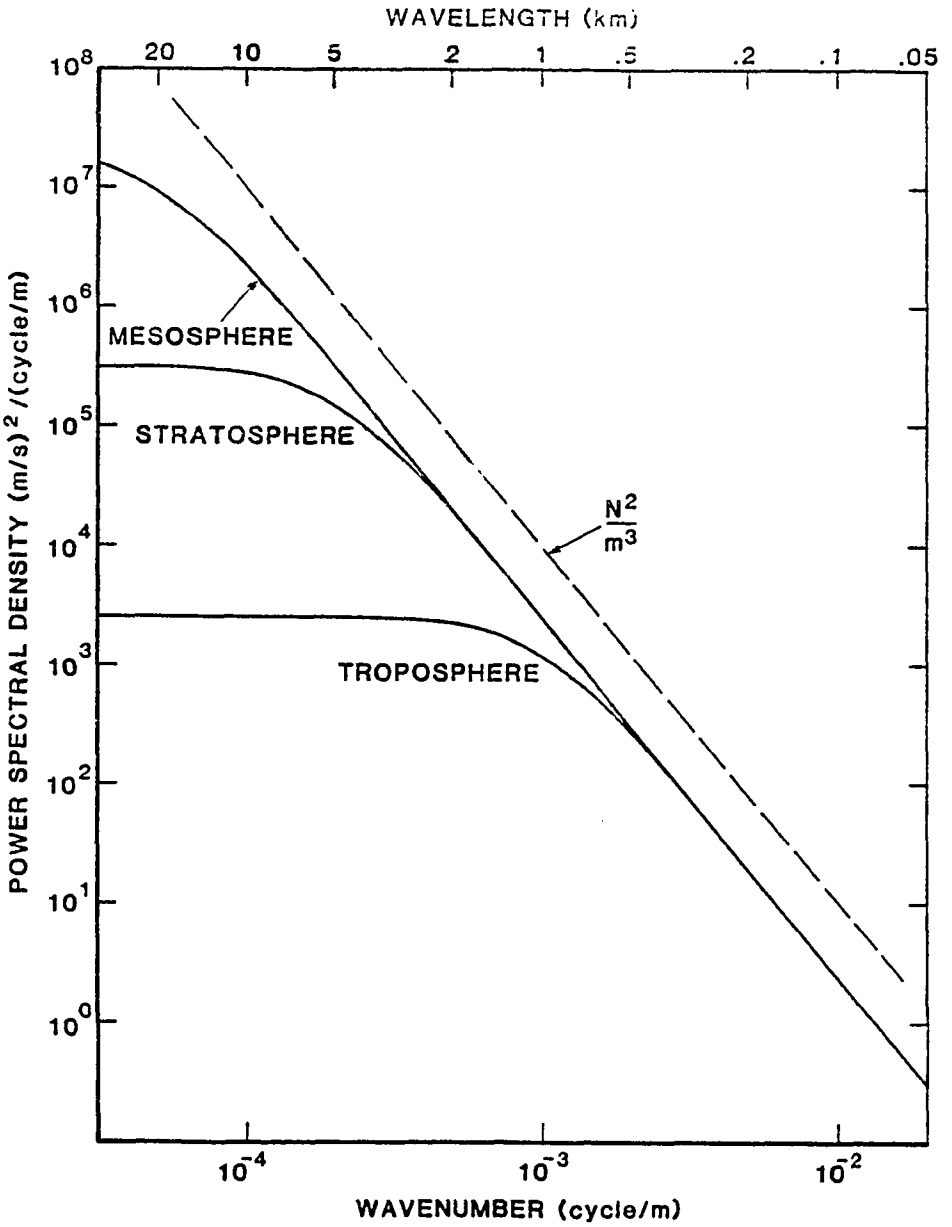

Figure 6.8 Schematic illustration of the effect of the proposed variation of m_* with height. The tropospheric, stratospheric and mesospheric values of m_* used here correspond to vertical wavelengths of 1, 5 and 20 km, respectively.

(1982) observed 2 km vertical wavelength waves to be dominant in the low stratosphere over a two day period. The waves identified in Chapters 4 and 5 had vertical wavelengths of 10 to 30 km in the mesosphere. Van Zandt (private communication, 1985) has computed values of m_*, combining the wavenumber spectra of Figure 6.2, 6.3 and 6.4 with the frequency spectra of Balsley and Carter (1982) and Balsley and Garello (1985) and his spectral model that implied mean vertical wavelengths were 19 and 30 kms in the summer mesosphere.

Thus, the growth in amplitude of frequency spectra with height is attributable to the amplitude growth of long vertical wavelength waves. This hypothesis could easily be tested if sufficiently long vertical profiles of wind velocity were obtained in the stratosphere. An ST radar should be able to provide 10 km of high resolution data from the stratosphere that should show evidence of a break in the vertical wavenumber spectra.

Chapter 7

Conclusions

Gravity wave dynamics near the mesopause have been investigated through the use of rocket and MST radar measurements. It has been shown, in this thesis, that gravity waves account for the bulk of the mesoscale energy spectrum.

Comparisons of rocket and radar measured mesospheric wind velocities demonstrated that the two techniques produced equivalent mean wind profiles. However, there were differences between the two sets of profiles, most likely due to the horizontal separation of the measurement sites and to small horizontal scale waves and inhomogeneities producing apparently uncorrelated fluctuations at the two sites.

The complementary strengths of rocket and radar techniques were used to identify a large-scale gravity wave in data collected near the summer mesopause. Rockets provide instantaneous profiles of wind velocity and temperature over an extensive height range. The 50 Mhz Poker Flat MST radar provides radial wind velocity measurements from a limited height range near the mesopause (and from a broader height range in the troposphere and stratosphere) over an extensive period of time. Thus, the temperature profiles and complete height coverage of the

rockets, along with the nearly continuous time series from the radar, allow detailed analysis of wave activity that would not be feasible with either instrument alone.

The rocket and radar data permitted gravity waves to be studied through identification of individual, nearly monochromatic waves. During the STATE campaign, two large-scale, large-amplitude, low-frequency inertio-gravity waves were found to be propagating upward and to the southwest. The temperature perturbation of one wave that appeared in a rocket measured temperature profile pinpointed the direction of wave propagation. Radar measured S/N time series showed that the intensity of 3m scale refractive index irregularities was greatest in that phase of the wave in which the temperature perturbation lapse rate was most negative and the atmosphere most nearly unstable, in accordance with linear saturation theory. That phase was also the point in the wave field where the perturbation velocity vector was oriented in the direction of wave propagation. This observation permitted the propagation direction of other waves to be determined with radar measurements of S/N and velocity perturbations alone. Thus, it was seen that the regions of strongest signal strength observed with the Poker Flat radar are related to the temperature and velocity perturbations associated with large-amplitude, low-frequency waves.

It is interesting to note that all of the waves that were individually identified, in both winter and summer data, had phase speeds greater than the mean wind speed and were primarilly propagating meridionally. The waves were undergoing dissipation over part of the observation region and therefore were producing net accelerations of the mesospheric mean flow. However, the result of the inferred momentum flux divergence was to accelerate the mean flow in the meridional direction, in most cases. The present theory of the mesospheric general circulation assumes gravity waves to be transferring eastward momentum in the summer and westward momentum in the winter to the mesosphere. Failure to identify these zonally propagating waves suggests that they are not the largest amplitude waves in the mesosphere and that the zonal wave drag is being supplied by smaller-scale, higher-frequency waves that are difficult to separate from the larger amplitude motions in the wind field.

Another perspective on mesospheric gravity waves was afforded by the examination of vertical wavenumber spectra of radial velocity fluctuations. Spectral studies give a statistical overview of the entire wind velocity field. By comparing observed spectra with Van Zandt's (1985) empirical gravity wave model, it was found that the majority of the fluctuations contributing to the spectra

could be identified as gravity waves since the ratio of oblique to vertical spectral amplitudes closely matched the ratio predicted by the model and the gravity wave dispersion relation.

The amplitudes of the vertical wavenumber spectra measured in the mesosphere were found to be approximately equal to spectral amplitudes measured in the stratosphere and also in the troposphere when scaled by the local N^2. The spectral amplitudes were seen to be consistent with those anticipated for a spectrum of saturating, small vertical scale wave motions as a consequence of convective or dynamic instabilities. This evidence of small-scale wave saturation throughout the atmosphere demonstrates the validity of Weinstock's (1982) conclusion that wave saturation occurs throughout the atmosphere.

Spectral amplitudes were approximately 25% of that necessary for a monochromatic wave to become convectively unstable. The fact that the apparently monochromatic waves that were individually identified appeared to be saturated even though their amplitudes were less than half of the convective instability threshold indicates that something other than monochromatic, linear wave theory is required to explain wave saturation. A reduced saturation limit could be produced by wave superposition as was shown by the simulations of Fritts (1985). Another cause of the reduced

saturation amplitude could be the transverse shear of inertio-gravity waves, that occurs at the phase of the wave where the lapse rate is most nearly unstable, leading to small Richardson numbers and dynamic instabilities (Fritts and Rastogi, 1985). The final resolution of the cause of the reduced saturation amplitudes depends, in part, on the analysis of the two-dimensional (frequency and wavenumber) energy spectrum so that the frequency distribution at any vertical wavenumber can be determined. This will require much longer time series of high spatial resolution velocity fluctuations than were available for this study.

One major problem with the Poker Flat data set was discovered: a vertical velocity bias away from zero introduced by a combination of DC filtering and time series windowing. A unique measurement that MST radars make is the determination of vertical velocities. In order to accurately measure the vertical velocity, the highest velocity resolution possible should be used and clutter rejection schemes should be carefully considered. One method of minimizing the effect of the DC or clutter filtering would be to perform the DC filtering by subtracting the mean of the time series, but to delay the windowing until the frequency spectrum had been calculated. Once in the frequency domain, the DC point could be interpolated and a three point smoothing function could be

convolved with the spectrum to duplicate the effect of windowing in the time domain. This approach would eliminate the three point notch put in the Doppler spectrum near zero by the present analysis routines.

The recommendation for future research on gravity wave propagation and saturation is that similar types of studies be carried out in the stratosphere with more than three radar beams. To determine the two-dimensional energy spectrum, continuous time and height series are needed, which could be provided by ST radars which typically observe from near the ground up to 25 km throughout the day, not just when the atmosphere is sunlit. It is also desirable to perform the analysis using information on stratification and temperature perturbations obtained from temperature soundings. These temperature soundings could be provided on a continuous basis by lidar observations of the stratosphere and mesosphere for upper atmospheric studies and by the routine rawinsonde soundings of the troposphere and lower stratosphere for lower atmosphere research.

Several radar beams are needed to study the azimuthal anisotropy of wave propagation. Vincent and Reid (1983) used two co-planar beams directed at equal but opposite zenith angles to determine the direction and magnitude of momentum flux in the mesosphere. Similar experiments need

to be done at other locations and throughout the troposphere and stratosphere to locate the sources of the waves that are transporting momentum and energy to the mesosphere. At least four radar beams, two pairs of beams directed at equal but opposite zenith angles in orthogonal planes, are required to begin to estimate the anisotropy of momentum flux needed to produce the observed features of the general circulation of the middle atmosphere. Beams directed at several azimuths would also produce data needed to examine the anisotropy found in the wavenumber spectra presented in Chapter 6. The beams would also provide several, simultaneous frequency and wavenumber spectra which could be used to more accurately quantify the gravity wave contribution to the total energy spectra.

Further observations of vertical wavenumber spectra are needed to more precisely define the gravity wave model. Measurements of spectral amplitude must be taken in conjunction with temperature measurements to determine the exact dependence of the saturation amplitude on N^2. Careful observations of the low wavenumber end of the spectrum are required in order to improve the functional specification of the gravity wave model. If the amplitude dependence on atmospheric stability and the low wavenumber

form of the spectrum were accurately known, then the vertical wavenumber, gravity wave spectrum could be easily specified by the single parameter, m_*, which would greatly improve model parameterizations of gravity wave - mean flow interactions and other studies of gravity wave effects.

Literature Cited

Balsley, B. B. and D. A. Carter, The spectrum of atmospheric velocity fluctuations at 8 and 86 km, Geophys. Res. Lett., 9, 465 - 468, 1982.

Balsley, B. B., W. L. Ecklund, D. A. Carter and P. E. Johnston, The MST radar at Poker Flat, Alaska, Rad. Sci., 15, 213 - 223, 1980.

Balsley, B. B., W. L. Ecklund and D. C. Fritts, VHF echoes from the high-latitude mesosphere and lower thermosphere: Observations and interpretations, J. Atmos. Sci., 40, 2451 - 2466, 1983.

Balsley, B. B., W. L. Ecklund and D. C. Fritts, VHF echoes from the Arctic mesosphere and lower therrmosphere, Part I: Observations, in Dynamics of the Middle Atmosphere, editted by J. R. Holton and T. Matsuno, Terra, Tokyo, 77 - 96, 1984.

Balsley, B. B. and K. S. Gage, The MST radar technique: Potential for middle atmospheric studies, Pure and Appl. Geophys., 118, 452 - 493, 1980.

Balsley, B. B. and R. Garello, The kinetic energy density in the troposphere, stratosphere and mesosphere: A preliminary study using the Poker Flat MST radar in Alaska, Rad. Sci., in press, 1985.

Booker, J. R. and F. P. Bretherton, The critical layer for internal gravity waves in shear flow, J. Fluid Mech., 27, 513 - 539, 1967.

Carter, D. A., Discrimination against interfering signals at the Poker Flat MST radar, MAP Handbook #9, editted by S. A. Bowhill and B. Edwards, 120 - 121, 1983.

CIRA, COSPAR International Reference Atmosphere 1972, Pergammon Press, Oxford, 450 pp., 1972.

Dewan, E. M., Stratospheric wave spectra resembling turbulence, Sci., 204, 832 - 835, 1979.

Dewan, E. M., N. Grossbard, A. F. Quesada and R. E. Good, Spectral analysis of 10m resolution scalar velocity profiles in the stratosphere, Geophys. Res. Lett., 11, 80 - 83, and Correction to "Spectral analysis of 10m...", Geophys. Res. Lett., 11, 624, 1984.

Dunkerton, T. J., Stochastic parameterization of gravity wave stresses, J. Atmos. Sci., 19, 1711 - 1725, 1982.

Ecklund, W. L. and B. B. Balsley, Long-term observations of the Arctic mesosphere with the MST radar at Poker Flat, Alaska, J. Geophys. Res., 86, 7775 - 7780, 1981.

Ecklund, W. L., B. B. Balsley, D. A. Carter, A. C. Riddle, M. Crochet and R. Garello, Observations of vertical motions in the troposphere and lower stratosphere using three closely-spaced ST radars, Rad. Sci., in press, 1985.

Eddy, A., C. E. Duchon, F. M. Haase and D. R. Haragan, Determination of winds from meteorological rocketsondes, Report No. 2, Atmospheric Science Group, Univ. of Texas, 29 pp., 1965.

Eliassen, A. and E. Palm, On the transfer of energy in stationary mountain waves, Geofysike Publikasjoner, 22, no. 3, 1 - 23, 1960.

Endlich, R. M., R. C. Singleton and J. W. Kaufman, Spectral analysis of detailed vertical wind speed profiles, J. Atmos. Sci., 26, 1030 - 1041, 1969.

Frezal, M. E., M. Glass, J. L. Fellous and M. Massebeuf, Simultaneous meteor radar observations at Monpazier (France, 44°N) and Punta Borinquen (Puerto Rico, 18°N). III The latitudinal variations of the energy of gravity waves (2 - 8h) in the high mesosphere, J. Atmos. Terr. Phys., 43, 543 - 547, 1981.

Fritts, D. C., Gravity wave saturation in the middle atmosphere: A review of theory and observations, Rev. Geophys. Space Phys., 22, 275 - 308, 1984.

Fritts, D. C., A numerical study of gravity wave saturation: Nonlinear and multiple wave effects, J. Atmos. Sci., in press, 1985.

Fritts, D. C., B. B. Balsley and W. L. Ecklund, VHF echoes from the Arctic mesosphere and lower thermosphere, Part II: Interpretations, in Dynamics of the Middle Atmosphere, editted by J. R. Holton and T. Matsuno, Terra, Tokyo, 97 - 116, 1984.

Fritts, D. C. and P. K. Rastogi, Convective and dynamical instabilities due to gravity wave motions in the lower and middle atmosphere: Theory and observations, Rad. Sci., in press, 1985.

Gage, K. S., Evidence for a $k^{-5/3}$ law inertial range in mesoscale two-dimensional turbulence, J. Atmos. Sci., 36, 1950 - 1954, 1979.

Gage, K. S. and T. E. Van Zandt, Wind measurement techniques available for the Middle Atmosphere Program, J. Geophys. Res., 86, 9591 - 9598, 1981.

Garrett, C. and W. Munk, Space-time scales of internal waves, Geophys. Fluid Dyn., 2, 225 - 264, 1972.

Garrett, C. and W. Munk, Space-time scales of internal waves: A progress report, J. Geophys. Res., 80, 291 - 297, 1975.

Geller, M. A., Dynamics of the middle atmosphere, Spa. Sci. Rev., 34, 359 - 375, 1983.

Hines, C. O., Internal gravity waves at ionospheric heights, Can. J. Phys., 38, 1441 - 1481, 1960.

Hines, C. O., The Upper Atmosphere in Motion, Geophysical Monograph 18, AGU, Washington, D.C., 1027 pp., 1974.

Hinze, J. O., Turbulence, 2nd ed., McGraw-Hill, New York, 790 pp., 1975.

Hirota, I., Y. Maekawa, S. Fukao, K. Fukuyama, M. P. Sulzer, J. L. Fellous, T. Tsuda and S. Kato, Fifteen-day observation of mesospheric and lower thermospheric motions with the aid of the Arecibo UHF radar, J. Geophys. Res., 88, 6835 - 6842, 1983.

Hodges, R. R., Jr., Generation of turbulence in the upper atmosphere by internal gravity waves, J. Geophys. Res., 72, 3455 - 3458, 1967.

Hodges, R. R., Jr., Eddy diffusion coefficients due to instabilities in internal gravity waves, J. Geophys. Res., 74, 4987 - 4090, 1969.

Holton, J. R., The role of gravity wave induced drag and diffusion in the momentum budget of the mesosphere, J. Atmos. Sci., 39, 791 - 799, 1982.

Holton, J. R., The influence of gravity wave breaking on the general circulation of the middle atmosphere, J. Atmos. Sci., 40, 2497 - 2507, 1983.

Houghton, J. T., The stratosphere and mesosphere, Quart. J. Roy. Met. Soc., 104, 1 - 29, 1978.

Jenkins, G. M. and D. G. Watts, Spectral Analysis and its Applications, Holden-Day, San Francisco, 525 pp., 1968.

Justus, C. R. and A. Woodrum, Upper atmospheric planetary-wave and gravity-wave observations, J. Atmos. Sci., 30, 1267 - 1275, 1973.

Leovy, C., Simple models of thermally driven mesospheric circulation, J. Atmos. Sci., 21, 327 - 341, 1964.

Lilly, D. K., Stratified turbulence and the mesoscale variability of the atmosphere, J. Atmos. Sci., 40, 749 - 761, 1983.

Lindzen, R. S., The application of classical tidal theory, Proc. Roy. Soc. A, 303, 299 - 316, 1968.

Lindzen, R. S., Turbulence and stress due to gravity wave and tidal breakdown, J. Geophys. Res., 86, 9707 - 9714, 1981.

Manson, A. H. and C. E. Meek, Gravity waves of short period (5 - 90 min), in the lower thermosphere at 52°N (Saskatoon, Canada), J. Atmos. Terr. Phys., 42, 103 - 113, 1980.

Manson, A. H., C. E. Meek and J. B. Gregory, Gravity waves of short period (5 - 90 min), in the lower thermosphere at 52°N (Saskatoon, Canada); 1978/1979, J. Atmos. Terr. Phys., 43, 35 - 44, 1981.

Muller, P., Small-scale vortical motions, Proceedings of the Aha Huliko'a Workshop on Internal gravity waves and small-scale turbulence, editted by P. Muller and R. Pujalet, Hawaii Inst. of Geophysics, Honolulu, 249 - 262, 1984.

Munk, W., Internal waves and small-scale processes, Evolution of Physical Oceanography, editted by B. A. Warren and C. Wunsch, MIT Press, 264 - 291, 1981.

Orlanski, I. and K. Bryan, Formation of the thermocline step structure by large-amplitude internal gravity waves, J. Geophys. Res., 74, 6975 - 6983, 1969.

Philbrick, C. R., A. C. Faire and D. H. Fryklund, Measurements of atmsopheric density at Kwajalein Atoll, 18 May 1977, AFGL-TR-78-0058, Air Force Surveys in Geophysics, No. 384, 1978.

Rastogi, P. K. and S. A. Bowhill, Gravity waves in the equatorial mesosphere, J. Atmos. Terr. Phys., 38, 51 - 60, 1976.

Rottger, J., Wind variability in the stratosphere deduced from spaced antenna VHF radar measurements, Preprint volume of the 20th Conf. on Radar Met. (Boston), AMS, Boston, 22 - 29, 1981.

Royrvik, O., K. P. Gibbs and S. A. Bowhill, VHF power scattered from the mesosphere at mid-latitudes, J. Geophys. Res., 87, 2501 - 2508, 1982.

Sato, T. and R. F. Woodman, Fine altitude resolution radar observations of upper-tropospheric and lower-stratospheric winds and waves, J. Atmos. Sci., 39, 2539 - 2545, 1982.

Smith, S. A. and D. C. Fritts, Estimation of gravity wave motions, momentum fluxes and induced mean flow accelerations in the winter mesosphere over Poker Flat, Alaska, Preprint volume of the 21st Conf. on Radar Met. (Edmonton), AMS, Boston, Mass., 104 - 110, 1983.

Smith, S. A. and D. C. Fritts, Poker Flat MST radar and meteorological rocketsonde wind profile comparisons, Geophys. Res. Lett., 11, 538 - 540, 1984.

Van Zandt, T. E., A universal spectrum of buoyancy waves in the atmosphere, Geophys. Res. Lett., 9, 575 - 578, 1982.

Van Zandt, T. E., A model for gravity wave spectra observed by Doppler sounding systems, Rad. Sci., in press, 1985.

Vincent, R. A., Gravity wave motions in the mesosphere, J. Atmos. Terr. Phys., 46, 119 - 128, 1984.

Vincent, R. A. and S. M. Ball, Mesospheric winds at low- and mid-latitudes in the southern hemisphere, J. Geophys. Res., 86, 9159 - 9169, 1981.

Vincent, R. A. and I. M. Reid, HF Doppler measurements of mesospheric gravity wave momentum fluxes, J. Atmos. Sci., 40, 1321 - 1333, 1983.

Watkins, B. J. and K. Jayaweera, Comparisons of vertical winds measured with the Chatanika and Poker Flat radars, J. Geophys. Res., in press, 1985.

Weinstock, J., Nonlinear theory of acoustic-gravity waves 1. Saturation and enhanced diffusion, J. Geophys. Res., 81, 633 - 652, 1976.

Weinstock, J., Nonlinear theory of gravity waves: momentum deposition, generalized Rayleigh friction, and diffusion, J. Atmos. Sci., 39, 1698 - 1710, 1982.

Weinstock, J., Gravity wave saturation and eddy diffusion in the middle atmosphere, J. Atmos. Terr. Phys., 46, 1069 - 1082, 1984.

Woodman, R. F. and A. Guillen, Radar observations of winds and turbulence in the stratosphere and mesosphere, J. Atmos. Sci., 31, 493 - 505, 1974.